

ABSTRACT

Seismo-Lineament Analysis of Selected Earthquakes in the Tahoe-Truckee Area, California and Nevada

Ryan D. Lindsay, M.S.

Committee Chairperson: Vincent S. Cronin, Ph.D.

Focal mechanism solutions from 29 $M \geq 3$ earthquakes recorded between 1966 and late 2009 in the Tahoe-Truckee area, California and Nevada, were used to establish a preliminary spatial correlation between these earthquakes and faults. In previous studies, only the 1966 Truckee earthquake ($M 6$) had been correlated with a fault: the Dog Valley fault. The most recent events on other Quaternary faults in the area were previously attributed to the mid-Holocene to Pleistocene. In this study, preliminary spatial correlation has been described between one or more earthquakes and the Dog Valley fault zone, Polaris fault, West Tahoe fault, North Tahoe fault, Incline Village fault and the hypothetical Agate Bay fault. Two additional trends are defined by seismo-lineaments and geomorphic indicators of possible faulting, and might encompass previously unrecognized seismogenic faults. This area is subject to earthquakes on north-striking east-dipping normal faults, northwest-striking dextral faults and their conjugates -- northeast-striking sinistral faults.

Seismo-Lineament Analysis of Selected Earthquakes in the Tahoe-Truckee Area,
California and Nevada

by

Ryan D. Lindsay, B.S.

A Thesis

Approved by the Department of Geology

Steven G. Driese, Ph.D., Chairperson

Submitted to the Graduate Faculty of
Baylor University in Partial Fulfillment of the
Requirements for the Degree
of
Master of Science

Approved by the Thesis Committee

Vincent S. Cronin, Ph.D., Chairperson

Robert J. Pulliam, Ph.D.

Joseph D. White, Ph.D.

Accepted by the Graduate School
May 2012

J. Larry Lyon, Ph.D., Dean

Copyright © 2011 by Ryan D. Lindsay

All rights related to this thesis are reserved, with the irrevocable exception that Vincent S. Cronin retains all rights to his intellectual property and to the research products/ideas that were shared with Ryan D. Lindsay in the course of this research.

TABLE OF CONTENTS

	Page
List of Figures	vii
List of Tables	ix
Acknowledgments	x
Dedication	xi
Epigraph	xii
CHAPTER ONE	1
Introduction	1
CHAPTER TWO	8
Background	8
Tectonic Setting	8
Faults with Known or Suspected Quaternary Displacement	15
CHAPTER THREE	26
Methods	26
Selection of Study Area	26
DEM Acquisition and Conversion	26
Earthquake Data Acquisition	29
Analysis	32
Seismo-Lineament Analysis	32
Geomorphic Lineament Analysis	36
Field Methods	40
Fisher Statistics	42

CHAPTER FOUR	44
Results	44
Earthquakes	44
Seismo-Lineaments	45
Geomorphic Lineament Analysis	47
Fieldwork	50
CHAPTER FIVE	53
Interpretation of Results	53
Introduction	53
Faults and Seismo-Lineament Trends	59
Polaris fault	59
Dog Valley fault zone	64
Sierra-Tahoe Frontal fault zone	65
West Tahoe – Dollar Point fault zone and Agate Bay fault	71
Prosser Creek trend	71
North Tahoe fault	76
Martis Creek trend	78
Synthesis	81
CHAPTER SIX	84
Conclusions	84
Introduction	84
Suggestions for future work	86

APPENDICES

Appendix A – SLAMCode <i>Mathematica</i> notebook used in this thesis	90
Appendix B – FisherStatsSD.nb <i>Mathematica</i> notebook used in this thesis	103
Appendix C – Location of field sites	114
Appendix D – Fisher statistics, sites 7 and 19	115
Appendix E – Output seismo-lineament maps from SLAMCode.nb.	117

REFERENCES CITED	133
------------------	-----

LIST OF FIGURES

Figure	Page
1. Location of study area	2
2. 7.5 minute quadrangles used in thesis	3
3. Epicenters for 1967-2009 earthquakes	4
4. Map of faults in the study area	6
5. Strain rates and plate velocities of Western North America	9
6. Generalized tectonic setting of the study area	10
7. Primary structural domains of the study area	14
8. Perspective illustrations depicting seismo-lineaments	33
9. Cross sections depicting uncertainty in location of nodal plane	35
10. Perspective illustration of seismo-lineament on hillshade surface	39
11. Seismo-lineaments associated with earthquake 24a	48
12. Geomorphic lineaments possibly related to known and unknown faults	49
13. Sites visited to search for ground surface exposures of faults	51
14. Map of focal mechanism solutions with known faults	55
15. Seismo-lineaments from earthquakes 9, 15, 25, 26, and 27c	60
16. Geomorphic indicator of faulting associated with the Polaris fault	62
17. Reverse fault observed at site 7	63
18. Seismo-lineaments from earthquakes 2, 3, 8, 9, 13, 25, and 29	66
19. Geomorphic lineaments and mapped fault traces in Dog Valley fault zone	67

20.	Oblique fault exposure at site 19	68
21.	Fault exposure at site 20	68
22.	Stereonet projections of the dip vector for the fault exposed at site 19	69
23.	Seismo-lineaments from earthquakes 5 and 13a	70
24.	Seismo-lineaments from earthquakes 16, 19, 22, 23, and 24	72
25.	Seismo-lineaments from earthquakes 8, 14, 15, and 16	73
26.	Geomorphic lineaments of Prosser Creek trend	74
27.	Seismo-lineaments from earthquakes 14, 17-21, 23, and 28	77
28.	Seismo-lineaments from earthquakes 1, 7, 11, and 27c	79
29.	Geomorphic lineaments of Martis Creek trend	80
30.	Interpretation of fault geometry in the study area	82

LIST OF TABLES

Table	Page
1. Earthquakes used to generate seismo-lineaments	30
2. Earthquakes that cluster temporally	44
3. Trend and plunge of the tensor axes of focal mechanism solutions	46
4. Preliminary interpretations of fault planes and fault correlations	57
5. Earthquakes spatially correlated with more than one fault or trend	59

ACKNOWLEDGEMENTS

My deepest gratitude goes to Dr. Cronin for having an inexhaustible passion for education, and always having faith in me as an undergraduate and graduate student. To my family and wife for their love and support they provided me during this process. To the Baylor Geology Department, Samson Resources, Ellis Exploration, and Sigma Xi for provided financial support. To Daniel Lancaster for his much needed help during field research. I would also like to thank Bruce Byars for giving me the opportunity to become his lab instructor for introductory ArcGIS. Finally, I would like to thank David Oppenheimer at the NCEDC for helping me track down the data needed to complete this thesis.

DEDICATION

To Granny - "Rocky Mountain High"

"Greatness is not in where we stand, but in what direction we are moving. We must sail sometimes with the wind and sometimes against it - but sail we must, and not drift, nor lie at anchor."

—Oliver Wendell Holmes

CHAPTER ONE

Introduction

The research described in this thesis is part of an effort to identify seismogenic faults and to map their intersection with the ground surface, so that the risks associated with these faults can be reduced. Seismogenic faults are faults that have produced earthquakes in the recent past, and are likely to produce additional earthquakes in the future. One interpretation of the meaning of “recent past” is provided in California’s Alquist-Priolo Earthquake Fault Zoning Act (Bryant and Hart, 2007), in which an active fault is defined as having “had surface displacement within Holocene time (about the last 11,000 years).”

The study area extends from north latitude 39.08° to 39.45° , west longitude 119.85° - 120.28° , including the northern half of Lake Tahoe in east-central California and west-central Nevada (Figure 1). This area was chosen in part because the annual meeting for the Association of Environmental and Engineering Geologists was held at Lake Tahoe in 2009, and a presentation about the Seismo-Lineament Analysis Method (SLAM) was invited (Cronin and others, 2009). Preparation for that meeting included a preliminary analysis of earthquakes in the Lake Tahoe Basin, which led to this thesis research project. Twenty 7.5 minute quadrangles encompass the study area, from north latitudes 39° to $39^{\circ}37.5'$ and west longitudes $119^{\circ}52.5'$ to $120^{\circ}22.5'$ (Figure 2).

The northern Tahoe Basin has had a moderate number of earthquakes in recent decades. The Northern California Earthquake Data Center (NCEDC) has records of approximately 1,700 earthquakes that occurred since 1967 with foci located within the study area (Figure 3). Of these, 38 earthquakes have reported magnitudes of 3.0 or

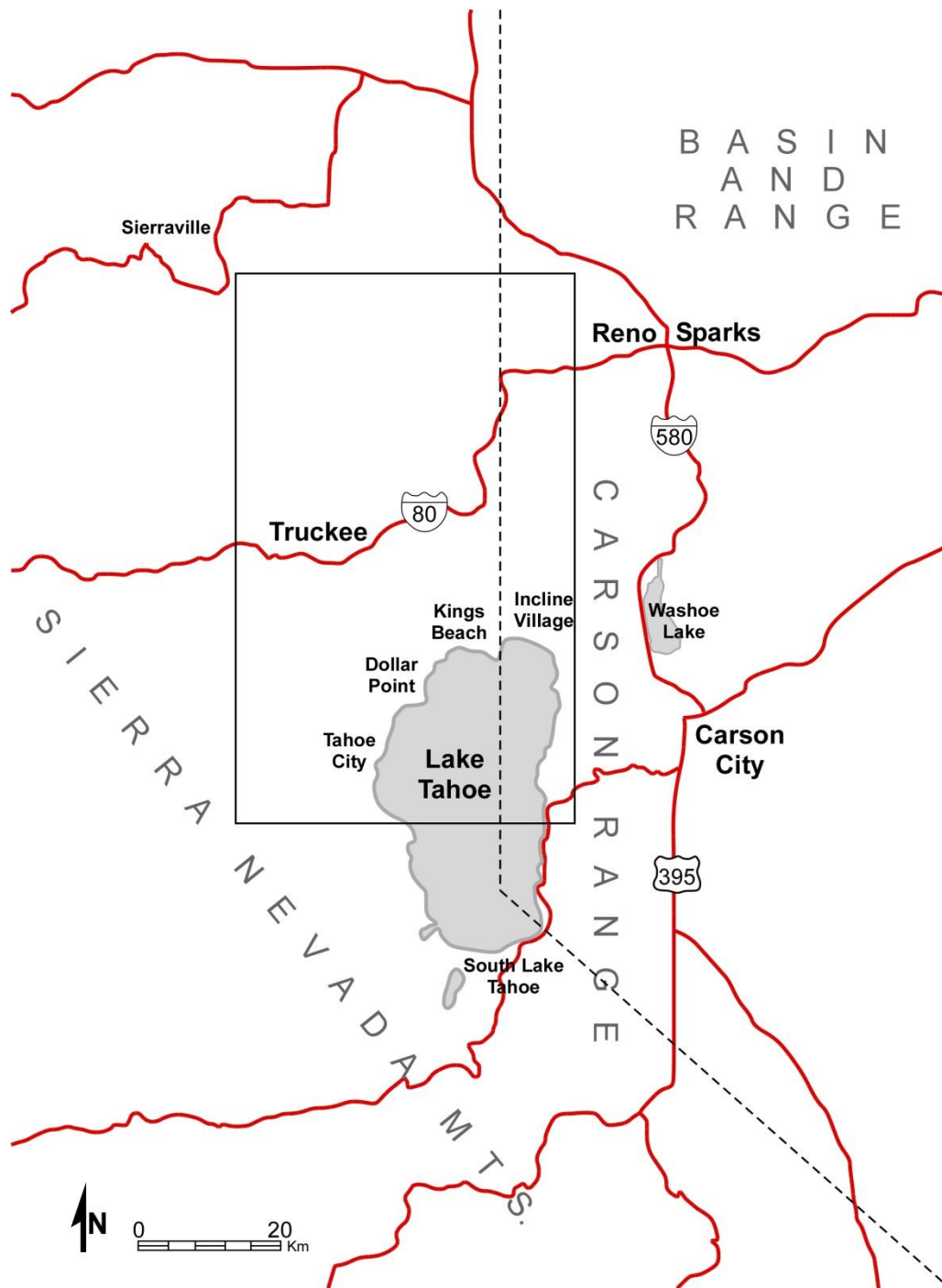


Figure 1. Location of study area (rectangle outlined in black). Dashed line is boundary between states of California, to the west, and Nevada to the east.

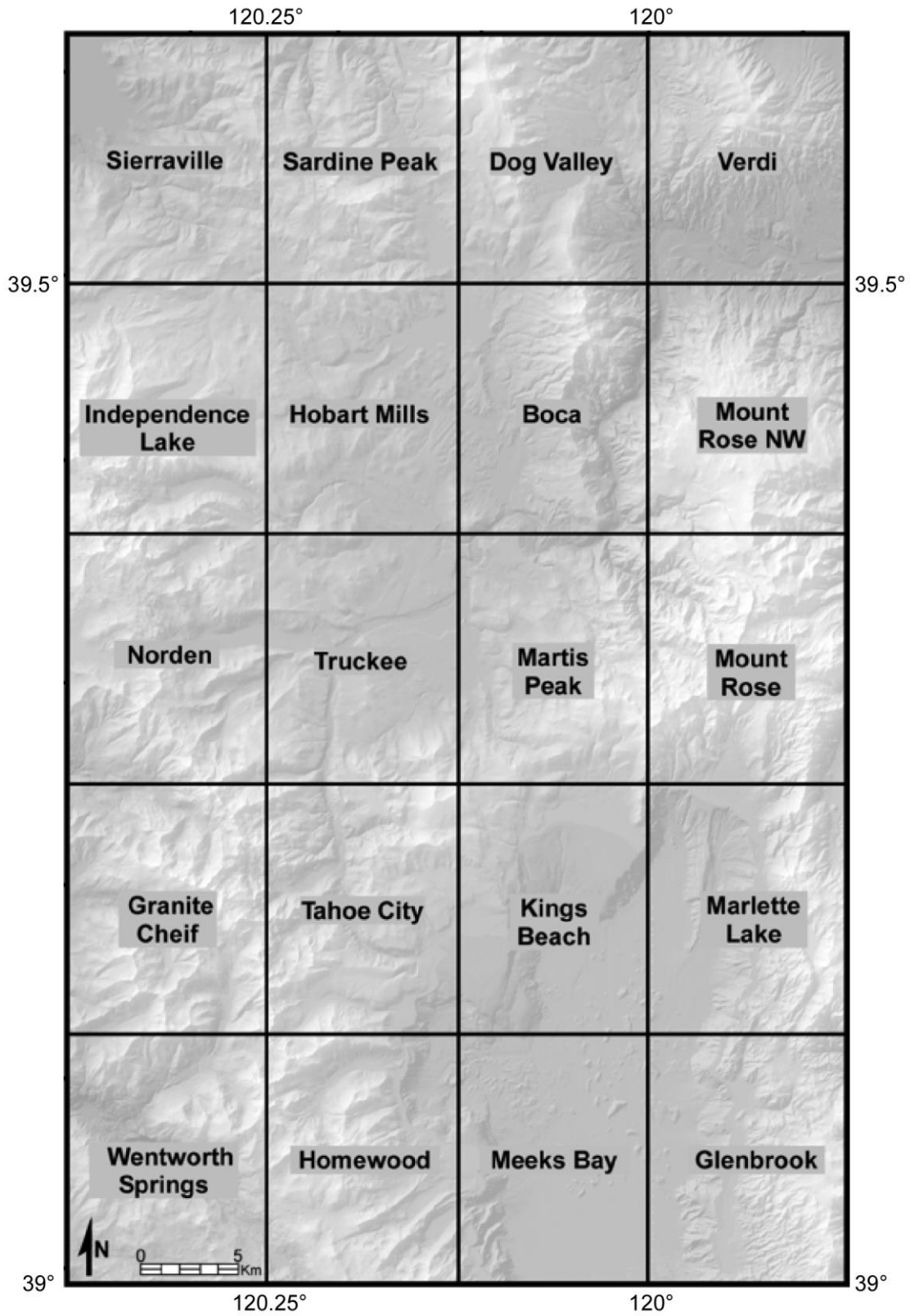


Figure 2. 7.5-minute quadrangles used in this thesis.

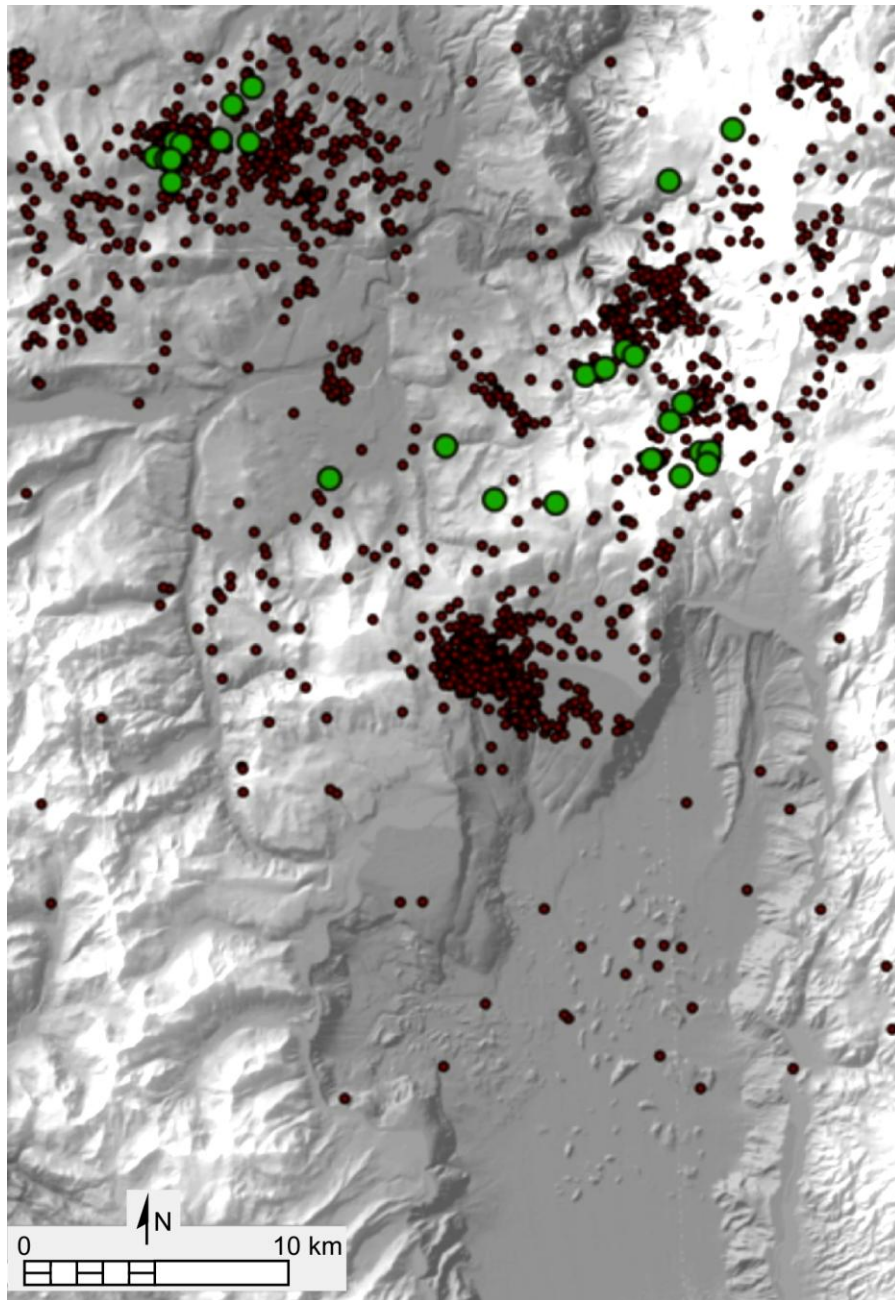


Figure 3. Epicenters for 1967-2009 earthquakes with $M_w < 3.0$ (red) and $M_w \geq 3.0$ (green). Data from the Northern California Earthquake Data Center.

greater. The largest earthquake reported for this area since 1967 was the $M_w 4.8$ event of October 30, 1998. Based on ground-surface cracking and the focal locations of aftershocks, the $M \sim 6$ Truckee earthquake of September 12, 1966 has been attributed to

the Dog Valley fault zone (*e.g.*, Quaternary Fault and Fold Database of the United States; Greensfelder, 1968; Kachadorian and others, 1967; Tsai and Aki, 1970; Ryall and others, 1968; Hawkins and others, 1986; Schweickert and others, 2004). Other historic earthquakes in the area have not caused documented rupture of the ground surface.

Late Neogene or Holocene displacement has been inferred for several faults in the study area. In the north Lake Tahoe Basin, the West Tahoe – Dollar Point, Stateline – North Tahoe, and the Incline Village faults are inferred to have produced multiple Mw 7.0 earthquakes during the Holocene (Brothers and others, 2009). The West Tahoe – Dollar Point fault is characterized by normal motion striking to the north and dipping to the east. The Stateline – North Tahoe and Incline Village faults are characterized by normal to sinistral motion striking to the northeast and dipping to the southeast (Brothers and others, 2009).

Further to the north, faulting between Sierra Valley and north Lake Tahoe is less understood and constrained. The two mapped fault zones in this area are the Dog Valley and Polaris fault zones. Both fault zones accommodate crustal shortening from the north and south with strike-slip motion (Schweickert and others, 2004). The Dog Valley fault is a zone of sinistral shear, and might have been the source of the 1966 M 6.0 Truckee earthquake (Hawkins and others, 1986; Schweickert and others, 2004). The Polaris fault was discovered in 2008 by Hunter and others (2009) using high resolution LiDAR data, and was subsequently studied by trenching. The Polaris fault is a zone of dextral shear, with the latest known slip occurring between the Pleistocene to Holocene (Hunter and others, 2011). The Dog Valley and Polaris Fault zones have a conjugate geometry relative to each other (Figure 4).

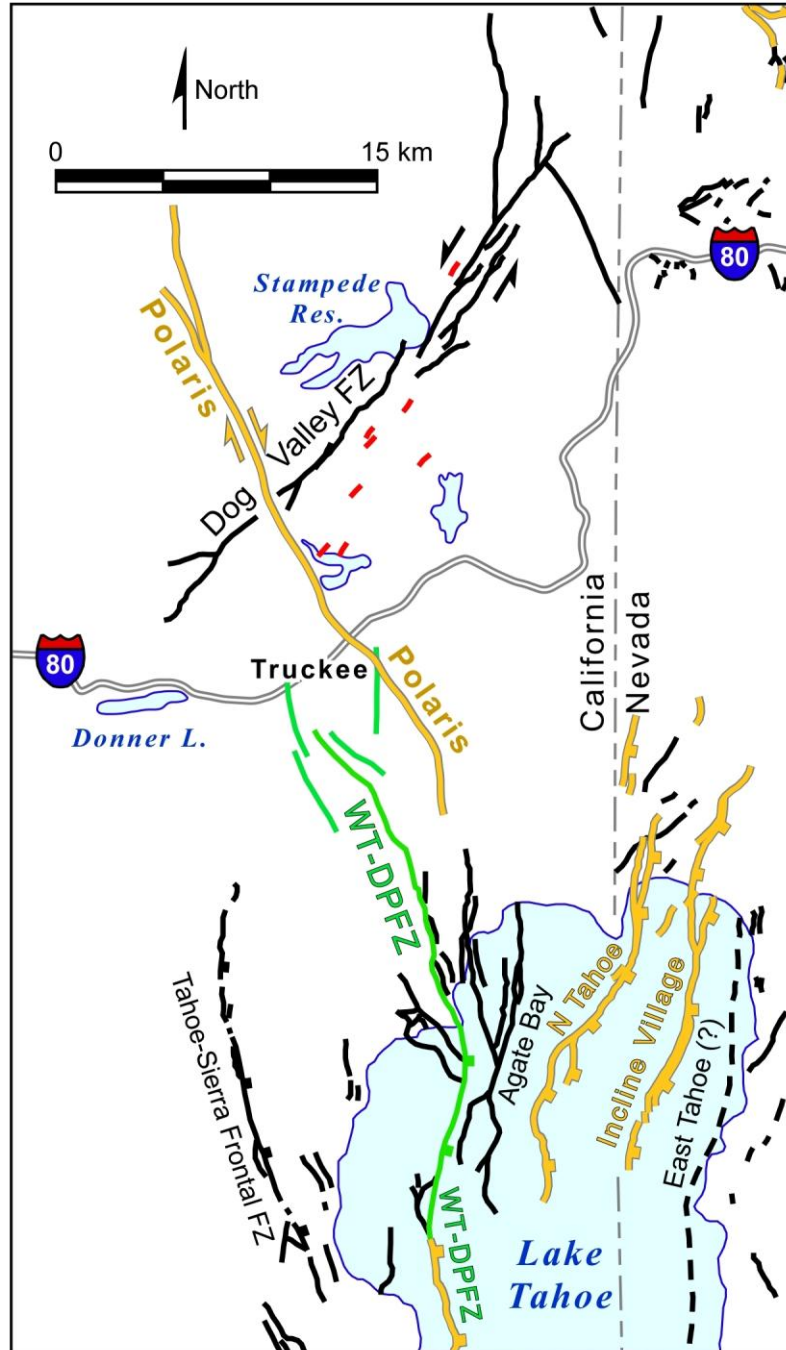


Figure 4. Map of faults in the study area, from the Quaternary Fault and Fold Database of the United States and Hunter and others (2011). Fault trace colors indicate the age of last known displacement: red < 150 years, yellow <15,000 years, green <130,000 years, black, <1600,000 years. WT-DPFZ is the West Tahoe-Dollar Point fault zone. Rectangles are on the footwall (down) blocks of normal faults.

Discovery and characterization of the full array of seismogenic faults in the study area is essential for earthquake disaster risk reduction. A substantial earthquake in the Lake Tahoe Basin could trigger a tsunami in Lake Tahoe, either through displacements along faults within the lake basin or by initiating landslides (*e.g.*, Ichinose and others, 2000; Kent and others, 2005; Moore and others, 2006). Most of the population of the Lake Tahoe area, including the towns of South Lake Tahoe, Incline Village, and Tahoe City, would be inundated by the maximum credible tsunami, as visualized by U.C. Santa Cruz researcher Steven Ward (simulations accessible via <http://es.ucsc.edu/~ward/>). A significant earthquake in the study area might also affect the nearby cities of Carson City, Reno and Truckee, and might disrupt major rail and highway transportation corridors such as Interstate Highway 80 across the Sierra Nevada Mountains.

The Seismo-Lineament Analysis Method (SLAM; Cronin and others, 2008) was developed as an aid to active-fault reconnaissance, and is used to spatially correlate an earthquake with the fault that generated it. This methodology has been applied in several projects to date, involving normal, reverse, strike-slip and oblique-slip faults (Bayliss, 2007; Seidman, 2007; Millard, 2007; Lancaster, 2011). The research described in this thesis involves the application of SLAM using selected earthquakes with epicenters located in the Tahoe-Truckee area, for which focal mechanism solutions have been published. The purpose of this thesis is to make preliminary spatial correlations between these selected earthquakes and the faults that caused them. This should facilitate the efforts of paleoseismologists and tectonic geomorphologists working to document active faults in the area through trenching and LiDAR-based geomorphic analysis

CHAPTER TWO

Background

Tectonic Setting

Atwater (1970) recognized that the western part of the continental United States was part of a broad transform boundary between the North American plate and the Pacific plate. Understanding of that boundary is still evolving. Our knowledge of the kinematics of lithospheric plates during the past 1-3 Myr is greatly improved over the models that were available to Atwater (*e.g.*, DeMets and others, 2010; Kreemer and others, 2003). Seismologists now collect earthquake data using denser arrays of seismographs, augmented by strainmeter and kinematic GPS data. GPS geodesy, which did not exist in 1970, has become a mature field and an indispensable tool for neotectonic analysis, allowing us to measure the relative motions of crustal blocks (Wdowinski and Eriksson, 2009). Much richer archives of gravity, magnetic and topographic data are now available throughout the US and abroad. With the benefit of decades of additional geologic, geodetic and geophysical data, it is clear that the western continental US is a region of present-day strain related to the motion of lithospheric plates, crustal blocks and sublithospheric upper mantle (Figure 5).

The study area for this thesis is located between the Pacific plate and the relatively rigid cratonic interior of the North American plate, within Atwater's broad zone of boundary deformation where there are a number of distinctive structural domains (Figure 6). To the west of the study area is the Sierra Nevada-Great Valley (SNGV) block (Atwater and Stock, 1998), which is sometimes called the Sierra Nevada microplate

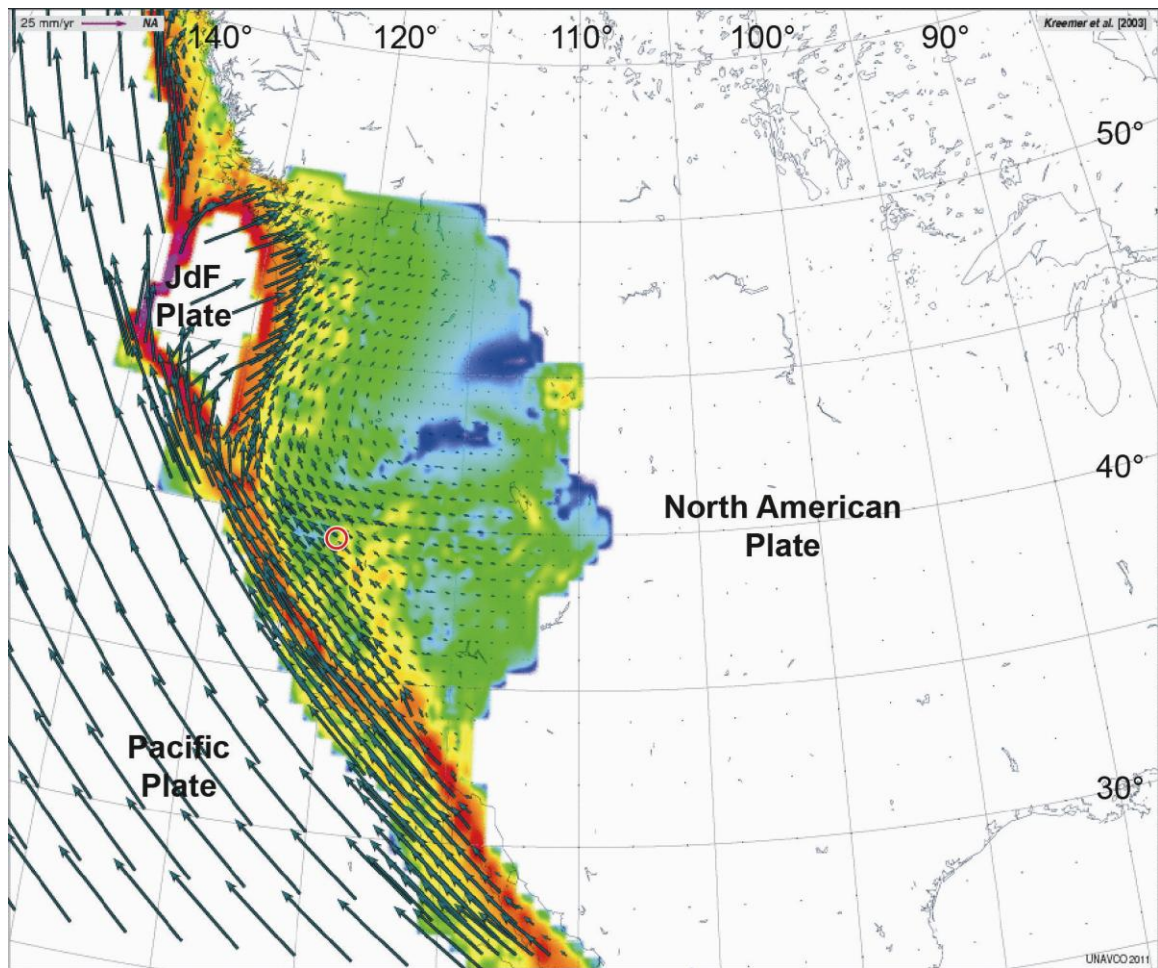


Figure 5. Strain rates (colored areas) and plate velocity vectors at selected locations relative to a fixed North America, modeled from GPS data for the western continental United States and excerpted from the Global Strain Rate Map (Kreemer and others, 2003). Red colors reflect higher strain rates and blue reflect lower strain rates. Red circle near latitude 40°N and longitude 120°W indicates the approximate location of the study area. Gorda plate is just south of the Juan de Fuca (JdF) plate. Map created in Jules Verne Voyager via http://www.unavco.org/edu_outreach/maptools.html.

(Argus and Gordon, 1991; Wernicke and Snow, 1998). The SNGV is a coherent terrane between the transpressional San Andreas fault system to the west and the transtensional Walker Lane system to the east. These fault systems accommodate most of the right-lateral transform motion between the North American and Pacific plates (Unruh and others, 2003; Wesnousky, 2005).

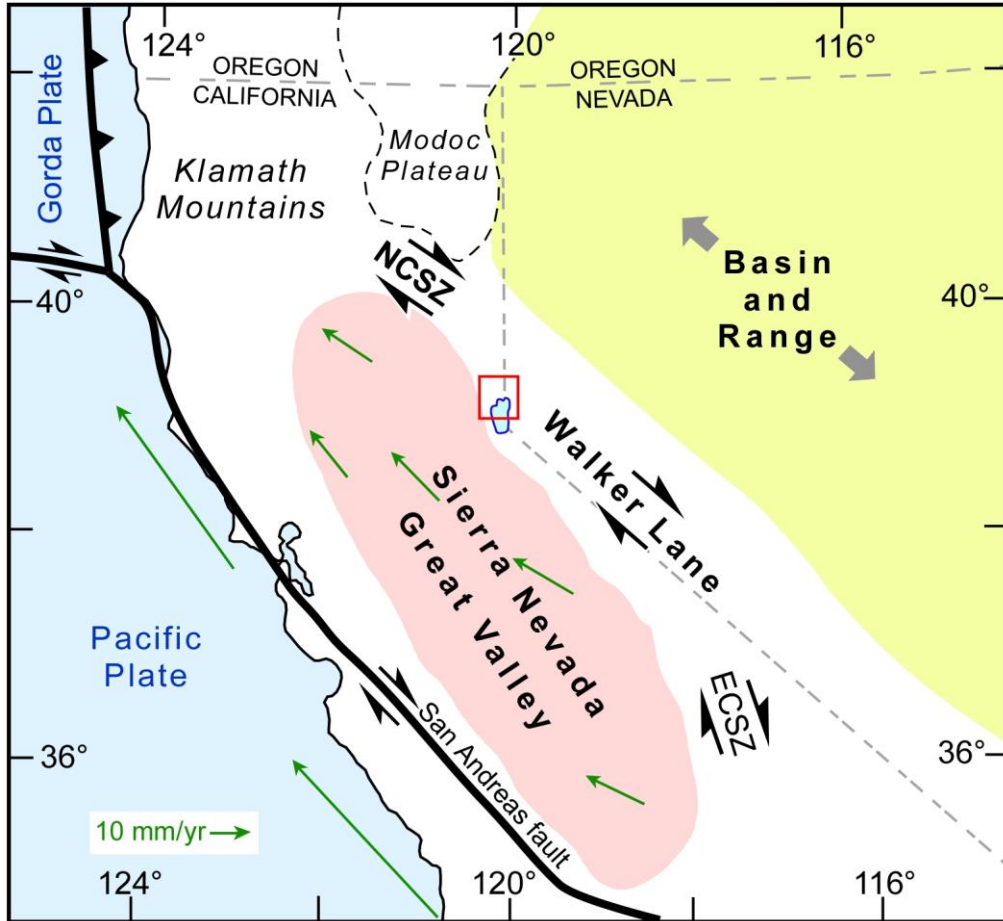


Figure 6. Generalized tectonic setting of the study area (red rectangle). ECSZ is Eastern California shear zone, and NCSZ is the Northern California shear zone of Hammond and others (2011). Green arrows are GPS velocities relative to fixed North American plate, adapted from Kreemer and others (2003) as plotted by Jules Verne Explorer via http://www.unavco.org/edu_outreach/maptools.html.

Walker Lane

The Walker Lane is a zone of seismogenic faulting between the SNGV and the Basin and Range Province to the east, extending from the Eastern California Seismic Zone (Locke and others, 1940; Savage and others, 1990; Dokka and Travis, 1990; Sauber and others, 1994; Dixon and others, 2003) northward toward the Modoc Plateau and Klamath Mountains. Current estimates are that the Walker Lane might accommodate ~20-25% of the relative motion between the Pacific and North American plates

(Hammond and Thatcher, 2007; Oldow and Cashman, 2009; Hammond and others, 2011).

The oldest displacement along the eastern edge of the Sierra Nevada occurred in the Miocene, with approximately 50-100 km of displacement along the Eastern California Shear Zone and Walker Lane boundary in southern California (Dokka and Travis, 1990; Faulds and others, 2005), 60-75 km in west-central Nevada (Oldow, 1992; Faulds and others, 2005), and minimal displacement in the northern Walker Lane. The northern Walker Lane in California and Nevada is the least developed and youngest part of the boundary (Faulds and others, 2005), suggesting growth of the Walker Lane northwestward overtime. Inferred northern propagation of displacement along the Walker Lane might be attributed to the northward migration of the Mendocino triple junction from 30 Myr–present (Atwater and Stock, 1998).

Approximately 9-13 mm/yr of dextral shear is partitioned across numerous strike-slip, dip-slip, and oblique-slip faults in the Walker Lane (Hearn and Humphreys, 1998; Dixon and others, 2000; Svarc and others, 2002; Bennett and others, 2003; Hammond and Thatcher, 2004, 2007; Brothers and others, 2009). The Lake Tahoe Basin is estimated to be extending in a WNW-ESE direction at a rate of 0.52-0.99 mm/yr (Dingler and others, 2009; Kent and others, 2005). The result of this differential motion between the Sierra Nevada and the Basin and Range is ~ 32 -164 nstrain/yr across the Lake Tahoe region, which is inferred to be a zone of lithospheric weakness adjacent to the stronger Sierra Nevada-Great Valley block (Kreemer and others, 2009).

Stewart (1988) divided the Walker Lane into nine structural domains, based on the orientation of map-scale faults. The northern Walker Lane is approximately 100 km

wide, trends ~N35-40W in the vicinity of the study area, and includes three of Stewart's structural domains (listed from north to south): the Pyramid Lake, Carson, and Walker Lake domains (Stewart, 1988; Hammond and others, 2011). Both the Pyramid Lake and Walker Lake domains are characterized by northwest trending dextral faults. The Pyramid Lake domain is coincident with the North California shear zone of Hammond and others (2011), and is dominated by northwest-trending right-lateral faults, including the Honey Lake fault, the Warm Springs Valley fault, the Pyramid Lake fault, and the Mohawk Valley fault zone.

The Carson domain is marked by known or suspected northeast-trending left-lateral faults including the Olinghouse fault, the Carson lineament and the Wabuska lineament. Cashman and Fontaine (2000) interpret rotated paleomagnetic vectors in the Carson domain to indicate a clockwise vertical-axis rotation rate of 2.8 to 5.7 °/Myr, while modeling of GPS data by Hammond and others (2011) indicates a lower rate of 1.3 ± 0.1 °/Myr. These domains wrap around the SNGV block in the Lake Tahoe region, which has the faulting characteristics of all three domains.

GPS geodetic studies of the Basin and Range and Walker Lane have illuminated the complex interactions of crustal blocks within this broad deformation zone (*e.g.*, Dixon and others, 2000; Oldow and others, 2001; Oldow, 2003; McCaffrey, 2005; Pancha and others, 2006; Hammond and Thatcher, 2004, 2005, 2007; Kreemer and Hammond, 2007; Hammond and others, 2009, 2011; Kreemer and others, 2009; Blewett and others, 2009). Hammond and others (2009) combined data from GPS, interferometric synthetic aperture radar (InSAR), and paleoseismic studies to estimate the effects of post-seismic relaxation from earthquakes in the Central Nevada seismic belt on raw GPS

velocity data. They reasoned that removing these transients from the GPS data would clarify the regional strain pattern in the northern Walker Lane. Their results indicate that the time-invariant (*i.e.*, longer-time, non-transient) deformation in the western Basin and Range is focused on the western part of the northern Walker Lane.

Hammond and others (2011) used data from additional GPS stations to study the velocities of a large number of crustal blocks located in the area of the northern Walker Lane (38.5°-40.5°N latitude, 117°-121°W longitude), and were able to distinguish five domains: [1] Sierra Nevada microplate, [2] Sierra Nevada/Walker Lane transition zone, [3] Walker Lane, [4] Basin and Range, and [5] North California shear zone (Figure 7). The North California shear zone is dominated by right-lateral displacement along the north-northeast edge of the SNGV block, and extends from the Mohawk Valley fault zone (Sawyer and others, 2005) on the southwest to the Honey Lake-Warm Springs-Pyramid fault zone to the northeast (*e.g.*, Wills and Borchardt, 1993; Wakabayashi and Sawyer, 2001; Wesnouski, 2005; Faults and others, 2005; Turner and others, 2008; Hinz and others, 2009; Briggs and Wesnousky, 2004). The study area of this thesis is primarily within their Sierra Nevada/Walker Lane transition zone, including part of the Sierra Nevada-Great Valley block and North California shear zone.

Sierra Nevada-Great Valley Block.

The Sierra Nevada-Great Valley block (SNGV) is a 600 km long block of continental crust that is tilted to the west and is bounded by faults associated with the San

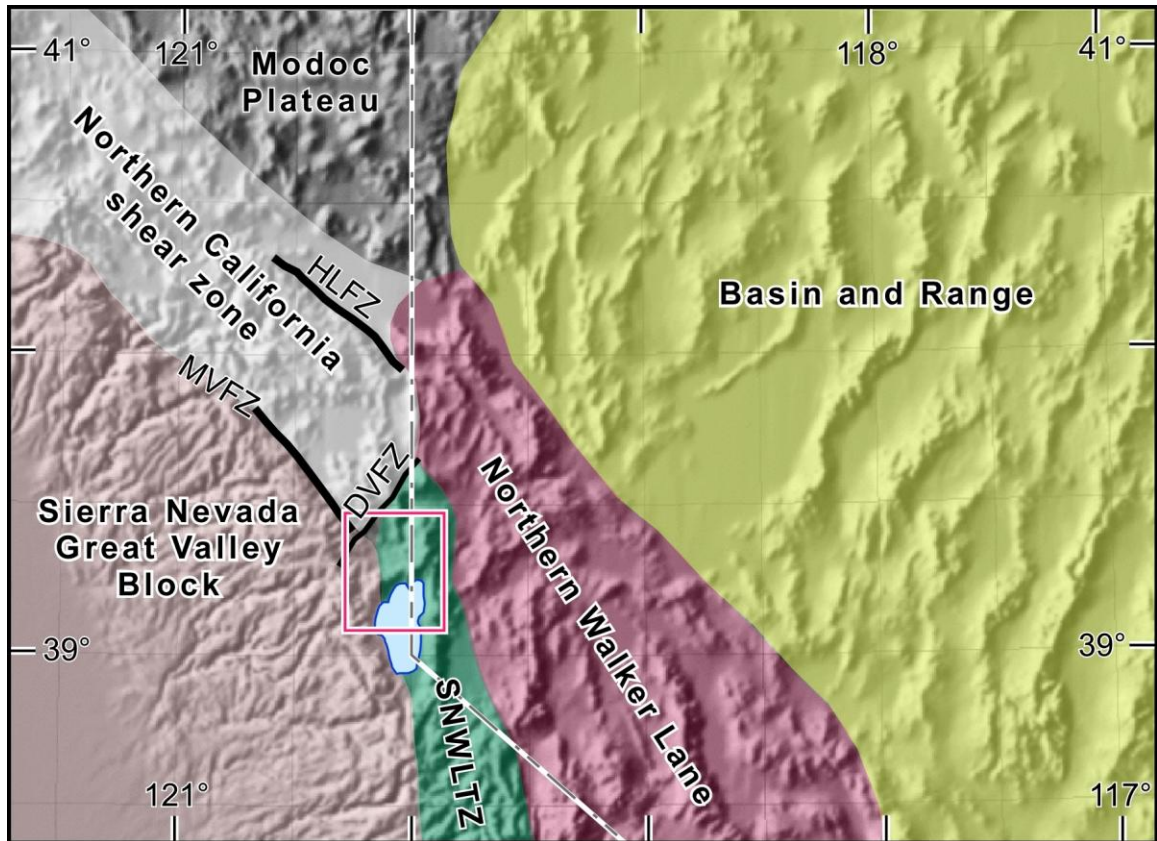


Figure 7. Primary structural domains based on GPS velocities and block modeling by Hammond and others (2001). Location of study area is approximated by the red rectangle. HLFZ = Honey Lake fault zone, MVFZ = Mohawk Valley fault zone, DVFZ is Dog Valley fault zone, SNWLTZ = Sierra Nevada-Walker Lane Transition Zone.

Andreas fault system and the Walker Lane (Figure 6). The core of the SNGV is composed of Paleozoic and Mesozoic sedimentary and volcanic rocks intruded by Mesozoic granitic rocks (Bateman and Wahrhaftig, 1966; Bateman and Eaton, 1967; Le and others, 2007, p. 242). This core is overlain by Cenozoic rhyolite tuffs, andesites, andesitic mudflows, and volcanic sedimentary rocks (Bartow, 1979; Wagner and others, 1981; Saucedo and Wagner, 1992; Wakabayashi and Sawyer, 2001). The SNGV extends northward just beyond 40°N latitude, where its elevation decreases and a structural and petrologic transition occurs with the Cenozoic volcanics of the Klamath

Mountains (Wakabayashi and Sawyer, 2001). The SNGV is moving toward N~40°-45°W at ~13-14 mm/yr relative to the cratonic center of North America (Dixon and others, 2000; Schweickert and others, 2004), with the Basin and Range Province extending between the two.

During the past 100 Myr, the Sierra Nevada mountains have experienced two dominate episodes of uplift and erosion. First, transpressional fault zones caused exhumation and erosion along the leading edge of a Mesozoic volcanic arc (Wakabayashi and Sawyer, 2001). Second, extension of the Basin and Range province during the late Cenozoic might have facilitated uplift and westward tilting of the Sierra Nevada due to footwall unloading along the Sierra Nevada frontal fault zone (Thompson and Parsons, 2009). The primary driver of uplift and potassic volcanism in the southern Sierra Nevada is interpreted to be delamination of the lower continental crust during the late Cenozoic (Wernicke and others, 1996; Ducea and Saleeby, 1998; Manley and others, 2000; Wakabayashi and Sawyer, 2001; Farmer and others, 2002; Saleeby and Foster, 2004; Figueroa and Knott, 2010). Figueroa and Knott (2010) suggest that crustal delamination was important in initiating uplift in the Pliocene, and that deformation related to the San Andreas and Walker Lane/Sierra Nevada Frontal fault systems explain continued uplift from the late Pliocene to the present.

*Faults with Known or Suspected Quaternary Displacement Histories
Tahoe-Sierra Frontal Fault Zone*

The Tahoe-Sierra Frontal fault zone (TSFFZ) is fault #518 on the Fault Activity Map of California (Jennings and Bryant, 2010) and is included in the USGS Quaternary Fault and Fold Database of the United States (Figure 4). The TSFFZ is marked

topographically by a NNW-trending geomorphic lineament with a down-to-the-east step, extending from just east of McKinney Bay toward the west end of Donner Lake. The TSFFZ is interpreted to be part of the system of “frontal” faults that mark the eastern edge of the Sierra Nevada and the westernmost encroachment of Basin and Range extensional faulting. Displacement is thought to be normal to dextral-oblique. The most recent displacement along the TSFFZ is thought to be Quaternary, <1.6 Myr (Jennings and Bryant, 2010, citing Harwood and Fisher, 2002; McCaughey, 2003; Saucedo, 2005; and Schweickert and others, 2000). The TSFFZ appears on published geologic maps by Saucedo and Wagner (1992), Saucedo (2005), and Sylvester and others (2007).

West Tahoe-Dollar Point Fault Zone

The West Tahoe-Dollar Point fault zone (WTDPFZ) is fault #516 on the Fault Activity Map of California (Jennings and Bryant, 2010, citing work by Burnett, 1982; Franks, 1980; and Schweickert and others, 2000) and is included in the USGS Quaternary Fault and Fold Database of the United States (Figure 4). The WTDPFZ is one of the three fundamental fault zones in the Lake Tahoe Basin that displaces Holocene lakebeds as imaged by CHIRP surveys across Lake Tahoe (Kent and others, 2005; Brothers and others, 2009; Dingler and others, 2009). All three of these active faults are north-striking, normal down-to-the-east faults thought to be capable of generating magnitude 7 earthquakes.

The estimated vertical offset rate on the WTDPFZ is 0.43-0.81 mm/yr (Dingler and others, 2009). The most recent earthquake along this trend, investigated using CHIRP profiles and cores, is interpreted to have occurred ~3.5 to 10 kyr before present, with an average slip of 3.7 m along a 55 km trace during a M 6.9-7.4 earthquake (Brothers and

others, 2009). Sub-lacustrine normal faults capable of generating magnitude 7 earthquakes would result in significant tsunamis or seiches within the Lake Tahoe Basin (Ichinose and others, 2000; Kent and others, 2005). Ichinose and others (2000) estimated that 2.83 m of coseismic slip on the WTDPFZ would produce 10 m seiche waves in Lake Tahoe. Coseismic failure of an additional section of the sedimentary shelf on the west side of Lake Tahoe, similar to the McKinney slide of circa 60 ka, would add greatly to the height of tsunami or seiche waves, resulting in the devastation of the cities and towns surrounding Lake Tahoe.

The northward extension of the WTDPFZ is somewhat ambiguous. The active fault might continue northward along the N-trending Carnelian Bay fault segment, or it may turn NNW at Dollar Point on a segment that continues toward Truckee (Saucedo, 2005; Sylvester and others, 2007). The Carnelian Bay extension might be more consistent with normal faulting, while the more NNW-trend might be associated with more dextral-divergent oblique faulting, given the slip behavior of other faults in the area.

Agate Bay Fault

The Agate Bay fault is fault #101 on the Fault Activity Map of California (Jennings and Bryant, 2010) and is included in the USGS Quaternary Fault and Fold Database of the United States (Figure 4). The fault trace as mapped by Saucedo (2005) did not reach the shore, and is marked by a geomorphic lineament observable on maps derived from LiDAR and multibeam surveys of the lake floor (Gardner and others, 1998, 2000). There is a small onshore extension of the Agate Bay fault on the map by Sylvester and others (2007). Dingler and others (2009) analyzed over 400 km of high-resolution CHIRP data collected across Lake Tahoe, and did not find evidence of an active Agate Bay fault

displacing offshore sediments. Given the proximity of the inferred trace of the Agate Bay fault to the West Tahoe-Dollar Point fault zone, the Agate Bay fault might (if it exists) be a splay of the WTDPFZ. The most recent displacement of the (inferred but not observed) Agate Bay fault is thought to be Quaternary, <1.6 Myr (Jennings and Bryant, 2010, citing work by Saucedo, 2005, and Schweickert and others, 2000).

North Tahoe Fault

The North Tahoe fault was initially described by Birkeland (1963). It is fault #102 on the Fault Activity Map of California (Jennings and Bryant, 2010), and is included in the USGS Quaternary Fault and Fold Database of the United States as fault 1649 (Figure 4; Sawyer and Haller, 2000). The North Tahoe fault is one of the three normal faults imaged using CHIRP surveys across Lake Tahoe that displace Holocene lake sediments (Kent and others, 2005; Brothers and others, 2009; Dingler and others, 2009). The Western Boundary fault, Kings Beach fault, and State Line fault (Gardner and others, 2000) are considered splays of the North Tahoe fault (Sawyer and Haller, 2000). The North Tahoe fault coincides with the base of a ~430 m high escarpment near the deepest part of the floor of Lake Tahoe, as well as a 14 m scarp associated with deformed recent lake sediments adjacent to Dollar Point (Gardner and others, 2000; Sawyer and Haller, 2000). The strike azimuth of the North Tahoe fault varies by ~30° along its trace, from striking due north to northeast (Dingler and others, 2009). Along the seismic profile shown as figure 7 in Dingler and others (2009), the top of the McKinney Bay landslide debris (emplaced ~60 kyr) is offset by 21 m along the North Tahoe fault. They estimate the rate of vertical offset on the North Tahoe fault to be 0.35-0.60 mm/yr. Geophysical profiling indicates that the North Tahoe fault might terminate near the middle of the

Tahoe Basin. The most recent displacement along the fault zone is Holocene, <15 ka (Hyne and others, 1972; Gardner and others, 2000; Sawyer and Haller, 2000; Jennings and Bryant, 2010; and Saucedo, 2005).

Incline Village Fault

The Incline Village fault was initially described by Hyne and others (1972), and is included in the USGS Quaternary Fault and Fold Database of the United States as fault 1650 (Figure 4; Sawyer, 1999a). The Incline Village fault is one of the three important normal faults imaged by CHIRP surveys in the Lake Tahoe Basin, which cut Holocene lakebeds (Dingler and others, 2009). The southern tip of the Incline Village fault appears to be in the middle of the Lake Tahoe basin, not far from the southern tip of the North Tahoe fault. The trend of the Incline Village fault offshore can be traced onshore, where a down-to-the-east scarp with up to ~5 m of local relief marks the fault line (Seitz, 2009). The average strike azimuth of the Incline Village fault is 22° (Sawyer, 1999a).

The most recent displacement along the fault zone is listed by the USGS as latest Quaternary, <15 ka, with a slip rate of between 0.2 and 1.0 mm/yr (Kumamoto and others, 1994; Sawyer, 1999a). Dingler and others (2009) estimate the vertical offset rate along the Incline Village fault at 0.12-0.30 mm/yr. Paleoseismic trenching by Seitz (2009) established the most recent displacement event along a strand of the Incline Village fault as dating from 1500 AD, and found that the last three large events in the last ~60 kyr resulted in displacements of from 3.5 to 4.2 m, indicating that earthquakes in the 6.8 to 7.4 range have occurred along the Incline Village fault. Ichinose and others (1999) attributed the M_w 4.9 earthquake of 30 October 1998 to the Incline Village fault, although there was no coseismic surface rupture. Ichinose and others (1999) characterized the

Incline Village fault zone as “a system of [northeast striking] southeast-dipping normal faults.” The epicenter for the main 30 October 1998 earthquake was 4 km north of the Incline Village fault, and their fault-plane solution had a strike of 33° , dip of 70°SE , and a rake of -15° (Ichinose and others, 1999).

East Tahoe Fault

The East Tahoe fault is included in the USGS Quaternary Fault and Fold Database of the United States as fault 1651 (Figure 4; Sawyer, 1999b). It is inferred to bound the east side of the Lake Tahoe Basin, where there is a steep ($>30^\circ$) escarpment that is ~1000 m high. Most of the inferred trace of the East Tahoe fault is below lake level. Whether seismic reflection profiles can be interpreted to include a fault along the eastern edge of the Lake Tahoe Basin still somewhat problematic (*e.g.*, Gardner and others, 1998, 1999, 2000) although magnetic data were interpreted by Henyey and Palmer (1974) as supporting existence of an East Tahoe fault. Dingler and others (2009) did not include an active fault along the East Tahoe trend, based on their interpretation of CHIRP data collected in the lake basin. The trace of the fault might be masked by debris flow deposits and fan material shed off the east side of the lake basin (Hyne and others, 1972; Schweickert and others, 1999). The average strike of the fault is inferred to be north, with a west dip, based on the interpretation that the Lake Tahoe Basin is a graben. Dingler and others (2009) interpret the Lake Tahoe Basin to be a half graben without a bounding fault to the east. The most recent displacement along the fault zone, if it exists at all, is speculated to be Quaternary, <1.6 Myr (Sawyer, 1999b).

Polaris Fault

The Polaris fault was discovered in 2008 during geotechnical investigations of the area around the Martis Creek Dam, which had been experiencing unacceptable levels of seepage. The US Army Corps of Engineers acquired LiDAR data from the Truckee-Donner Public Utility District in order to make a detailed topographic map of the area at a contour interval of 2 feet, along with ortho-rectified aerial photographs of the area. “During the initial inspection of these data a prominent lineament was observed to cross the East Martis Creek Fan...and was judged to likely be a fault related scarp” (Hunter and others, 2010, p. 286). Field studies of the geomorphic feature were initiated, resulting in the recognition of a youthful shear zone they called the Polaris fault.

Cronin’s presentation at the 2009 National Meeting of the Association of Environmental and Engineering Geologists in Lake Tahoe included a slide showing a seismo-lineament in the Truckee area that he could not correlate with any fault on a published map. He had included the slide to demonstrate that the SLAM method might not always work. In the audience was USGS geologist Gerald Bawden, who had analyzed the LiDAR data used to discover the Polaris fault. After the presentation, Bawden told Cronin that the seismo-lineament seemed to spatially correlate with the Polaris fault, whose discovery was being announced at that very meeting (Hunter and others, 2009) but had not yet been announced in the peer-reviewed literature (Hunter and others, 2011).

The Polaris fault was not an entirely unknown structural trend. At that same meeting, Aaron Melody presented results from his MS thesis at Humboldt State University, in which he hand-trenched a fault in Hobart Meadow, ~10 km north of

Truckee and ~4 km NNW of the Prosser Creek reservoir. He initiated his work based on mapping by Olig and others (2005a, b) that mapped the “Truckee fault zone (TFZ)...comprised generally of two zones: a western zone of linear northwest-striking, left-stepping faults and lineaments extending from Martis Creek to Independence Lake, and an eastern zone of north-striking faults and lineaments extending from the east flank of Alder Hill north to Kyburz Flat.” It was this fault zone that Melody sought to understand through a paleoseismic trench study.

Melody (2009) found a near-vertical fault with 1.25 m of down-to-the-east displacement. He interpreted a flower structure along the fault, suggesting that the vertical displacement might be related to overall horizontal shear on a slightly non-planar fault surface; however, he was not able to determine any sense of horizontal relative motion across the fault. Based on isotopic dating of a displaced ash bed, Melody (2009) inferred that the most recent displacement of the fault was <7 kyr. Melody’s trench is along the line of the Polaris fault of Hunter and others (2011).

Olig and others (2005a) described a trend they called the Sierra Nevada fault zone (SNFZ) extending “for 30 km from the northern end of the West Tahoe-Dollar Point Fault in Martis Valley up to Independence Lake, where a 5-km-wide stepover separates it from the [Mohawk Valley fault zone]. The SNFZ is characterized by overall normal-dextral, down-to-the-east slip...” They infer a maximum credible earthquake magnitude of 6.0 to 7.3, and “weighted mean slip rates from 0.03 to 2.4 mm/yr.” At least part of the SNFZ appears to be coincident with the Polaris fault.

The Polaris fault as currently mapped (Figure 4) is a 35-km-long right-lateral strike-slip fault that is thought capable of producing a magnitude 6.4-6.9 earthquake. Hunter

and others (2011) attribute a Holocene slip rate of 0.4 ± 0.1 mm/yr to the fault. They interpret the Polaris fault as being distinct from the Mohawk Valley fault zone, whose southeastern tip is <5 km beyond the northwest tip of the Polaris fault. The northern tip of the Carnelian Bay fault is ~2 km south of the southeastern tip of the Polaris fault, so the Polaris fault might be interpreted as a mixed or transitional structural trend that connects the normal faulting of the West Tahoe-Dollar Point fault zone with the dextral faulting of the North California shear zone (Figures 4 and 7).

Dog Valley (Steadman) Fault Zone

The Dog Valley fault zone (DVFZ) is fault #99 on the Fault Activity Map of California (Jennings and Bryant, 2010) and is included in the USGS Quaternary Fault and Fold Database of the United States (Figures 4 and 7). The most recent displacement along the DVFZ is historic, associated with the 1966 Truckee earthquake (Kachadoorian and others, 1967; Hawkins and others, 1986; Jennings and Bryant, 2010, citing work by Carter, 1966, and Grose, 2000a). Hawkins and others (1986) are referenced in the 2025 General Plan for the Town of Truckee, California, (<http://www.townoftruckee.com/index.aspx?page=470>), which states “that the Dog Valley fault and Mohawk Valley faults could result in a maximum credible earthquake of 6.75 and 7.0 magnitude, respectively.”

Hawkins and others (1986) conducted studies in the Truckee area “to assess the seismic hazards posed to four [US Bureau of Reclamation] dams (Stampede, Prosser Creek, Boca, and Lake Tahoe.” They considered the Genoa, West Tahoe, Last Chance, Mohawk Valley and Dog Valley faults to be the most likely seismic sources. They considered the DVFZ to be “the most seismically active fault in the study area (Ryall and

VanWormer, 1980; VanWormer and Prestly, 1978).” Hawkins and others (1986) referred to the DVFZ as a “concealed” left-lateral strike-slip fault “delineated by a pronounced topographic lineament on a regional scale, but on detailed examination, no geomorphic evidence of late-Quaternary surface displacement was found... Exploratory trenching of landforms suspected to be fault related did not reveal evidence of surface fault displacement.” They attributed the M_L 6.0 earthquakes in 1966 and 1948 and the M 3.6-4 earthquakes in July 1983 to the DVFZ, but noted that “no surface fault displacement occurred” although some ground rupture was noted in the 1966 event (Kachadoorian and others, 1967).

Mohawk Valley Fault Zone

The Mohawk Valley fault zone (MVFZ) was initially described by Turner (1897). It is fault #98 on the Fault Activity Map of California (Jennings and Bryant, 2010) and is included in the USGS Quaternary Fault and Fold Database of the United States as fault 25a,b (Figures 4 and 7; Sawyer, 1995a,b). The MVFZ marks the northern edge of the Sierra Nevada/Great Valley block and the southern edge of the North California shear zone of Hammond and others (2011) and the Pyramid Lake domain of the northern Walker Lane (Stewart, 1988). Although the MVFZ is mapped outside of the study area for this thesis, three faults in the thesis area seem to extend toward it and might merge with it, including the Tahoe-Sierra fault zone, the West Tahoe-Dollar Point fault zone, and the Polaris fault.

The MVFZ is described as a “high-angle, normal to dextral-divergent fault zone that extends along the eastern side of the northern Sierra Nevada and across parts of Sierra and Mohawk valleys. The total vertical offset across the fault is 500 to 1,800 m

based on the amount of vertical separation of the Mehrten Formation and Lovejoy Basalt” (Sawyer, 1995a,b; Page and Sawyer, 1992; Sawyer and Page, 1993). The average strike of the MVFZ is 318° to 322° (Mohawk Valley segment) and 322° to 333° (Sierra Valley segment), dipping 55°E to vertical. The most recent displacement along the MVFZ is thought to be latest Quaternary, <15 ka (Sawyer, 1995a,b; Jennings and Bryant, 2010, citing work by Grose, 2000b,c; Hawkins and others, 1986; Saucedo, 1992; and Sawyer and others, 1993).

Summary

The local tectonic setting of the thesis study area is complex. The complexity is reflected by variety of focal mechanisms in this area, including strike-slip, normal, and oblique-slip events that are typical of a transtensional structural setting (e.g., Schweickert and others, 2004). The North California shear zone to the northwest of the study area is dominated by right-lateral shear on northwest-striking faults. In the Truckee area, evidence from the 1966 Truckee earthquake indicates left-lateral shear on northeast-striking faults, possibly conjugate to the North California shear zone faults (Schweickert and others, 2004). Several north-striking faults in the Lake Tahoe Basin display evidence of normal (east down) displacement. Some earthquakes are interpreted to be related to magma injection (Smith and others, 2004), adding to the variety of possible structural interpretations of shallow-focus earthquakes.

CHAPTER THREE

Methods

Selection of Study Area

The boundaries of the geographic area within which this study was conducted were chosen to take advantage of published earthquake focal mechanism solutions, geologic maps, and paleoseismology studies, as well as the presence of relatively good road access (Figure 1). Adjacent areas to the west and south were less conducive to this work, and include the Granite Chief Wilderness and the Desolation Wilderness areas of the Tahoe and Eldorado National Forests where access is limited. In this area, there is a mix of private land and public land in the Tahoe and Humboldt Toiyabe National Forests that are traversed by a relatively dense system of trails, gravel or paved roads, and highways including Interstate 80.

DEM Acquisition and Conversion

Digital elevation data for twenty 7.5' quadrangles generated by the U.S. Geological Survey (USGS) were obtained from GIS (Geographic Information Systems) Data Depot (data.geocomm.com/dem/demdownload.html) of the area between north latitudes 39° and 39.625° and west longitudes 120.375° and 119.875° (Figure 2). The data were downloaded in compressed form as a zipped tar file directly from the GIS Data Depot, and the application *WinZip* was used to unpack the compressed files. The resulting elevation data were in Spatial Data Transfer Standard (SDTS) format. The files were converted from their original format to a Digital Elevation Model (DEM) using the

Windows application *SDTS2DEM*, available free from GIS Data Depot (data.geocomm.com/dem/sdts2dem.html).

The resulting DEM files were suitable for input to the *ArcGIS* software, through which they were converted to raster files. In the Arc Toolbox, the *conversion* toolset is opened and the *DEM to raster* tool is selected. The DEM file to be converted is then selected, and the conversion process is run. *ArcGIS* automatically includes the resulting raster file in the table of contents, making it visible and available for other processes.

The twenty individual raster files were then combined into a single raster file. In order to stitch the raster files together, the pixel type, cell size, and coordinate system must be known and the same for all rasters. In this study, the pixel type was floating point, the cell size was 10 meters, and the coordinate system was UTM (zone 10N). In the Arc Toolbox, the *Mosaic to New Raster* tool is selected from (in sequential order) the *Data Management*, *Raster*, and *Raster Dataset* menus. The *Mosaic to New Raster* tool allows the combination of all raster files in one step. In the *Mosaic to New Raster* window, a drop-down box contains all raster data currently in the *ArcMap* table of contents. Add all desired rasters into the tool window as well as all necessary data characteristics. Information required for input into the *Mosaic to New Raster* window can be found by navigating to one of the raster files in the *ArcMap* table of contents, right clicking, selecting properties, and opening the *Source* tab. Once all required fields are completed, click *ok* in the *Mosaic to New Raster* window to execute the tool. The result of this process is a composite raster file of the greater northwest Tahoe area.

The composite raster file must be converted to a composite *ASCII* file before the elevation data can be used in the SLAM process, as implemented by the current

Mathematica code (Cronin and others, 2008; Cronin, 2011; see Appendix ____). Within the *Arc Toolbox*, choose *Conversion Tools* and select the *Raster to ASCII* tool. The input file is the composite raster just created, and a folder/directory for the resulting text file must be chosen. The conversion process is initiated by selecting *run*. The ASCII file has a .txt extension, and displays the elevation data as numerical values that can be opened in any text editor program.

The text file at this stage has to be converted to a .dat file, so the data can be used in the SLAM *Mathematica* code. Using a PC, the .txt file can be opened using the *Notepad* text editor. The .txt file will display a header with columns and rows of numerical values. To make the conversion, save the opened .txt as a .dat using *all files* instead of *text document files* in the *save as type* drop down box, and select *save*. A .dat file is a data file than can easily store data as text, and does not alter the structure of the dataset.

The final DEM data file has the .dat suffix, and has the following structure (after Cronin and others, 2008; Maune, 2001). The first six records are two columns wide, with alpha characters in the first column and numbers in the second column. The alpha characters are labels for the adjacent values; for example, the abbreviation in row 1 column 1 identifies or describes the numeric value in row 1 column 2. The header information in the first six records includes the number of columns (*ncols*) in the dataset, the number of records (*nrows*) from record 7 to the end of the data, the UTM coordinates of the lower left corner (*xllcorner* and *yllcorner*) of the DEM area, the horizontal distance between adjacent elevation data points (*cellsize*), and the default value for any cell that does not have an elevation observation associated with it (*NODATA_value*). The remainder of the dataset is a rectangular matrix *nrows* long and *ncols* wide containing

numeric elevation data. The 3D UTM coordinate of a given datum (z) is computed by knowing the row (i) and column (j) of the datum, the cellsize, and the UTM coordinates of the lower left corner:

$$\{(xllcorner + (cellsize (j - 1))), (yllcorner + (cellsize (nrows - i))), z\}$$

(Cronin and others, 2008, equation 1).

Earthquake Data Acquisition

Earthquake focal-mechanism data used in this study were obtained from the Northern California Earthquake Data Center (NCEDC) hosted by the University of California at Berkeley (<http://www.ncedc.org/ncedc/catalog-search.html>), moment tensor solutions from the Berkeley Seismological Laboratory catalog published online by Doug Dreger (<http://seismo.berkeley.edu/~dreger/solutions.new>), the USGS moment tensor and broadband source-parameter catalogs (<http://earthquake.usgs.gov/earthquakes/eqarchives/sopar/>), Ichinose and others (2003, Table 2, events 66 and 87), and Tsai and Aki (1970). Online searches were limited to $M \geq 3$ events from 1980 through 2009 with reported epicenters located within the study area: north latitude 39.08° - 39.45° and west longitude 120.28° - 119.85° . In the NCEDC search, the “Mechanism Catalog (1968-Present)” was queried. The USGS site allowed concurrent searches of several catalogs with focal-mechanism data, including the USGS National Earthquake Information Center (NEIC) first-motion and moment-tensor catalogs and the Global CMT (centroid moment tensor) catalog (<http://www.globalcmt.org/CMTsearch.html>).

Focal mechanism solutions for total of 29 earthquakes were acquired (Table 1). Multiple solutions were available for 12 earthquakes, either generated by different researchers or by routines like FPFIT that can yield several results that are consistent with

Table 1. Earthquakes used to generate seismo-lineaments.

Earthquake Number	Date ID yyyyMMddhhmmss	Latitude °	Longitude °	Depth (km)	Magnitude	Horizontal Error (km)	Vertical Error (km)
1a	19800721101222	39.295	-120.145	11.43	3.05	0.3	1.0
1b	19800721101222	39.295	-120.145	11.43	3.05	0.3	1.0
2a	19830703124443	39.413	-120.209	10.65	3.60	0.2	0.6
2b	19830703124443	39.413	-120.209	10.65	3.60	0.2	0.6
3a	19830703150819	39.412	-120.206	11.05	4.00	0.3	0.8
3b	19830703150819	39.412	-120.206	11.05	4.00	0.3	0.8
3c	19830703150819	39.412	-120.206	11.05	4.00	0.3	0.8
3d	19830703150819	39.412	-120.206	11.05	4.00	0.3	0.8
4	19870502821958	39.403	-119.879	5.78	3.20	0.3	1.3
5	19881107101155	39.408	-120.218	9.45	3.10	0.2	0.5
6	19910102234438	39.130	-119.859	0.01	3.40	0.7	1.6
7	19920324113855	39.394	-119.990	0.14	3.45	0.5	0.6
8	19920830234208	39.413	-120.189	0.90	3.24	1.1	1.7
9	19930806003138	39.412	-120.176	0.02	3.07	0.8	1.0
10	19930809021908	39.399	-120.211	10.08	3.00	1.3	1.4
11a	19950408220618	39.286	-120.072	0.92	3.04	1.5	3.2
11b	19950408220618	39.286	-120.072	0.92	3.04	1.5	3.2
12	19960406230814	39.411	-119.961	6.95	3.04	0.4	1.0
13a	19980115151215	39.425	-120.183	5.00	3.60	1.0*	1.0*
13b	19980115151215	39.431	-120.174	0.04	3.77	0.3	0.3
13c	19980115151215	39.431	-120.174	0.04	3.77	0.3	0.3
13d	19980115151200	39.440	-120.170	9.00	3.80	1.0*	1.0*
14a	19981030095330	39.303	-119.977	14.20	5.30	1.0*	1.0*
14b	19981030095300	39.310	-119.980	11.00	4.74	1.0*	1.0*
15	19981030095332	39.284	-120.045	2.41	4.80	0.3	0.4
16	19981030101110	39.292	-119.989	13.51	3.05	0.8	1.9
17	19981204005736	39.311	-119.993	0.17	3.47	0.5	0.5
18a	20000206023117	39.328	-120.030	2.25	3.46	0.4	1.9
18b	20000206023117	39.328	-120.030	2.25	3.46	0.4	1.9
19	20010529062109	39.300	-119.976	9.34	3.01	0.4	0.9
20a	20010707073355	39.298	-120.001	1.39	3.67	0.4	2.6
20b	20010707073355	39.298	-120.001	1.39	3.67	0.4	2.6
21	20010707073953	39.296	-119.977	9.58	3.20	0.5	1.0
22a	20011030044320	39.298	-120.002	6.06	3.03	0.4	1.5
22b	20011030044320	39.298	-120.002	6.06	3.03	0.4	1.5
23	20040603082538	39.336	-120.012	5.19	3.04	0.2	1.1
24a	20040603085446	39.333	-120.006	5.80	4.50	1.0*	1.0*
24b	20040603085446	39.334	-120.008	5.24	4.20	0.2	0.9
25	20040612144942	39.407	-120.213	2.20	3.65	0.2	2.4
26	20040612150419	39.407	-120.211	1.06	3.40	0.2	7.2
27a	20050626184558	39.305	-120.093	0.09	4.77	0.6	2.8
27b	20050626184558	39.305	-120.093	0.09	4.77	0.6	2.8
27c	20050626184557	39.310	-120.067	7.10	5.20	1.0*	1.0*
28	20091223045955	39.317	-119.987	3.58	3.49	0.3	0.8
29	19660912164103	39.438	-120.160	10.00	6.00	1.0	2.0

*Uncertainty magnitude not reported; value assumed.

Table 1. Earthquakes used to generate seismo-lineaments, continued.

Earthquake Number	Strike A	Dip Az A	Dip Angle A	Rake A	Strike B	Dip Az B	Dip Angle B	Rake B	Source
1a	360	90	70	-120	239	329	36	-36	1
1b	145	235	45	170	242	332	83	45	1
2a	160	250	15	-90	340	70	75	-90	1
2b	110	200	45	170	207	297	83	45	1
3a	330	60	25	-140	203	293	74	-70	1
3b	105	195	75	160	200	290	71	16	1
3c	150	240	40	-50	282	12	61	-118	1
3d	185	275	55	-50	309	39	51	-133	1
4	170	260	35	-60	315	45	60	-109	1
5	175	265	30	-70	332	62	62	-101	1
6	45	135	70	-10	138	228	81	-160	1
7	25	115	45	-50	155	245	57	-123	1
8	210	300	55	-10	306	36	82	-145	1
9	55	145	90	-30	145	235	60	-180	1
10	120	210	60	140	233	323	56	37	1
11a	105	195	80	120	212	302	31	19	1
11b	55	145	60	80	254	344	31	107	1
12	160	250	55	-90	340	70	35	-90	1
13a	57	147	89	60	325	55	30	178	2
13b	110	200	60	120	241	331	41	49	1
13c	355	85	75	160	90	180	71	16	1
13d	223	313	89	-47	314	44	43	-179	3
14a	32	122	88	-1	122	212	89	-178	4
14b	125	215	83	-169	34	124	79	-7	3
15	40	130	60	-10	135	225	81	-150	1
16	15	105	75	-10	108	198	80	-165	1
17	135	225	60	-150	29	119	64	-34	1
18a	350	80	90	70	260	350	20	180	1
18b	170	260	75	-50	277	7	42	-157	1
19	20	110	75	10	287	17	80	165	1
20a	180	270	80	-40	278	8	51	-167	1
20b	280	10	60	170	15	105	81	30	1
21	190	280	85	-30	283	13	60	-174	1
22a	120	210	45	-160	16	106	76	-47	1
22b	175	265	40	-40	298	28	66	-123	1
23	135	225	40	-120	352	82	56	-67	1
24a	354	84	54	-62	132	222	44	-123	4
24b	125	215	50	-130	358	88	54	-53	1
25	55	145	75	-20	150	240	71	-164	1
26	65	155	90	-40	155	245	50	-180	1
27a	45	135	85	10	314	44	80	175	1
27b	90	180	30	-90	270	360	60	-90	1
27c	230	320	86	-14	321	51	76	-176	4
28	115	205	60	-140	2	92	56	-37	1
29	44	134	80	0	314	44	90	170	5

Sources: 1=NCEDC online catalog; 2=USGS online catalog; 3=Ichinose and others, 2003; 4=Dreger online catalog; 5=Tsai and Aki, 1970

the input data. FPFIT is a FORTRAN program that finds “best fit” double-couple fault-plane solutions for a given set of P-wave first-motions (Reasenber and Oppenheimer, 1985). Earthquakes with similar origin times and locations were considered distinct events if they were assigned different ID numbers by the Northern California Earthquake Center at Berkeley. All of the 45 focal mechanism solutions compiled in Table 1 were analyzed in this study.

Analysis

Seismo-Lineament Analysis

A seismo-lineament is a swath across the ground surface, as represented by a hillshade map derived from a DEM, formed by the intersection of the ground surface and a nodal plane and its associated uncertainty volume (Cronin and others, 2008). Every earthquake focal mechanism solution has two nodal planes, oriented perpendicular to each other; consequently, two seismo-lineaments can be derived for any earthquake for which a focal mechanism solution has been computed (Figure 8; Cronin, 2004). One of the two nodal planes is coincident with the fault that produced the earthquake, and hence is called the fault-plane solution, and the other nodal plane is the auxiliary plane.

The vector normal to the auxiliary plane is parallel to the slip vector on the fault plane. If the focal data are accurate and the fault that generated the earthquake is approximately planar and emergent, the ground-surface trace of that fault should be evident within a seismo-lineament associated with that earthquake. Earthquakes that are

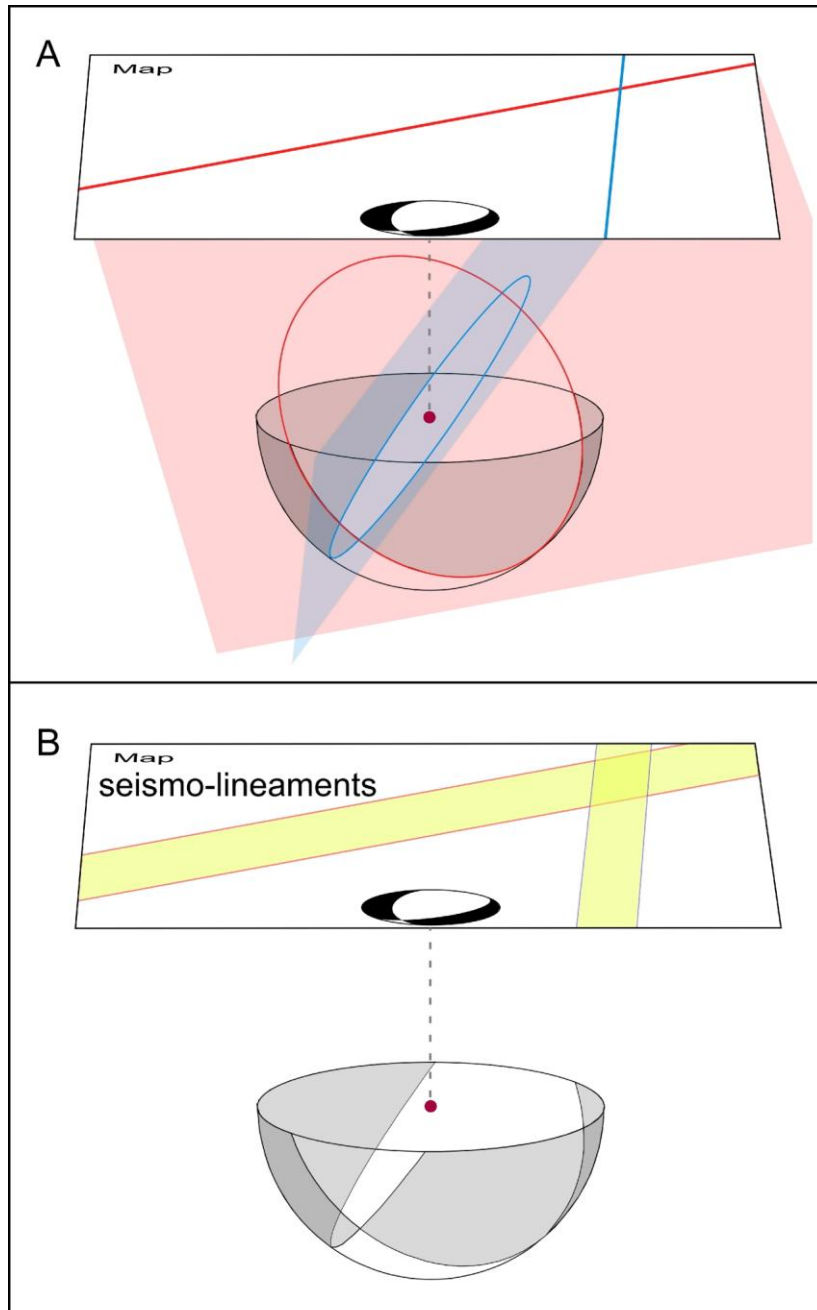


Figure 8. Perspective illustrations depicting seismo-lineaments, with focal mechanism diagram plotted on the horizontal map surface at the epicenter, directly above the focus (red circle). [A] Projection of two nodal planes (pink and blue) from the focus to the ground surface, resulting in the red and blue linear traces on the map. [B] Seismo-lineament swaths (yellow) reflect uncertainty in location of focus. After Cronin (2011b).

useful in delineating seismo-lineaments include events with well located foci, well constrained focal mechanism solutions that reflect a strong double-couple mechanism (*i.e.*, >~80% dc), and nodal planes that dip more steeply than ~25° (Cronin and others, 2008).

Seismo-lineaments were delineated using the 2010 version of the software application *SLAMCode.nb* written in *Mathematica* by Cronin (Appendix 1). The input data requirements for *SLAMCode.nb* include the following: (1) a properly formatted ASCII (text) file containing the DEM elevation data for the area around the epicenter, (2) the UTM zone, (3) the location of the earthquake focus – latitude, longitude, depth in kilometers, (4) the horizontal and vertical uncertainty in the focal location, in kilometers, and (5) the trend and plunge of the dip vector of each of the two nodal planes from the focal mechanism solution. Text lines within *SLAMCode.nb* provide a detailed explanation of how the code operates on the input data, while a general explanation is given by Cronin and others (2008) and Cronin (2011b). The output datafiles include a jpeg image of the hillshade map showing the boundaries of both seismo-lineaments, as well as separate jpeg images of both individual seismo-lineaments illuminated perpendicular to the lineament trends.

The seismo-lineament code used in this thesis to define the boundaries of each seismo-lineament used a cylindrical uncertainty region around the earthquake focus (Figure 9), as described in Cronin and others (2008). The version of the *SLAMCode.nb* that is current as of September, 2011, allows the user to choose either a cylindrical or an elliptical uncertainty region around the earthquake focus (Cronin, 2011a). The elliptical region has axes that are vertical and horizontal, with the vertical semi-major axis equal to

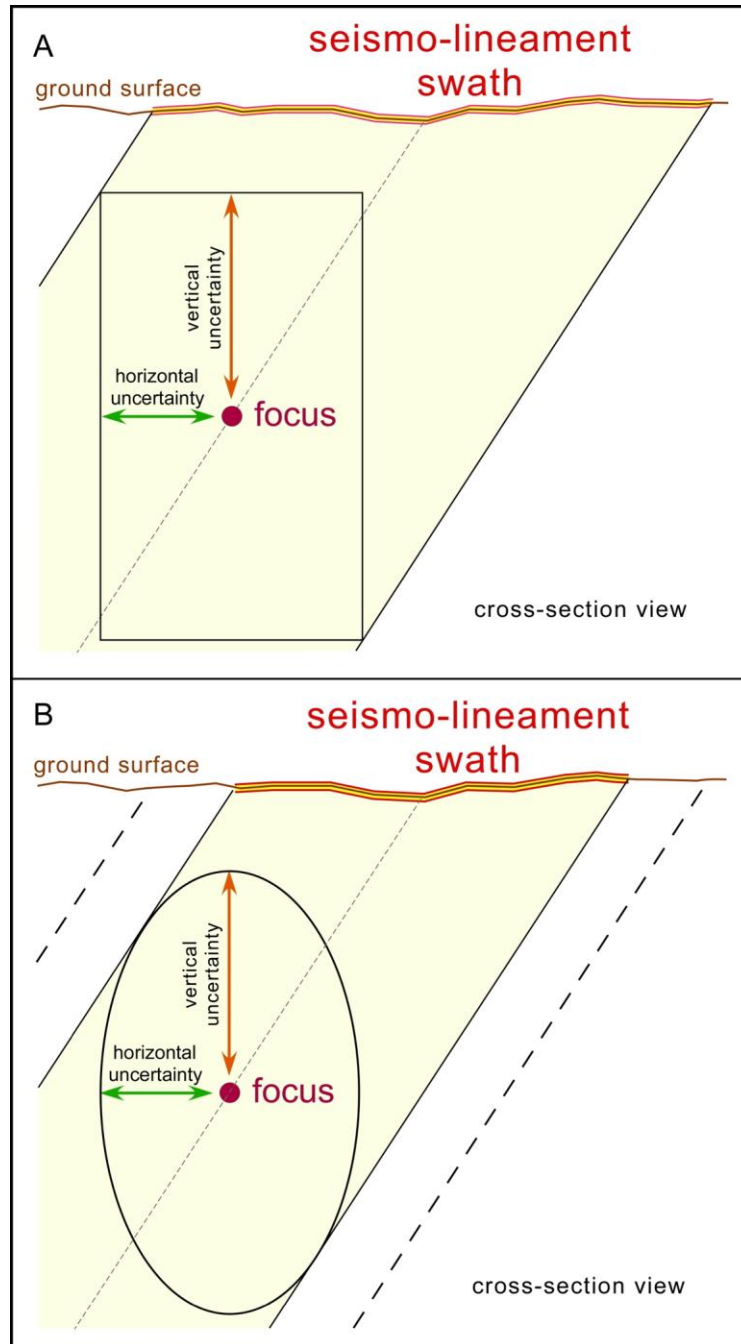


Figure 9. Cross sections depicting uncertainty in location of nodal plane (short-dashed line) based on uncertainty in focal location. [A] Nodal-plane uncertainty envelope and corresponding seismo-lineament swath based on cylindrical uncertainty region around focus, as used in this thesis. [B] Uncertainty envelope and seismo-lineament swath based on ellipsoidal uncertainty region. Long-dashed lines depict the envelope for the cylindrical case. After Cronin and others (2008) and Cronin (2011a,b).

the reported vertical uncertainty and the horizontal semi-major axes equal to the reported horizontal uncertainty.

The width of the swath for vertical nodal planes is the same whether the cylindrical or elliptical uncertainty volume is used, as would be the swath width for horizontal nodal planes (which are not used for obvious geometric reasons). Using the ellipsoidal uncertainty region for inclined, non-vertical planes would yield narrower seismo-lineament swaths. For example, the swath for a plane dipping 45° and an uncertainty region whose vertical uncertainty is twice the horizontal uncertainty would be ~25% narrower over a horizontal ground surface using the ellipsoidal rather than the cylindrical uncertainty region around the focus (Cronin, personal communication, 2011). The cylindrical uncertainty region yields a more conservative, wider seismo-lineament swath.

Geomorphic-Lineament Analysis

A long, collinear or slightly curving array of geomorphic features that are not related to human activities is called a *geomorphic lineament* (definition adapted from Cronin and others, 1993). A fault that propagates until it reaches the ground surface will be marked by geomorphic features developed along the fault trace related to the shear deformation of the ground surface. A near-planar fault surface will generate a gently curved or near-linear intersection with the ground. Near-vertical faults tend to generate strongly linear arrays of geomorphic features. The shape of the ground-surface trace of gently inclined faults can be complicated by erosion or by emergence through pre-existing high-relief topography. While not all geomorphic lineaments coincide with faults, an emergent seismogenic fault is very likely to generate a geomorphic lineament along its trace.

A total of 45 focal mechanism solutions were compiled for earthquakes with epicenters located in the study area, so 90 seismo-lineament swaths were mapped (Figure 10). The swaths to some gently inclined nodal planes plotted outside of the study area, and were not investigated further.

A hillshade map of each seismo-lineament swath was illuminated perpendicular to the strike of the nodal plane, at an angle of $\leq 45^\circ$ to horizontal, to accentuate geomorphic lineaments that trend subparallel to the seismo-lineament. This process was completed in the *ArcGIS* environment for this thesis. (The *Mathematica* notebook *SeismoLinGeomorph.nb* (Cronin, 2011c) uses the same input data as *SLAMCode.nb* to produce hillshade images of seismo-lineaments illuminated at a low angle perpendicular to the nodal-plane strike.) Using either *ArcGIS* or a graphics application (*Adobe Illustrator* or *Canvas*), geomorphic lineaments were traced on the swath map. These lineaments function as hypotheses for the possible location of faults within the swath that might be parallel with the nodal plane.

The area inside the boundaries of the seismo-lineament swath was examined for geomorphic indicators of active faulting. Cronin and others (2008, *after* Ray, 1960; Miller, 1961; Wesson and others, 1975; Bonilla, 1982; Slemmons and dePolo, 1986; Cronin and others, 1993; McCalpin, 2009; and Burbank and Anderson, 2001) list the following geomorphic features that are potentially observable on a DEM-based hillshade map and that might be developed along a fault:

- Stream channels that are aligned on opposite sides of a drainage divide;
- Lower-order (smaller) stream channel aligned across a higher-order stream channel;
- An anomalously straight segment of a stream channel;
- Aligned straight segments of one or more stream channels;

- Lower-order stream channel whose trend is directed upstream relative to the higher-order stream it intersects, so water flowing from the smaller stream into the larger stream has to change directions through an obtuse angle;
- Abrupt changes in gradient along a stream channel;
 - A stream channel that steps down in the direction of flow, indicated by rapids or a waterfall (knickpoint);
 - A stream channel that steps up in the direction of flow, indicated by a pond;
- Apparent lateral deflection of an incised stream channel or floodplain;
- Abrupt changes in gradient along a ridge crest;
 - A ridge crest that steps down abruptly in the direction of decreasing elevation;
 - A ridge crest that steps up in the direction of decreasing elevation;
 - A saddle in the ridge crest;
- Apparent lateral deflection of ridge crest;
- Abrupt changes in the gradient of a surface localized along a narrow linear step (fault scarp);
- Benches or faceted spurs at the base of ridges that are apparently unrelated to coastal or fluvial erosion;
- A set of ridges in an *en echelon* array;
- A topographic basin along a linear trough (pull-apart basin, sag pond);
- A topographic hill along a linear trough (pop-up, pressure ridge); and
- A ridge across the mouth of a stream drainage that is not a glacial moraine (shutter ridge).

The seismo-lineament swaths were each compared with the surface trace of known faults (chapter 2; *e.g.*, Wagner and others, 1981; Saucedo and Wagner, 1992; Saucedo, 2005; Sylvester and others, 2007; Dingler and others, 2009; Brothers and others, 2009; Hunter and others, 2011; Quaternary Fault and Fold Database) to assess whether there might be a spatial correlation between the corresponding earthquake and a previously recognized fault. Potential spatial correlations were recognized when the mapped fault trace was located within the seismo-lineament swath, and the fault trace was approximately parallel to the surface trace of the nodal plane – that is, approximately parallel to the lateral boundaries of the seismo-lineament swath.

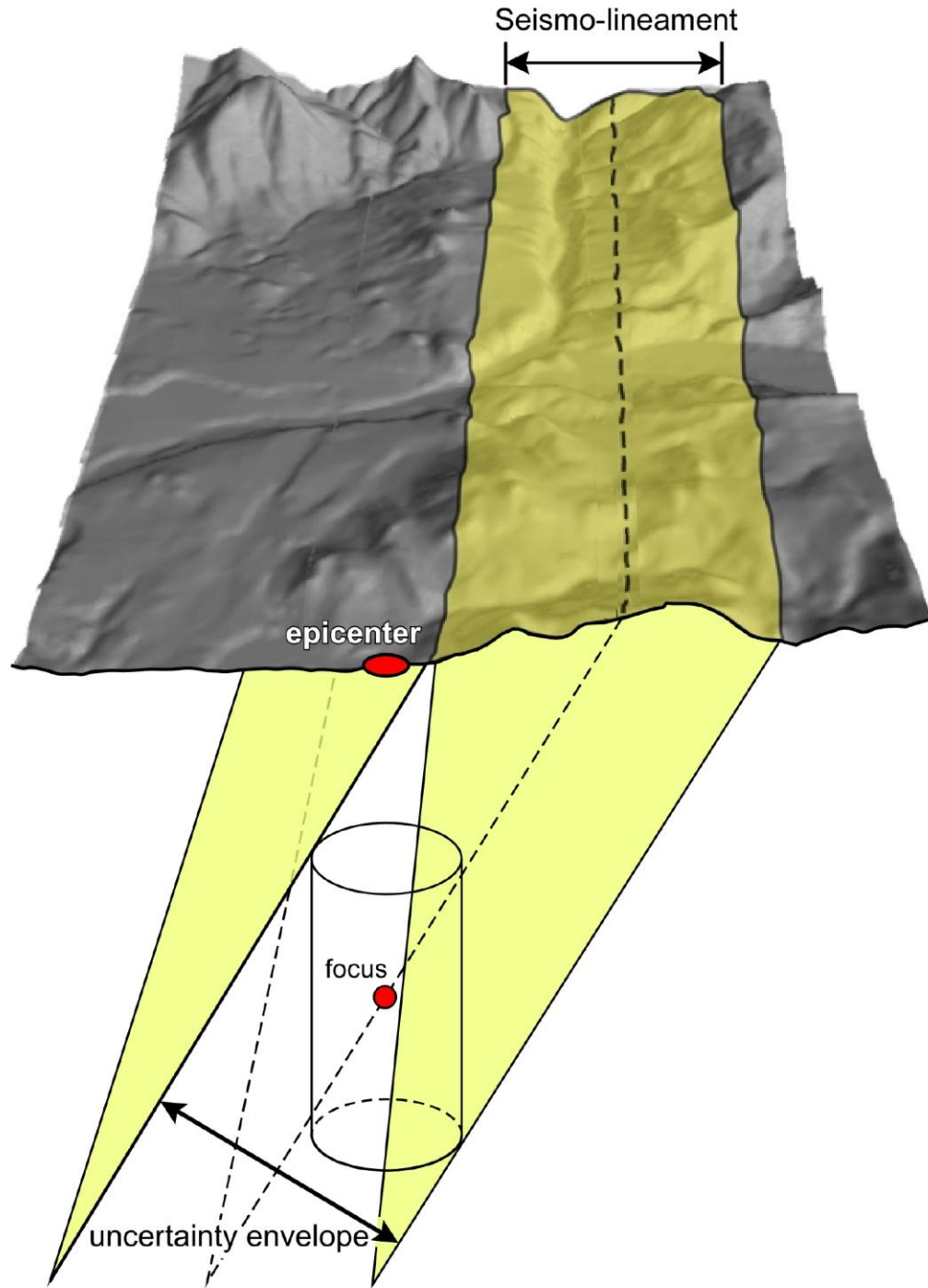


Figure 10. Perspective illustration of a seismo-lineament projected onto a hillshade surface constructed from a DEM. A linear valley parallel to the nodal-plane trace forms a prominent geomorphic lineament within the seismo-lineament.

Finally, each seismo-lineament for a given earthquake was assessed for its possible association with faulting, recalling that one of the two seismo-lineaments for each earthquake is associated with the auxiliary nodal plane and so is not coincident with the causative fault plane. Generally, this resulted in one of three outcomes: (1) the seismo-lineament does not appear to be related to either a mapped fault or any geomorphic indicators of active faulting; (2) the seismo-lineament is potentially related to a mapped fault within the seismo-lineament swath and whose surface trace is approximately parallel to the surface trace of the nodal plane; or (3) the seismo-lineament includes geomorphic indicators of faulting that are approximately parallel to the surface trace of the nodal plane but that are not associated with previously mapped faults. In rare instances, both or neither of the seismo-lineaments for a given earthquake appear to be spatially correlative with either a fault or with geomorphic indicators of faulting, in which case identification of the auxiliary plane is ambiguous prior to fieldwork.

Field Methods

The initial phases of the seismo-lineament analysis method (SLAM) generate hypotheses for where the surface trace of a seismogenic fault might be found. The focal mechanism data are used to establish the boundaries of the seismo-lineament swaths, and the geomorphic analysis is a search for geomorphic features that might have developed as a result of displacement along faults. The overall goal of fieldwork is to evaluate these hypotheses.

One of the nodal planes associated with a given earthquake is spatially coincident with the plane of the fault that generated the earthquake, and the other nodal plane is the auxiliary plane. A goal of field work is to collect sufficient additional data to discern

which nodal plane is more likely to be coincident with the fault plane. When there are geomorphic features observed within a seismo-lineament that are inferred to be developed along a fault, a goal of field work is to investigate whether a fault can be observed at the ground surface along that trend. When a fault is located within a seismo-lineament through previous published mapping or geomorphic analysis, a goal of field work is to locate that fault in the field and measure the fault's orientation as well as the orientation and slip sense of shear indicators along the fault, such as shear striae, grooves, drag folds, and displaced piercing points. Spatial correlation between the nodal plane and a fault is based on whether the ground-surface trace of the fault is within the corresponding seismo-lineament, whether the fault and nodal plane are approximately parallel, and whether the shear indicators observed in the field are approximately parallel to the corresponding shear vector on the nodal plane.

Data were collected whenever a fault was identified in the field to characterize the fault and to measure the orientation of the fault surface and the slip direction. The following data were collected at each site using a field notebook, hand-held GPS receiver, Brunton compass, and digital camera: [1] latitude and longitude of fault exposure or geomorphic feature; [2] photos of the fault trace or associated geomorphic features; [3] no less than 7 measurements of the strike and dip of the fault surface; [4] no less than 7 measurements of the orientation of shear striae on the fault surface; [5] general description of fault rock (type, thickness); [6] measurement of net slip or stratigraphic separation along the fault; and [7] general description of rock units adjacent to fault trace.

Faults that cut Holocene material typically feature a fault core bounded by shear-smoothed surfaces. The core of an exposed seismogenic fault will contain materials developed under conditions of low pressure and temperature, such as gouge, breccia, or cataclasite (*e.g.*, McCalpin, 2009; Yeats and others, 1997; Snoke and others, 1998). A damage zone of fractures and small shear surfaces often extends beyond the fault zone (Scholz, 2002; Sibson, 2003; Chester and others, 1993, 2004; Cronin and others, 2008). An exposed fault that lacks evidence of low PT faulting would not be a reasonable candidate as a seismogenic fault (Cronin and others, 2008).

Fisher Statistics

The spatial data collected along fault surfaces and geomorphic lineaments were subsequently compared with the corresponding earthquake nodal plane and slip vector to assess whether the earthquake might be spatially correlated with the observed fault. Fisher statistics were used to determine the mean orientation and associated 95% confidence interval for the fault surface and, if present, shear striae at each exposed fault encountered within the seismo-lineaments (Appendix 2; Cronin, 2008; Fisher, 1953). The focal mechanism data compiled for this study did not include uncertainty information for nodal-plane orientations.

The dip vector of a given nodal plane was plotted on a lower-hemisphere equal-area stereographic plot, with small circles of 10°, 20° and 30° radius around the vector. On the same stereonet were plotted the dip vectors of any fault surfaces located within the corresponding seismo-lineament, along with their 95% uncertainty region. A general assessment could then be made about whether the fault might reasonably be spatially

correlated with the nodal plane, based on whether the fault uncertainty region overlapped with the inner small circles around the nodal plane dip vector.

If a given fault appeared to be spatially correlated with the nodal plane, the slip vector associated with the nodal plane was plotted on a stereonet along with the mean orientation vector for shear striae on the fault surface. An assessment could then be made about whether the fault might reasonably be spatially correlated with the nodal plane, based on whether the uncertainty region around the mean shear vector overlapped with the inner small circles around the nodal plane slip vector.

If the fault is located within the seismo-lineament, and both the fault surface and the shear striae are approximately parallel to the corresponding nodal plane and slip vector, then the preliminary assessment is that the fault is spatially correlated with the earthquake. In other words, there is a reasonable possibility that the fault generated the earthquake. The strength of the correlation between the earthquake and a given fault within a corresponding seismo-lineament cannot be rigorously characterized because no uncertainty data have been published for the focal mechanism solutions.

CHAPTER FOUR

Results

Earthquakes

Data were compiled about 29 earthquakes, with reported magnitudes ranging from 3.00 to 6.0 (Table 1). Multiple focal mechanism solutions are available for eleven of these earthquakes, including two events that have four published solutions. Focal depths range from 0.02 km to 14.2 km, with focal depths reported at less than 2 km for ten different earthquakes. Earthquake 13 had reported depths of 0.04 ± 0.3 km (NCEDC, accessed 2011), 5.0 km (USGS, accessed 2011) and 9.0 km (Ichinose and others, 2003); similarly, earthquake 27 had reported depths of 0.09 ± 2.8 km (NCEDC, accessed 2011) and 7.10 km (Dreger, accessed 2011). The average elevation of the upper surface of Lake Tahoe is approximately 2.94 km, so the shallow focal depths would still be on the order of 3 km subsurface. Eleven of these events were separated from other earthquakes in the set by more than 9 months, while other events clustered temporally (Table 2).

Table 2. Earthquakes that cluster temporally

Earthquake Number(s)	Date(s)
2 & 3	July 3, 1983
7 & 8	March 24 & August 30, 1992
9 & 10	August 6 & 9, 1993
14, 15, 16 & 17	October 30 to December 4, 1998
19, 20, 21 & 22	May 20 to October 30, 2001
23, 24, 25 & 26	June 3 to 12, 2004

Focal mechanism diagrams were created for each of the 45 solutions given in Table 1, using a *Mathematica* application by Scherbaum and others (accessed 2011). This application provides the orientations of the axes of the focal mechanism solution in terms of their trend and plunge, with negative plunge indicating an upward-directed vector (Table 3). Zoback and Zoback (1980) note the general correspondence between the direction of T axes derived from earthquake focal mechanism solutions and the horizontal extension direction measured by various techniques in the field. The mean orientation of T axes from the earthquakes for which a single focal mechanism solution was available (*i.e.*, events 4-10, 12, 15-17, 19, 21, 23, 25, 26, 28, 29) has a trend of $79^{\circ} \pm 11^{\circ}$ and a plunge of $4^{\circ} \pm 11^{\circ}$ at the 95% confidence level. This is generally consistent with the east-west horizontal extension direction indicated for this area (Hammond and others, 2009, 2011; Kreemer and others, 2009).

Seismo-Lineaments

Seismo-lineaments corresponding to 45 focal mechanism solutions were delineated using a version of the *SLAMcode* application (Appendix 1) acting on the data from Table 1. All of the seismo-lineaments computed for this thesis are presented in Appendix 3. Some solutions (2a, 3a, 4) resulted in only one seismo-lineament within the study area, generally because the dip of the other plane was very small. Some solutions (6, 22b) resulted in one seismo-lineament that did not traverse the study area to a significant extent. In cases where two seismo-lineaments are functionally unavailable for assessment in the context of this research project, the nodal planes could not be differentiated to infer the fault plane. Most of the solutions resulted in two seismo-lineaments within the study area.

Table 3. Trend and plunge of the tensor axes of focal-mechanism solutions

Earthquake Number	P-axis		T-axis		N-axis	
	Trend °	Plunge °	Trend °	Plunge °	Trend °	Plunge °
1a	232	55	112	19	11	28
1b	5	24	114	36	249	44
2a	250	60	70	30	340	0
2b	330	24	79	36	214	44
3a	138	56	277	27	17	19
3b	153	3	62	25	250	65
3c	145	63	32	11	297	24
3d	154	58	248	2	339	32
4	185	69	59	13	325	17
5	218	71	70	16	338	10
6	3	21	270	7	162	68
7	11	62	268	7	174	27
8	174	30	73	18	317	54
9	6	21	104	21	235	60
10	177	2	85	48	269	42
11a	171	29	46	47	279	29
11b	152	14	300	73	60	9
12	70	80	250	10	340	0
13a	173	37	300	39	58	30
13b	179	10	69	62	274	26
13c	43	3	312	25	140	65
13d	168	32	279	30	42	43
14a	347	2	257	1	148	88
14b	350	13	259	3	157	77
15	2	27	264	14	149	59
16	332	18	241	4	139	72
17	350	41	83	3	176	49
18a	99	42	241	42	350	20
18b	120	45	231	20	338	38
19	334	4	243	18	76	72
20a	131	35	235	19	348	49
20b	144	14	242	27	29	59
21	142	24	240	17	1	60
22a	326	42	75	19	183	42
22b	164	56	51	14	313	30
23	313	69	66	9	159	19
24a	322	67	65	5	157	22
24b	328	60	62	2	153	29
25	12	25	103	3	200	65
26	12	27	118	27	245	50
27a	179	3	270	11	71	79
27b	180	75	0	15	90	0
27c	185	13	276	7	34	75
28	330	48	238	2	146	42
29	359	7	269	7	134	80

Positive plunge angles are directed downward.

The seismo-lineaments for the M4.2 earthquake of 3 June 2004 (#24a, Table 1) are typical of the results obtained from *SLAMCode.nb* (Figure 11; Dreger, accessed 2011). This earthquake has a reported focal depth of 5.8 km, and occurred on either [1] a normal oblique fault with minor left-lateral strike slip, oriented (strike & dip) 354°, 54°E, or [2] a normal oblique fault with minor right-lateral strike slip, oriented 132°, 44°SW. The swath associated with the first nodal plane extends northward from just east of Dollar Point across Agate Bay, passing through or just east of the Boca and Stampede Reservoirs, and encompasses parts of the North Tahoe fault and West Tahoe-Dollar Point fault zone (WTDPFZ). The North Tahoe fault and WTDPFZ are inferred to be a normal fault systems that dips east ~60° (Dingler and others, 2009; Kent and others, 2005), so there is good spatial correlation between these Late Neogene fault systems and the June 2004 earthquake. The second swath extends from north of Washoe Lake northwest across Sunflower Mountain, passing through Stampede Reservoir and possibly including faults just north of the Mohawk Valley fault zone at the far northwest edge of the study area. The most important correlations of earthquakes and faults are presented in Chapter 5 of this thesis.

Geomorphic Lineament Analysis

Geomorphic lineaments that trend approximately parallel to the seismo-lineament were identified within each of the seismo-lineament swaths. The geomorphic lineaments from all swaths are compiled in figure 12. Some of the geomorphic lineaments are coincident with the trace of previously mapped faults, while others are not. Geomorphic lineaments mapped within seismo-lineament swaths coincide with all or part of the traces of the following Late Neogene fault zones: the Sierra Nevada frontal fault zone, the West

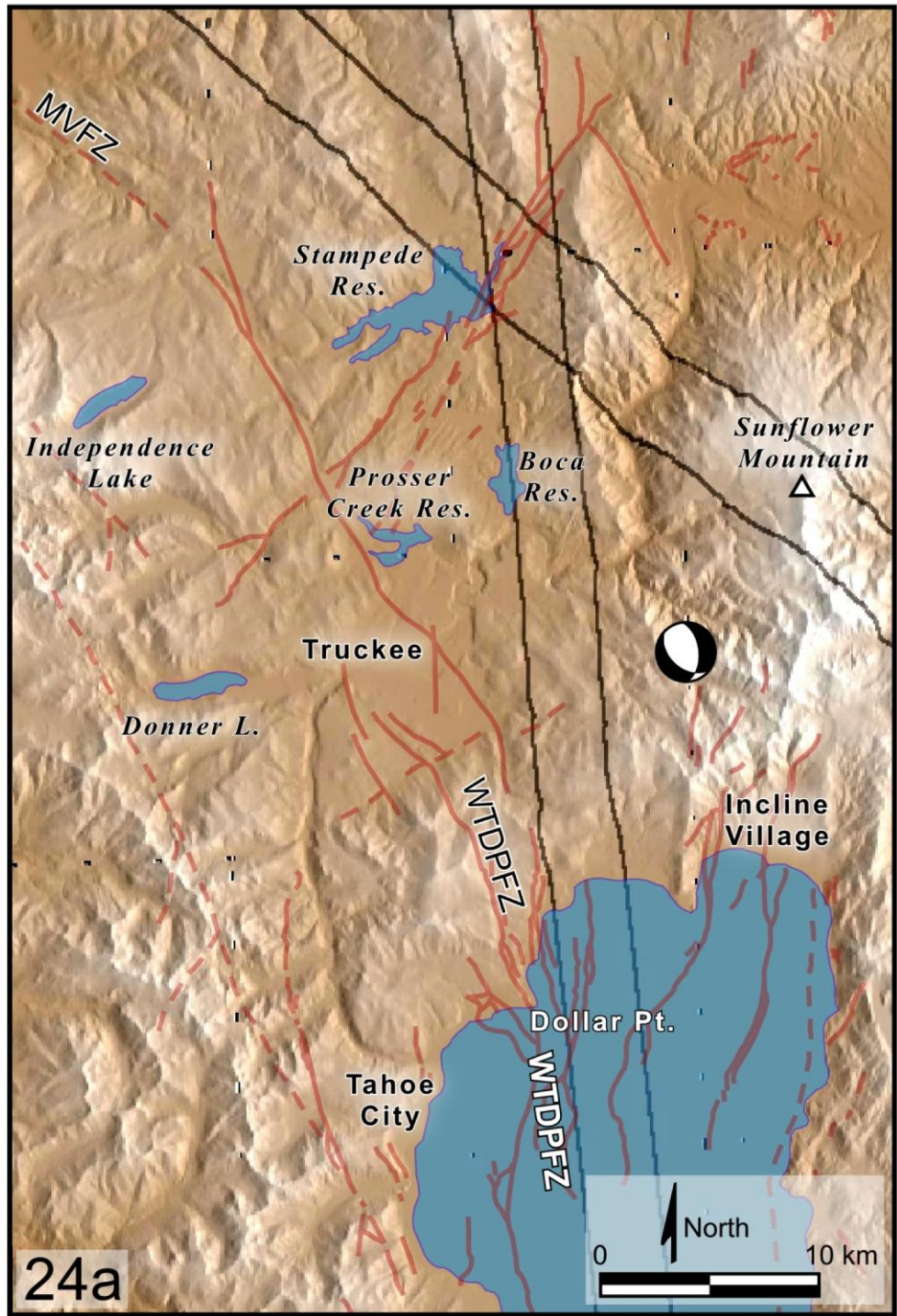


Figure 11. Seismo-lineaments associated with earthquake 24a. Illumination is from the east. WTDPFZ = West Tahoe-Dollar Point fault zone; MVFZ = Mohawk Valley fault zone.

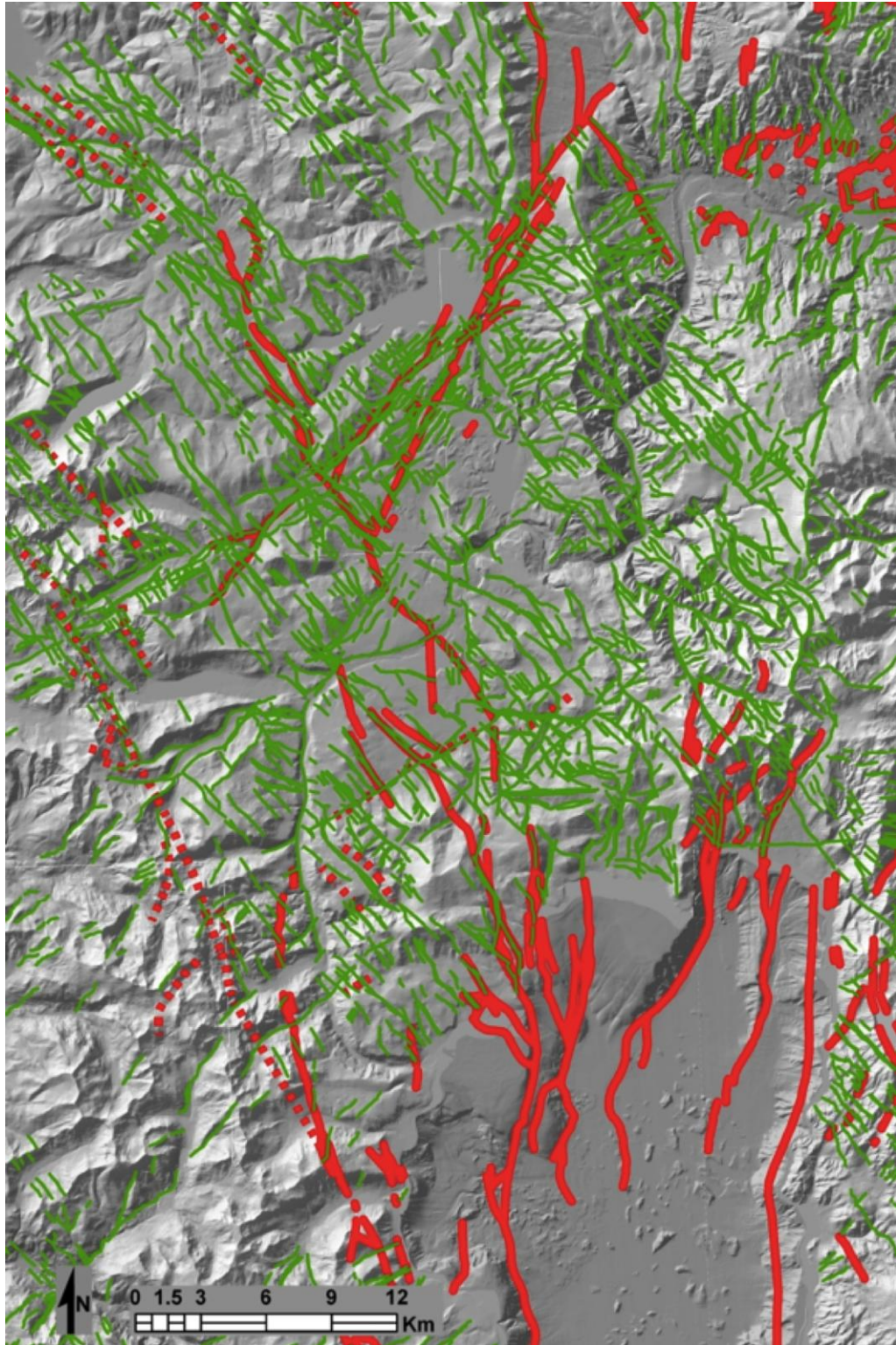


Figure 12. Geomorphic lineaments that might be related to faulting (green curves) and known faults (red) from the Quaternary Fault and Fold Database of the United States (accessed 2011), Saucedo (2005), Hunter and others (2011) and Schweickert and others (2004).

Tahoe fault, the Stateline - North Tahoe fault, the Incline Village fault, Dollar Point fault, the Dog Valley fault, and the Mohawk fault.

Geomorphic lineaments that do not coincide with mapped faults might be due to regional joint trends, lithologic features such as foliation or bedding, glacial or fluvial landforms, or erosional processes unrelated to faulting. Geomorphic lineaments that do not coincide with mapped faults might also be related to previously unrecognized faults. Noteworthy sets of geomorphic lineaments were observed that trend northwest ($\sim 310^\circ$ - 330°) and northeast ($\sim 40^\circ$ - 60°).

Fieldwork

Fieldwork in the Tahoe area is effectively limited to the summer and autumn before the first snowfall. Employment responsibilities limited the field season further, so a plan was developed to examine geomorphic lineaments within seismo-lineaments traversed by accessible paved highways, jeep roads or trails. Rock in the study area is commonly obscured by vegetation, alluvium and soil in stream valleys, and colluvium on hillslopes. Extreme topographic relief made some areas inaccessible. Some geomorphic lineaments were on private land bounded by fences. In most cases, lineaments could not be associated with an observed fault. As a consequence, this study should be considered a preliminary assessment.

Fieldwork to evaluate the possible fault-related origin of geomorphic lineaments was conducted at 30 sites north of Lake Tahoe in September, 2010 (Figure 13; Appendix 4). At the time of the AEG National Meeting at South Lake Tahoe in 2009, Dr. Cronin asked several local geoscientists whether they are aware of any ground-surface exposures of Late Neogene fault surfaces in the Tahoe area. The response was negative, echoing

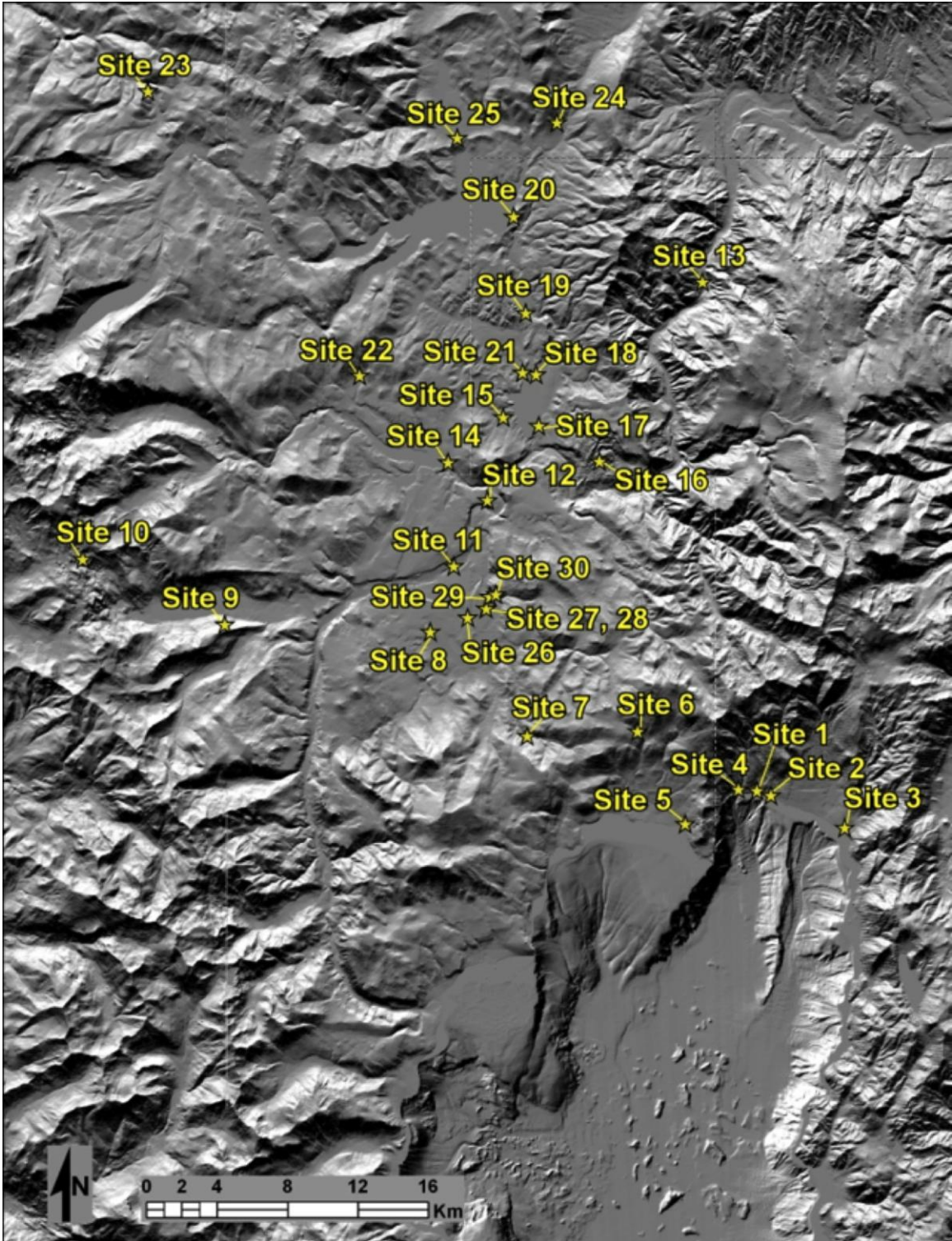


Figure 13. Sites visited to search for ground-surface exposures of faults. Site locations are listed in Appendix 4. Faults were noted at sites 7, 19 and 20.

the comments of Hawkins and others (1986) concerning the lack of surface exposure of the Dog Valley fault. Scarps at the former site of a grammar school in Incline Village (Seitz, 2009) and at the Angora Lakes parking lot, beyond the southern edge of the study area, are clearly associated with recently active faults; however, the fault surfaces in both cases are only accessible via trenching. Although fault exposures were discovered at three sites during fieldwork for this study (sites 7, 19 and 20), availability of fault-surface exposures in the northern Lake Tahoe Basin is limited.

CHAPTER FIVE

Interpretation of Results

Introduction

The goals of this chapter are to summarize the preliminary interpretations of results obtained in this research, and to recognize areas where interpretation is hampered by lack of data that might be collected in future studies. In cases where multiple focal-mechanism solutions are available, an assessment is presented to identify the solution that seems most consistent with the regional structural pattern and the local faults or geomorphology. An interpretation of which nodal plane is most likely to be coincident with the fault plane is made for each earthquake. An assessment of which fault(s) might have generated each earthquake is given, and seismo-lineament trends that do not have mapped faults but that have possible geomorphic indicators of faulting are identified.

The study area features many geomorphic features that are interpreted to have developed as a result of fault displacement; however, the surface trace of most faults mapped in the area is obscured by soil, colluvium, alluvium, vegetation or water. Only three faulted exposures were encountered during the fieldwork for this thesis, and these were assessed for their spatial correspondence with fault-plane solutions. This paucity of fault exposure required a change in the usual interpretive procedure used in SLAM, so emphasis was placed on the correspondence between seismo-lineaments and the traces of mapped faults. Given the recent discovery of the Polaris fault, it is reasonable to suppose that other previously undiscovered faults with late Neogene displacement histories might be present in the north Tahoe area.

It was noted in the previous chapter that there is some temporal clustering of earthquake events. This temporal clustering might indicate either foreshock-mainshock-aftershock events on a single fault, or an earthquake on one fault triggered by the changing stress field after slip on another fault. The epicenters of earthquakes studied in this thesis research also tend to cluster spatially (figure 14). One group (earthquakes 2, 3, 5, 8-10, 13, 25, 26, 29) clusters near the intersection of the Dog Valley fault zone and the Polaris fault. Another group (earthquakes 14, 16-24, 28) clusters in the highland area immediately north of Lake Tahoe, along trend with the West Tahoe-Dollar Point fault zone, the North Tahoe fault, and a new zone defined by NE-SW trending geomorphic lineaments and seismo-lineaments across the area drained by branches of Martis Creek.

Interpretations are potentially affected by two types of uncertainty that are not accounted for in the data used as input to this research. The uncertainty associated with nodal plane orientations was not reported for any focal mechanism solution used in this thesis. In the rare case when uncertainties in the strike and dip (or dip azimuth and dip angle) of nodal planes is reported, the two uncertainties are commonly uncorrelated with each other and are therefore unreliable (Cronin, personal communication, 2011; Cronin, 2008). They are uncorrelated because the reported range of dip angles would not result in the reported range of strike angles. The simplest uncertainty would be described by a conical uncertainty region around the dip vector. The incorporation of an angular uncertainty estimate for the nodal-plane dip vector would be to change the shape of the resulting seismo-lineament on a horizontal plane above the focus from a pair of parallel lines to a pair of curves that are closest up-dip from the focus and diverge with distance along strike away from the focus. It would resemble the outline of a conical hourglass.

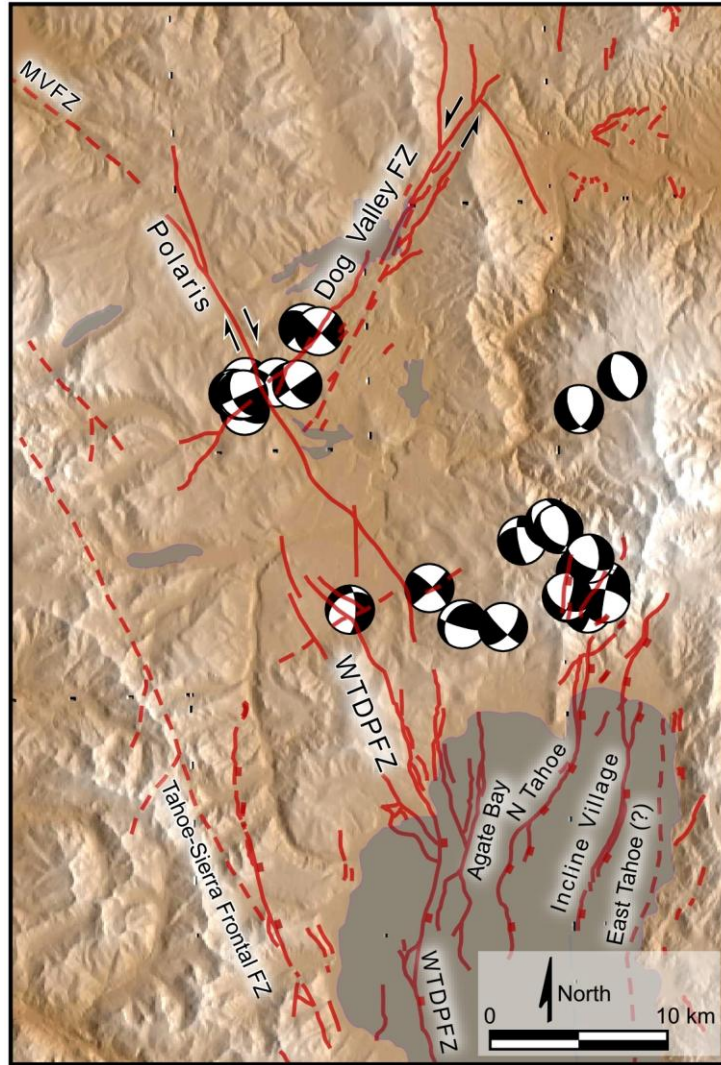


Figure 14. Map of all focal mechanism solutions for which both seismo-lineaments were mapped in the area, and hence could be evaluated. Epicenters spatially cluster near the intersection of the Polaris fault and Dog Valley fault zone, or in the highland area immediately north of Lake Tahoe. WTDPFZ = West Tahoe-Dollar Point fault zone; MVFZ = Mohawk Valley fault zone.

The other uncertainty that potentially affects the interpretation involves the unreported or inconsistent uncertainty in focal location, and in particular, the focal depth. Formal uncertainties in focal location were not reported for six of the focal mechanism solutions listed in table 1 (earthquakes 13a, 13d, 14a, 14b, 24a and 27c), and were arbitrarily set equal to 1 km for both the vertical and horizontal uncertainties in order to

compute the corresponding seismo-lineament location. The focal depths for three of the earthquakes that had multiple focal-mechanism solutions diverged beyond the limits of the reported vertical uncertainties. Various reports of focal depths for earthquake 13, a M 3.6-3.8 event on 15 January 1998, were 5.0 km (USGS), 0.04 ± 0.3 km (NCEDC), and 9 km (Ichinose and others, 2003). For earthquake 14, a M 4.7-5.3 event on 30 October 1998, reported focal depths were 14.2 km (Dreger, accessed 2011) and 11.0 km (Ichinose and others, 2003). For earthquake 27, a M 4.7-5.2 event on 26 June 2005, reported focal depths were 0.09 ± 0.6 km (NCEDC) and 7.10 km (Dreger, accessed 2011). The effect of changing the focal depth for any of our runs would be to shift the resulting seismo-lineament parallel to strike; the effect of increasing the estimated vertical uncertainty would be to widen the seismo-lineament.

The strike of interpreted fault-plane solutions listed in table 4 is chosen using the right-hand rule convention, in which the reference strike is 90° anticlockwise from the trend of the dip vector. Fault types in table 4 are normal and reverse dip-slip faults along which the hanging-wall slip vector is essentially colinear with the dip vector, sinistral (left-lateral) and dextral (right-lateral) strike-slip faults in which the slip vector is essentially horizontal, and oblique faults. Faults are considered oblique if the plunge of the N axis is between 10° and 80° . The first term used to describe an oblique fault indicates the dominant component of slip, if any. For example, a dextral-normal fault has an N axis that plunges $>45^\circ$ and the center of the focal-mechanism diagram is in a white quadrant. A normal-dextral fault has an N axis that plunges less than 45° and a white center to the focal-mechanism diagram. Focal-mechanism solutions that did not yield two full seismo-lineaments in the field area were excluded from table 4.

Table 4. Preliminary interpretations of fault planes and fault correlations

Earthquake Number	Fault Plane		Fault Type	Fault(s) or Trend
	Strike °, RHR	Dip Angle °		
1a	360	70	normal-dextral	--
1b	242	83	reverse-sinistral	Martis Creek trend
2b	207	83	reverse-sinistral	DVFZ (?)
3b	200	71	sinistral-reverse	DVFZ
3c	A	--	--	--
3d	A	--	--	--
5	332	62	normal	TSNFFZ trend (?)
7	25	45-	normal-sinistral	Martis Creek trend
8	210	55	sinistral-normal	DVFZ
8	306	82	dextral-normal	Prosser Creek trend
9	145	60	dextral-normal	Polaris fault (?)
9	55	90	sinistral-normal	DVFZ (?)
10	120	60	reverse-dextral	MVFZ
11a	212	31	reverse-sinistral	Martis Creek trend
11b	A	--	--	--
12	A	--	--	--
13a	57	89	reverse-sinistral	DVFZ
13a	325	30	reverse-dextral	TSNFFZ
13b	241	41	reverse-sinistral	DVFZ
13c	A	--	--	--
13d	223	89	reverse-sinistral	DVFZ
14a	122	89	dextral	Prosser Creek trend
14a	32	88	sinistral	North Tahoe fault
14b	125	85	dextral	Prosser Creek trend
14b	34	79	sinistral	North Tahoe fault
15	135	81	dextral-normal	Polaris fault (?), Prosser Creek trend (?)
15	40	60	sinistral-normal	Martis Creek trend
16	15	75	sinistral-normal	WTDPFZ, Agate Bay fault
16	108	80	dextral-normal	Prosser Creek trend
17	29	64	dextral-normal	North Tahoe fault
18a	A	--	--	--
18b	170	75	normal-sinistral	North Tahoe fault
19	20	75	sinistral-reverse	WTDPFZ, Agate Bay fault, North Tahoe fault
20a	180	80	sinistral-normal	North Tahoe fault
20b	15	81	sinistral-reverse	North Tahoe fault
21	190	85	sinistral-normal	North Tahoe fault, IVFZ
22a	16	76	sinistral-normal	WTDPFZ, Agate Bay fault
23	352	56	normal-sinistral	North Tahoe fault, Agate Bay fault

Table 4. Preliminary interpretations of fault planes and fault correlations—Continued.

Earthquake Number	Fault Plane		Fault Type	Fault(s) or Trend
	Strike °, RHR	Dip Angle °		
24a	354	54	normal-sinistral	WTDPFZ(?), Agate Bay fault
24b	358	54	normal-sinistral	WTDPFZ(?), Agate Bay fault
25	55	75	sinistral-normal	DVFZ(?)
25	150	71	dextral-normal	Polaris fault
26	155	50	dextral-normal	Polaris fault
27a	314	80	dextral-reverse	Polaris fault
27a	45	85	sinistral-reverse	Martis Creek trend
27b	A	--	--	--
27c	321	76	dextral-normal	Polaris fault
27c	230	86	sinistral-normal	Martis Creek trend
28	2	56	normal-sinistral	North Tahoe
29	44	80	sinistral	DVFZ

RHR=right-hand rule, A=ambiguous; DVFZ=Dog Valley fault zone, IVFZ=Incline Village fault zone, MVFZ=Mohawk Valley fault zone, TSNFFZ=Tahoe-Sierra Nevada Frontal fault zone

Some earthquake focal mechanism solutions referenced in table 4 can be spatially correlated with more than one fault. These events are compiled in table 5. It is tempting to infer that earthquakes with similar source mechanisms that are temporally clustered are most likely to be part of displacement sequence on a single fault surface. For example, earthquakes 14-16 might be inferred to have occurred along the Prosser Creek trend that all have in common. Without additional supporting data, this is a weak inference. The M 6.2 earthquake on the Elmore Ranch fault (Salton Trough, southern California) triggered the M 6.6 earthquake on the Superstition Hills fault ~11.3 hours later on 24 November 1987, with epicenters separated by 10 km. The Elmore Ranch and Superstition Hills earthquakes demonstrate that an earthquake on one fault can trigger an earthquake on an adjacent conjugate fault (Hanks and Allen, 1989). The seismo-lineaments for the Superstition Hills earthquake included both the Superstition Hills and Elmore Ranch

faults, and fieldwork was required to identify surface rupture associated with the event (Millard, 2007; Sharp and others, 1989).

Table 5. Earthquakes spatially correlated with more than one fault or trend

Date	Number	Faults or trends
August 30 1992	8	Dog Valley fault zone, Prosser Creek trend
August 6 1993	9	Dog Valley fault zone, Polaris fault
January 15 1998	13	Dog Valley fault zone, Tahoe-Sierra Nevada Frontal fault zone
October 30 1998	14	North Tahoe fault (?), Prosser Creek trend
October 30 1998	15	Polaris fault (?), Prosser Creek trend (?), Martis Creek trend
October 30 1998	16	Prosser Creek trend, West Tahoe-Dollar Point fz, Agate Bay fault
May 29 2001	19	Agate Bay fault, North Tahoe fault, West Tahoe-Dollar Point fz
July 7 2001	21	Incline Village fault zone, North Tahoe fault
October 30 2001	22	Agate Bay fault, West Tahoe-Dollar Point fault zone
June 3 2004	23	Agate Bay fault, North Tahoe fault
June 3 2004	24	Agate Bay fault, West Tahoe-Dollar Point fault zone (?)
June 12 2004	25	Polaris fault, Dog Valley fault zone (?)
June 26 2005	27	Martis Creek trend, Polaris fault

(?) indicates spatial correlation with the fault is weak or tenuous

Faults and Seismo-Lineament Trends

Polaris Fault

Seismo-lineaments associated with earthquakes 9, 25, 26 and 27c spatially correlate with the Polaris fault (figure 15) and geomorphic lineaments trending parallel to it. One of the seismo-lineaments associated with earthquake 15 is similar to the trend of the Polaris fault. These are all oblique-slip mechanisms on planes dipping between 50° and 80°, with dextral strike-slip and either normal or reverse dip-slip (table 4). The Polaris fault is currently understood to be a dextral fault with some local down-to-the-east normal slip (Hunter and others, 2011; Olig and others, 2005a; Melody, 2009). The focal

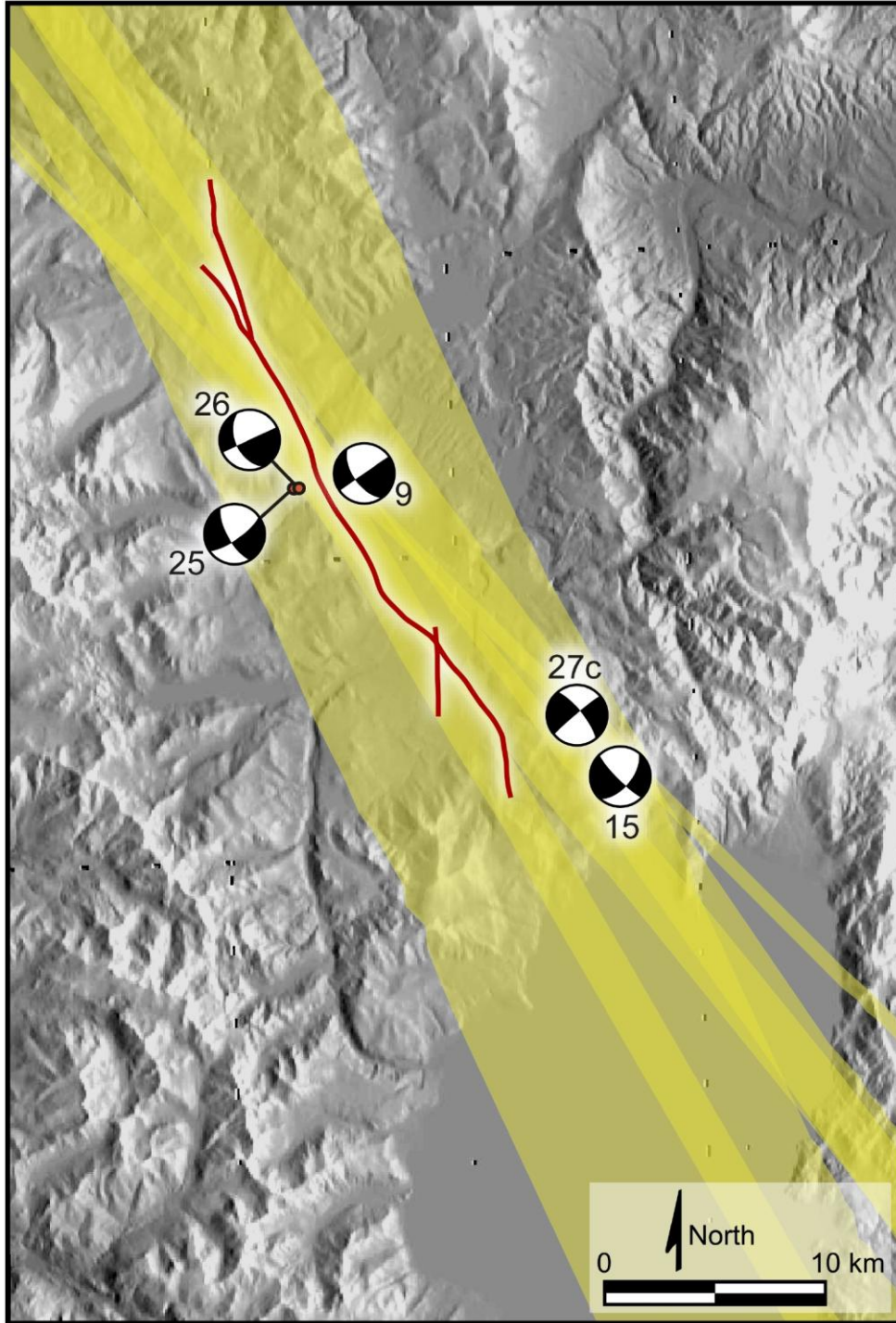


Figure 15. Overlapping seismo-lineaments (yellow) from focal mechanisms of earthquakes 9, 15, 25, 26 and 27c. Surface trace of the dextral Polaris fault is the red dashed curve. Earthquake numbers in this and all similar figures that follow are from table 1.

mechanisms to earthquakes 9, 15, 25, 26 and 27 are consistent with the observed slip characteristics of the Polaris fault.

Several of the earthquakes in this set spatially correlate with more than one fault. Rather than being associated with the Polaris fault, earthquake 9 might have occurred on the Dog Valley fault zone, earthquake 15 on the Prosser Creek or Martis Creek trends, earthquake 25 on the Dog Valley fault zone, and earthquake 27 on the Martis Creek trend.

Earthquakes 25 and 26 occurred within 15 minutes of each other on 12 June 2004. Earthquakes 23 and 24 are interpreted to have occurred on the West Tahoe-Dollar Point fault zone of the North Tahoe fault just 9 days earlier, so it is possible that the earlier earthquakes helped trigger the 12 June earthquakes on the Polaris fault. One year later on 26 June 2005, earthquake 27 occurred at the southern end of the Polaris fault ~5 km southwest of the epicenters of events 23 and 24.

The Polaris fault was identified based on geomorphic analysis of bare-earth LiDAR imagery (Hunter and others, 2011). Using the coarse resolution of a 10 m DEM, geomorphic features suggestive of faulting such as aligned drainages, vertical steps in ridges, benches, scarps, pressure ridges, and stream channel lateral deflections (figure 16) were observed in each seismo-lineament on the DEM surface. One exposed fault surface was found within the general trend of the Polaris fault at site 7 during fieldwork (figure 17; appendix 4). The fault observed at site 7 has a dip vector that is within 30° of the dip vector of a nodal plane of focal mechanism 27c (appendix 5); however, the observed fault is a reverse fault, while 27c is a normal-oblique focal mechanism. The fault

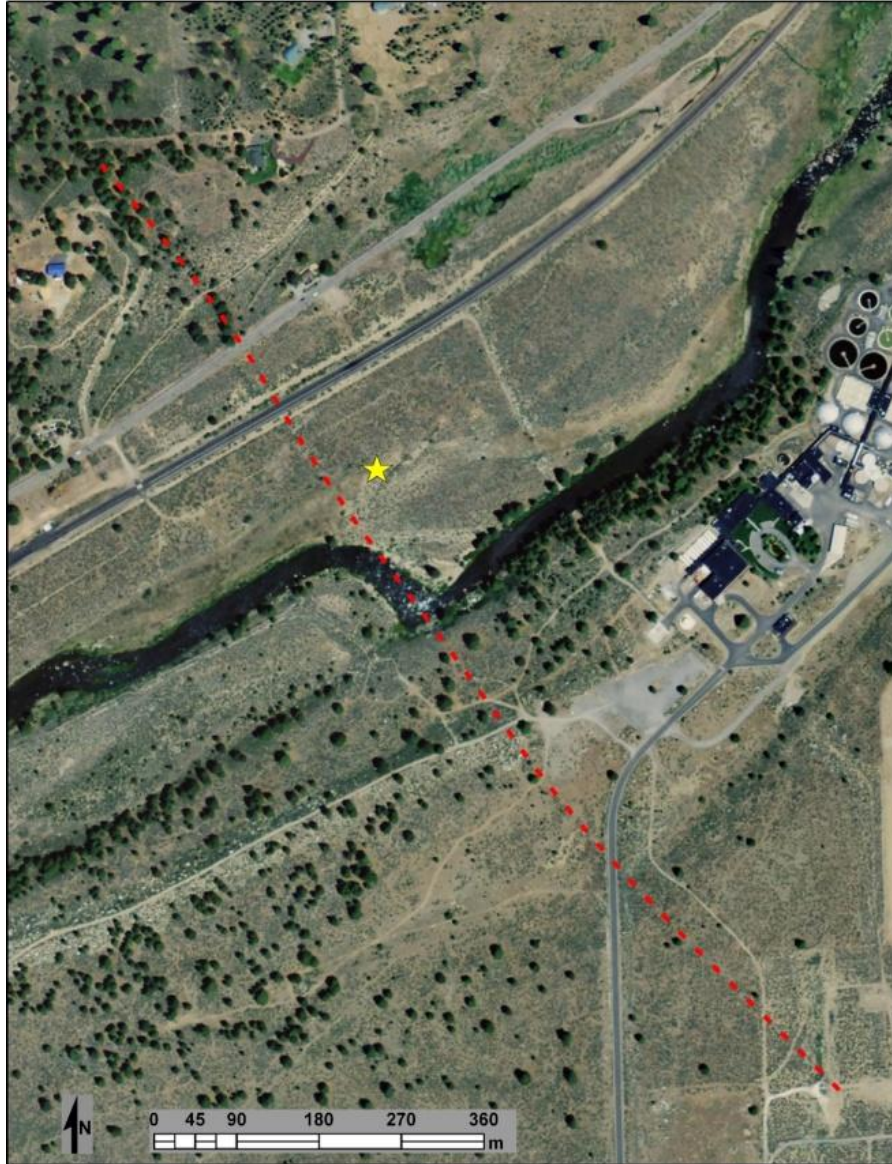


Figure 16. Geomorphic indicators of faulting associated with the dextral Polaris fault (dashed red curve). Location of part of the Truckee River channel is controlled by the Polaris fault, circa 39.34°N 120.13°W. Truckee sanitation plant is on the right.

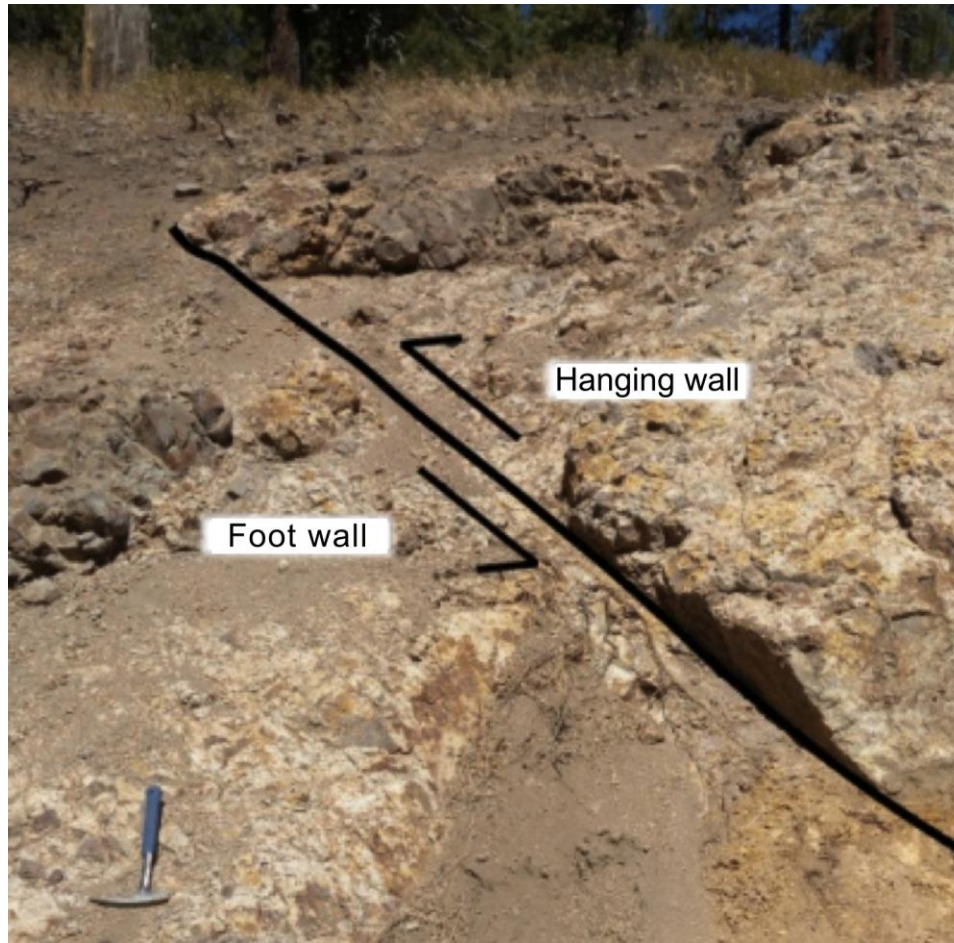


Figure 17. Reverse fault observed at site 7. Fault orientation is $346^{\circ} 56^{\circ}\text{E}$. Rock hammer is for scale.

observed at site 7 does not correlate with any of the earthquakes in table 1, or with faults on the published geologic maps reviewed for this study.

The Polaris fault is interpreted to be a seismogenic fault. Recent trench studies across the Polaris fault indicate a Holocene displacement history (Hunter and others, 2011; Melody, 2009). Based on this preliminary SLAM analysis, $M \geq 3$ earthquakes in 1993, 2004 and 2005 are spatially correlated with the Polaris fault, and an event in 1998 is weakly correlated with that fault.

Dog Valley Fault Zone

Seismo-lineaments associated with earthquakes 3, 8, 9, 13, 25 and 29 spatially correlate with the Dog Valley fault zone (DVFZ, figure 18) and geomorphic lineaments trending parallel to it (figure 19). One of the seismo-lineaments associated with earthquake 2 is similar to the trend of the DVFZ, and events 2 and 3 occurred within 2.25 hours of each other on 3 July 1983. These are all oblique-slip mechanisms on planes dipping between 41° and 90° , with sinistral strike-slip and either normal or reverse dip-slip (table 3). The DVFZ is currently understood to be a sinistral fault system with some local dip slip (Kachadoorian and others, 1967; Greensfelder, 1968; Ryall and others, 1968; Tsai and Aki, 1970; VanWormer and Priestly, 1978; Ryall and VanWormer, 1980; Hawkins and others, 1986). The focal mechanisms to earthquakes 2, 3, 8, 9, 13, 25 and 29 are consistent with the observed slip characteristics of the Dog Valley fault zone.

Several of the earthquakes in this set spatially correlate with more than one fault. Rather than being associated with the Dog Valley fault zone, earthquake 8 might have occurred on the Prosser Creek trend, earthquake 9 on the Polaris fault, earthquake 13 on the TSNFFZ, and earthquake 25 on the Polaris fault.

Some of the dominant geomorphic features observed on the surface of the DEM were aligned drainages and ridges (figure 19). Most geomorphic lineaments in the region trend in the approximately in same direction as the ground rupture from the 1966 M 6.0 Truckee earthquake (Kachadoorian and others, 1967). Two fault surfaces were found

within the seismo-lineaments at sites 19 and 20. No shear striae were observed at site 19, which displayed a reverse sense of stratigraphic separation on the outcrop surface (figure 20). The fault at site 19 is a previously unmapped fault that is on trend with one of the surface ruptures of the 1966 M 6.0 Truckee earthquake (Kachadoorian and others, 1967). The fault at site 20 was inaccessible and no measurements were obtained, although a normal sense of stratigraphic separation was observed on the outcrop surface (figure 21). The dip vector of the fault at site 19 trends $108^{\circ} \pm 18^{\circ}$ plunging $82^{\circ} \pm 2^{\circ}$ -- $\sim 10^{\circ}$ from the dip vector for nodal planes 9-A, 13a-A and 25-A, and $\sim 30^{\circ}$ from the dip vector for nodal plane 13b-A (figure 22; appendix 5). However, site 19 is located just outside seismo-lineaments 13a-A and 25-A.

The Dog Valley fault zone is interpreted to be seismogenic. Based on this preliminary SLAM analysis and previous work (*e.g.*, Hawkins and others, 1986), $M \geq 3$ earthquakes in 1966, 1983, 1992, 1993, 1998 and 2004 are tentatively correlated with the Dog Valley fault zone.

Sierra-Tahoe Frontal Fault Zone

Seismo-lineaments associated with earthquake focal mechanisms 5 and 13b are located between and subparallel to the Tahoe-Sierra Nevada Frontal fault zone (TSNFFZ) and the Dollar Point fault zone (DPFZ; figure 23). The spatial correlation with these faults is weak because the mapped fault traces are not within the seismo-lineaments. There are distinctive geomorphic lineaments within the seismo-lineaments between the TSNFFZ and DPFZ. These geomorphic lineaments are not mapped as faults yet have features which are indicative of faulting, such as abrupt changes in gradients of ridge

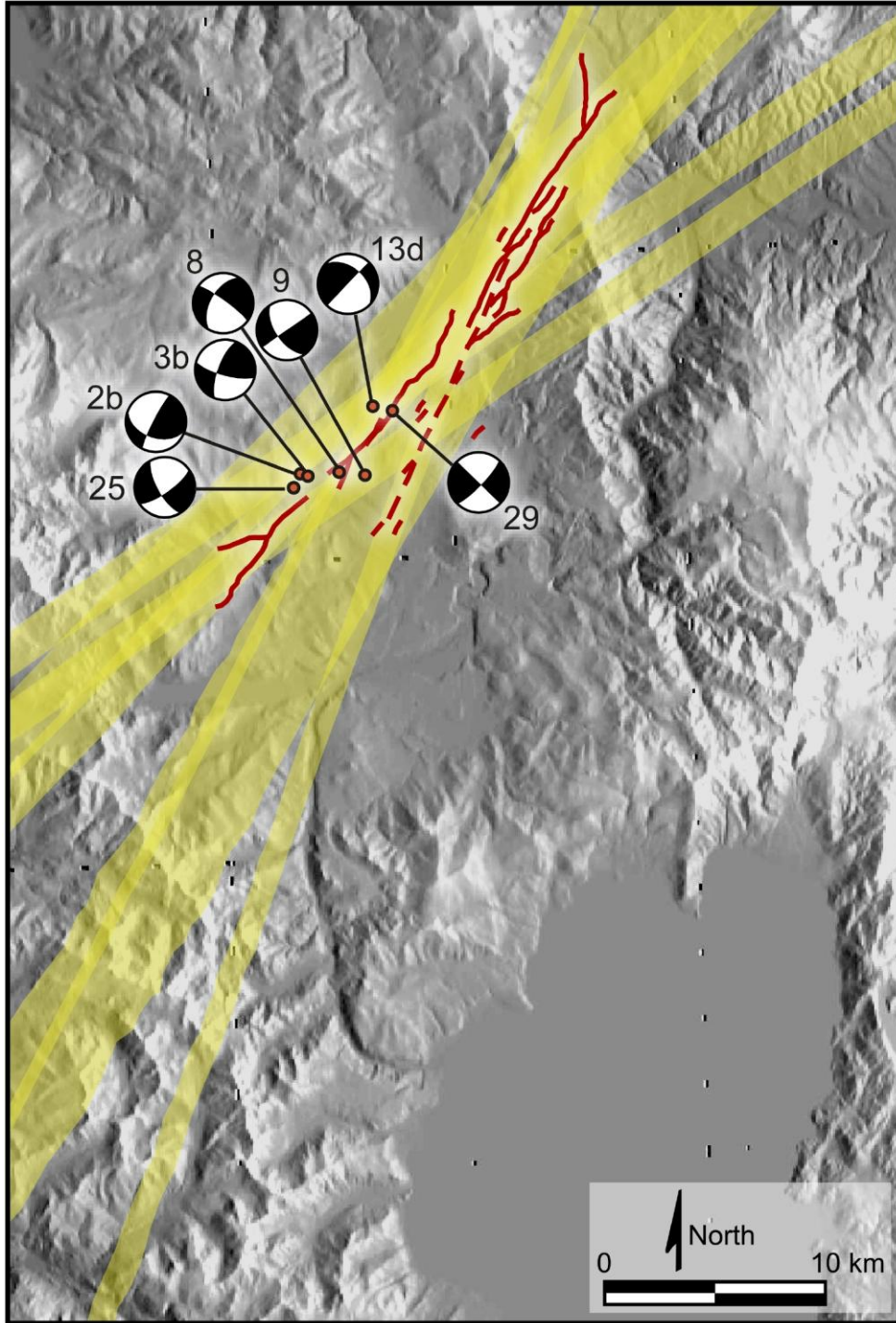


Figure 18. Overlapping seismo-lineaments (yellow) from focal mechanisms of earthquakes 2, 3, 8, 9, 13, 25 and 29. Surface trace of segments of the sinistral Dog Valley fault zone are indicated by the red dashed curves.

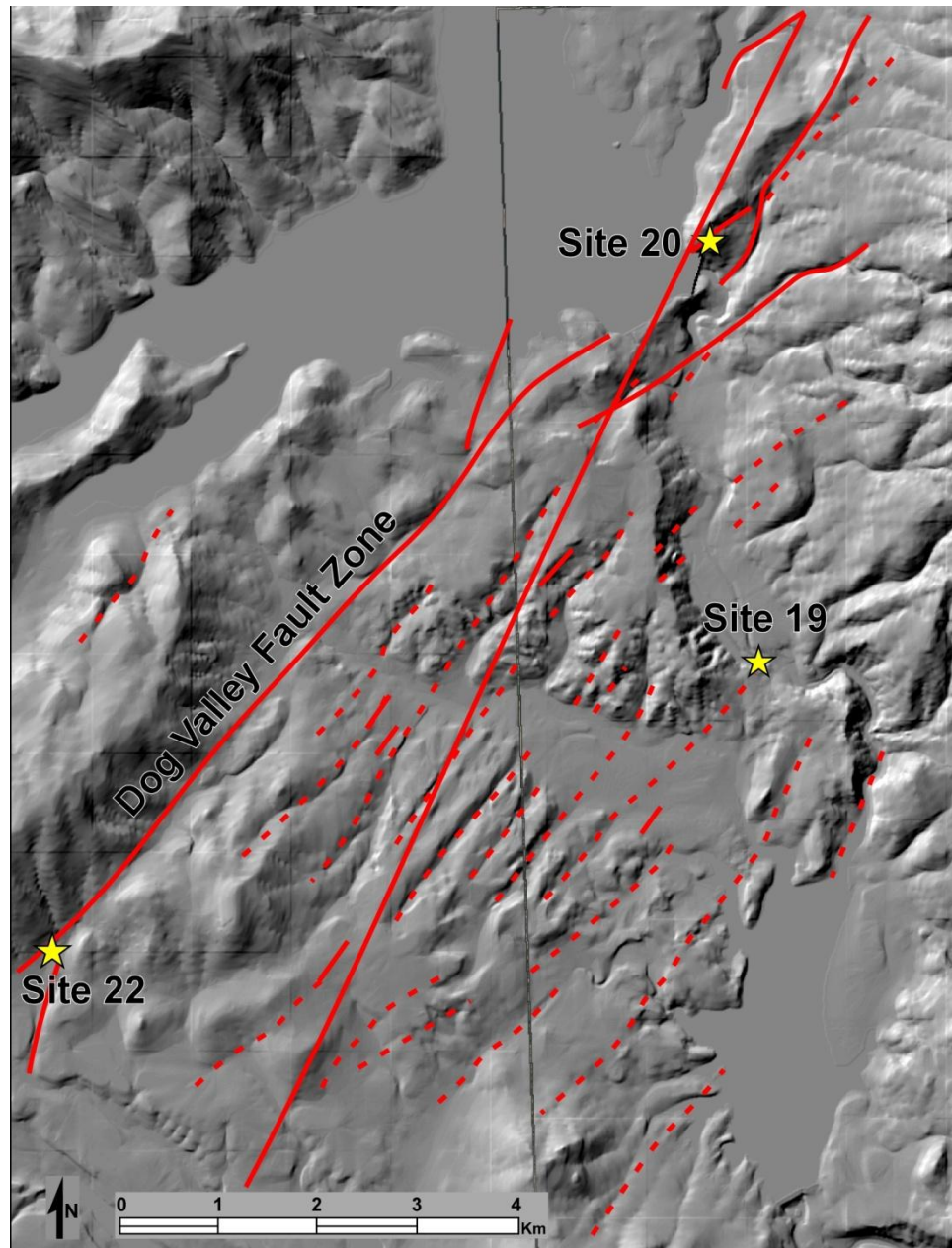


Figure 19. Geomorphic lineaments (red dashed curves) and mapped traces of faults (red solid curves) in the Dog Valley fault zone. Fault exposures were observed at sites 19 and 20. Stampede Reservoir is the featureless area toward the top left of the map, and Boca Reservoir is at the bottom right.



Figure 20. Oblique fault exposure at site 19. Fault orientation (strike and dip) is $17^{\circ}\pm 18^{\circ}$ $82^{\circ}\pm 2^{\circ}$ SE.



Figure 21. Fault exposure at site 20. Dan Lancaster provides the scale.

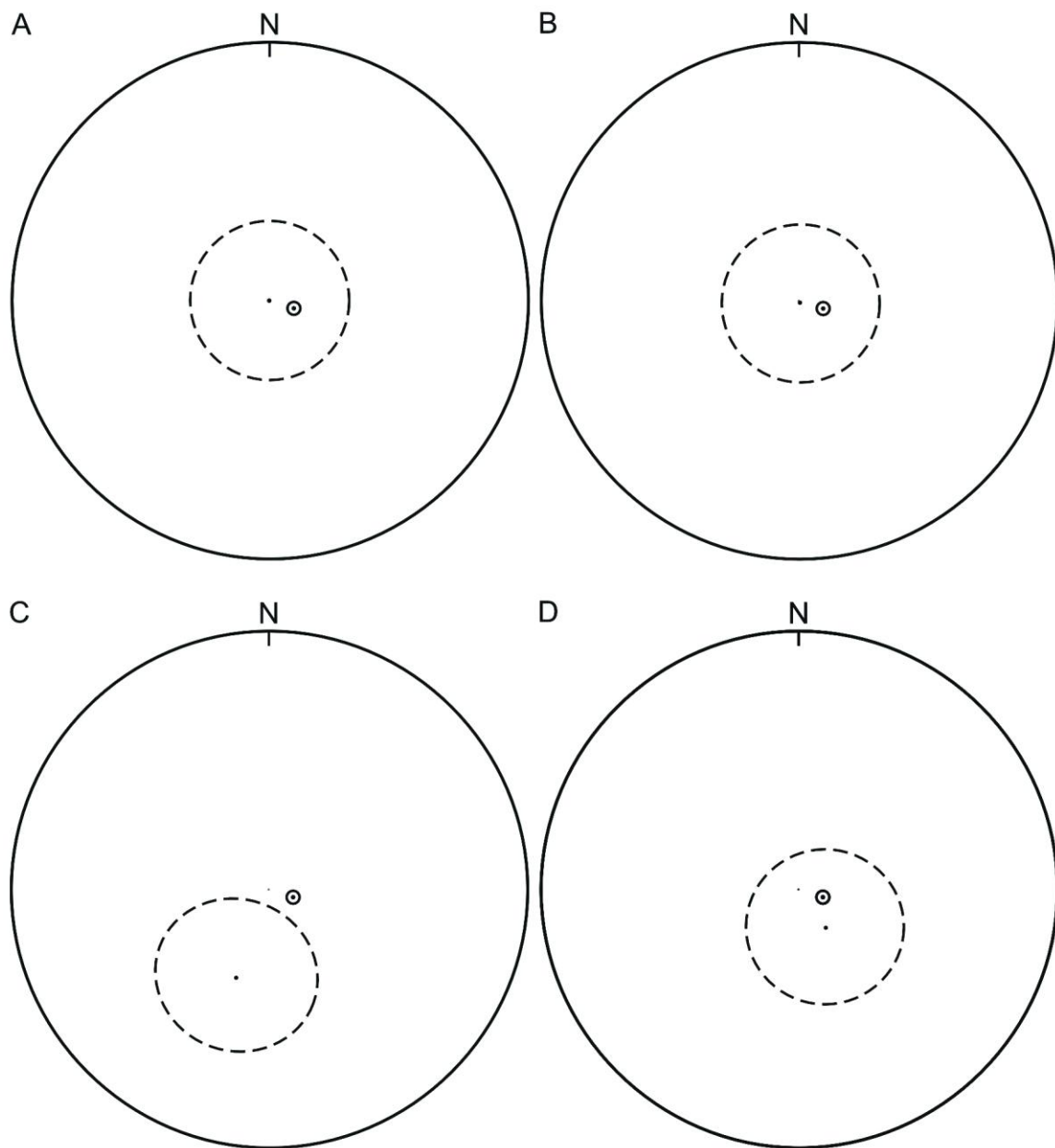


Figure 22. Lower-hemisphere equal-area projections of the dip vector for the fault exposed at site 19 (solid small circle), shown relative to the dip vectors of nodal planes from four earthquake focal mechanism solutions: [A] earthquake 9; [B] earthquake 13a; [C] earthquake 13b; and [D] earthquake 25. Dashed small-circles around the nodal-plane dip vectors have an angular radius of 25° .

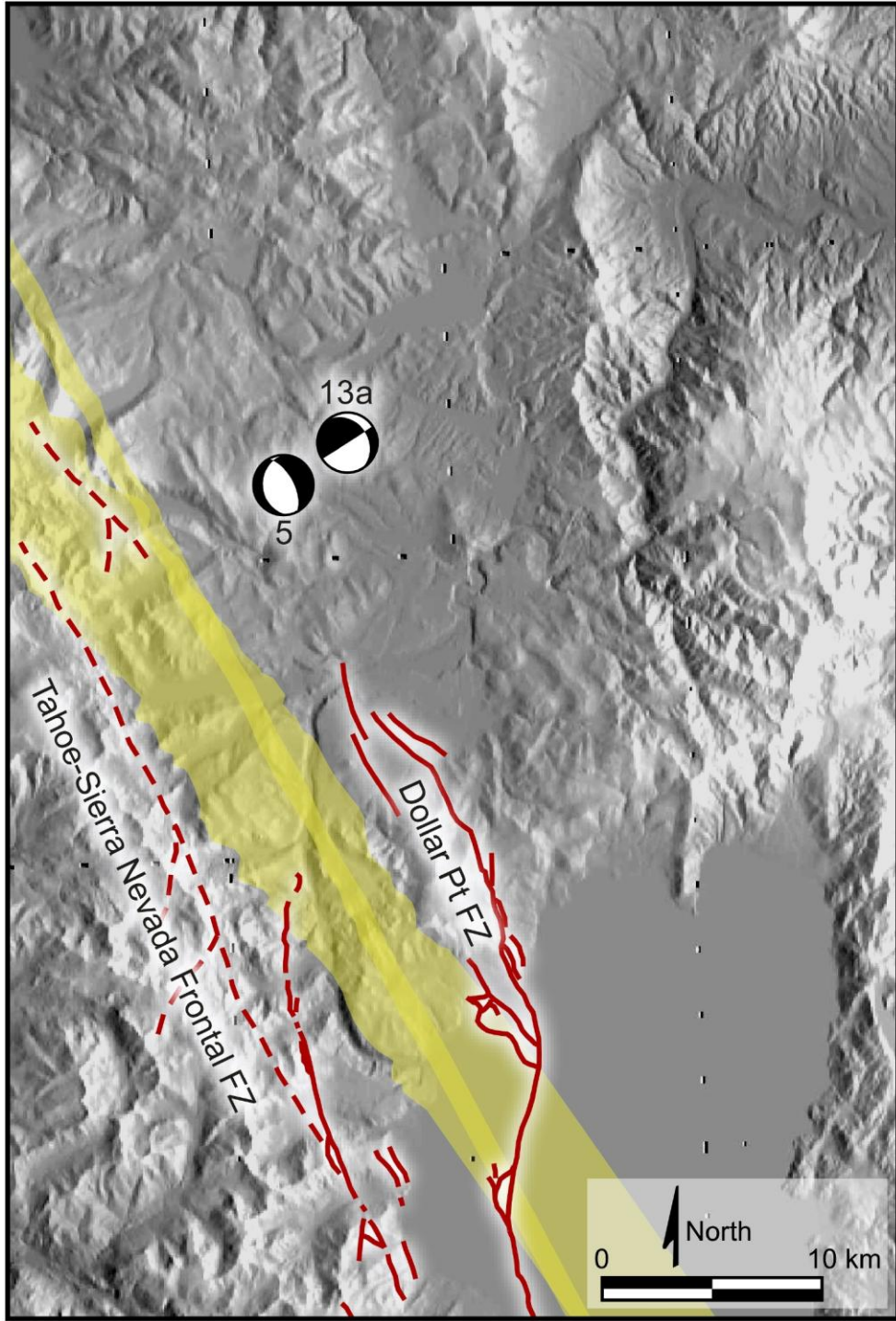


Figure 23. Overlapping seismo-lineaments (yellow) from focal mechanisms of earthquakes 5 and 13a. Surface trace of the Dollar Point fault zone and the Sierra Nevada Frontal fault zone are the red dashed curves.

crests, aligned drainages, and abrupt changes in topography. Surface exposures of faults were not found in the field along this trend.

West Tahoe – Dollar Point Fault Zone and Agate Bay Fault

Seismo-lineaments associated with five earthquakes in table 1 correlate with strands of the West Tahoe-Dollar Point fault zone (WTDPFZ) or the Agate Bay fault (figure 24). The Agate Bay fault is mapped based on geomorphic features on the floor of Lake Tahoe (Gardner and others, 1998, 2000; Saucedo, 2005; Sylvester and others, 2007), but was not observed in chirp profiles by Dingler and others (2009), so its existence is in question. Earthquakes 23 (M 3.04) and 24 (M4.2-4.5) occurred 29 minutes apart on 3 June 2004, so they might be interpreted as a foreshock-mainshock sequence on the same fault. Nodal planes 23-B and 24a-A correspond to normal faults with small sinistral components that dip east 54° - 56° , striking 352° - 354° . Earthquakes 19 and 22 occurred five months apart in May-October 2001, interpreted to be on east-dipping sinistral-oblique faults striking 16° - 20° . Similarly, earthquake 16 might have occurred on a sinistral-normal fault striking 15° and dipping 75° E, although its other nodal plane coincides with the Prosser Creek trend.

Prosser Creek Trend

Seismo-lineaments associated with earthquakes 8 and 14-16 that coincide with a prominent set of geomorphic lineaments form the basis for the Prosser Creek trend (figures 25 and 26). No faults are mapped along this trend on the published geologic

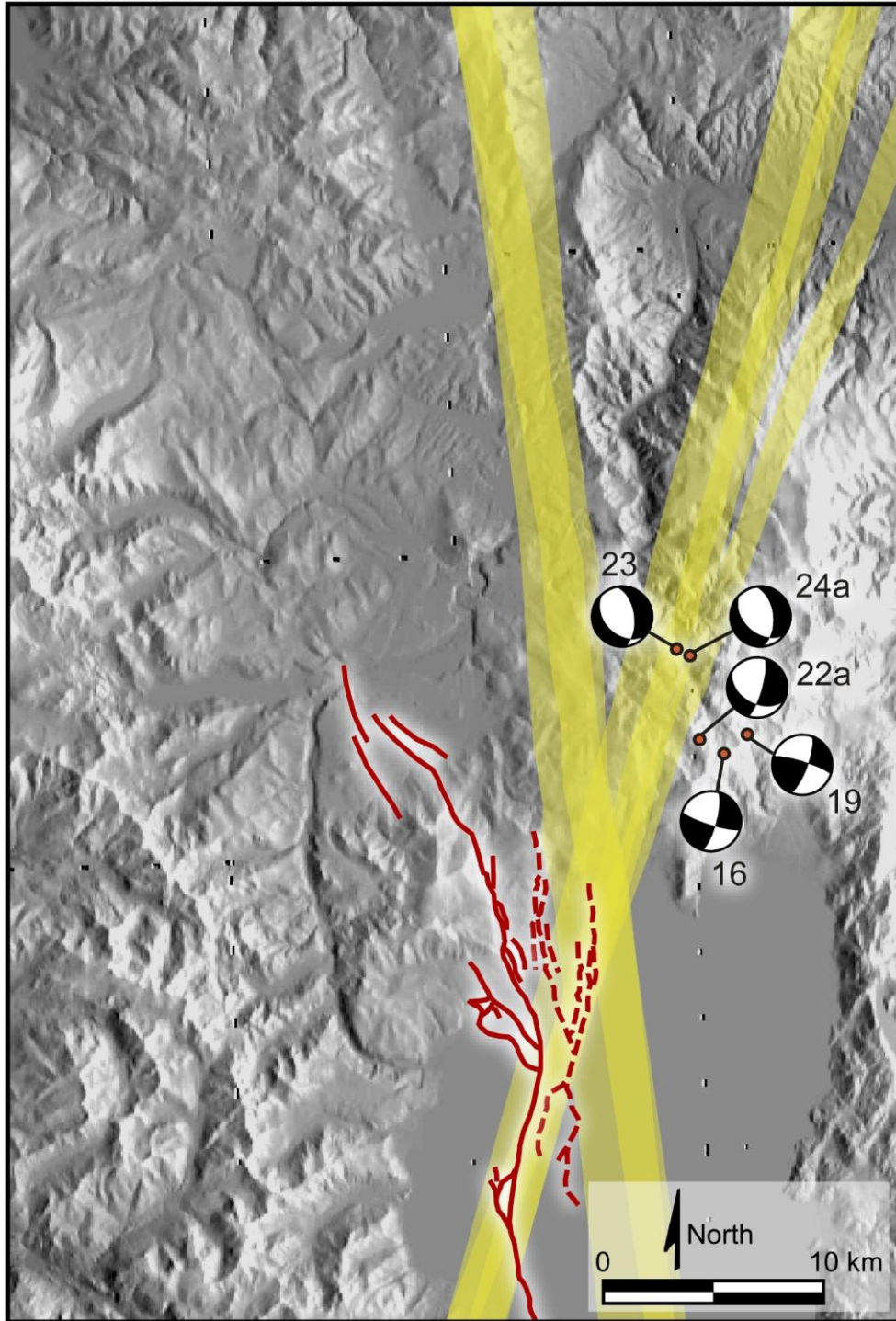


Figure 24. Overlapping seismo-lineaments (yellow) from focal mechanisms of earthquakes 16, 19, 22, 23 and 24. Red curves are surface traces of segments of the West Tahoe-Dollar Point fault zone (solid curves) and Agate Bay fault (dashed curves).

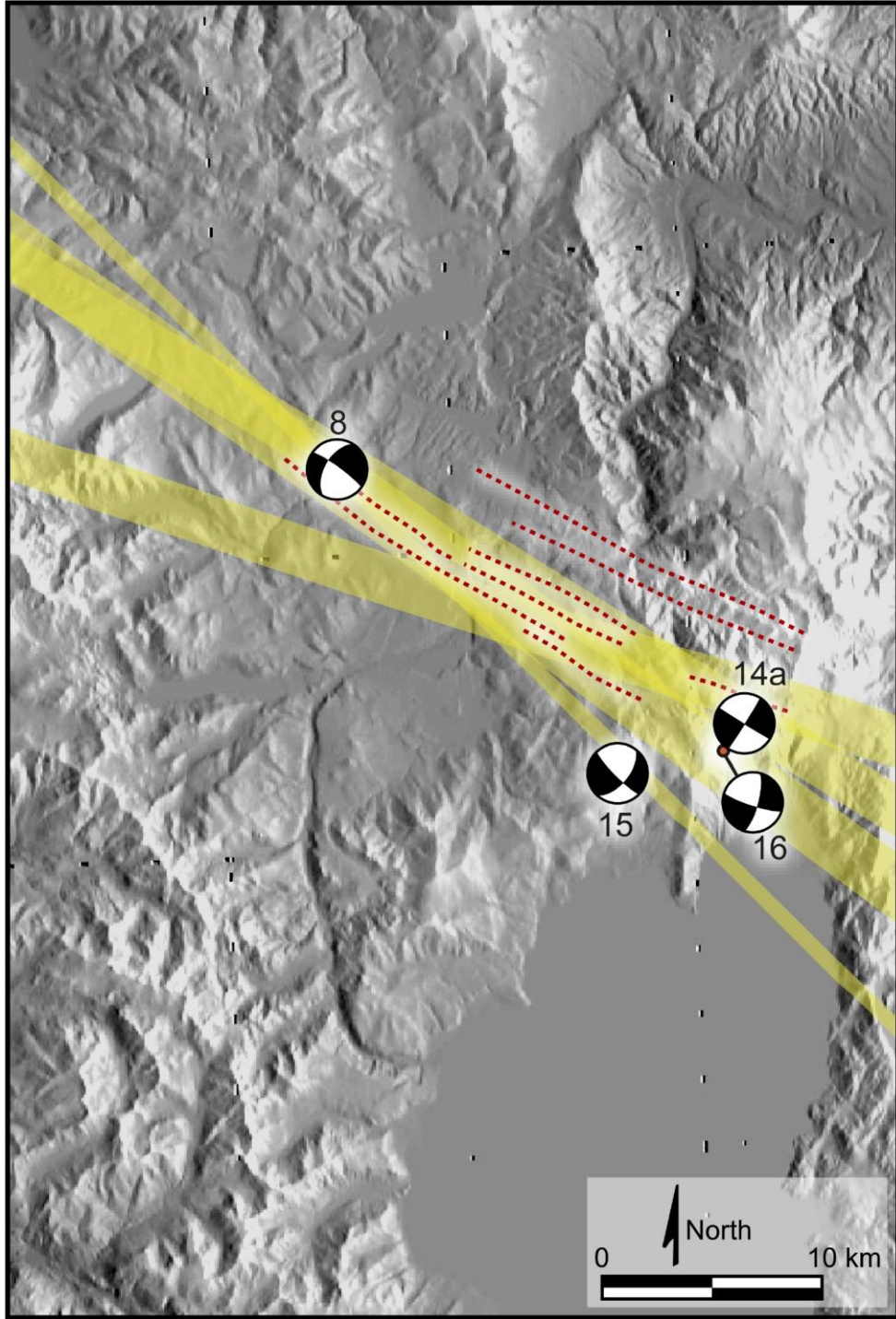


Figure 25. Prosser Creek trend defined by overlapping seismo-lineaments (yellow) from focal mechanisms of earthquakes 8, 14, 15 and 16. These define a zone that includes geomorphic features that are interpreted to be related to faulting (red dashed curves).

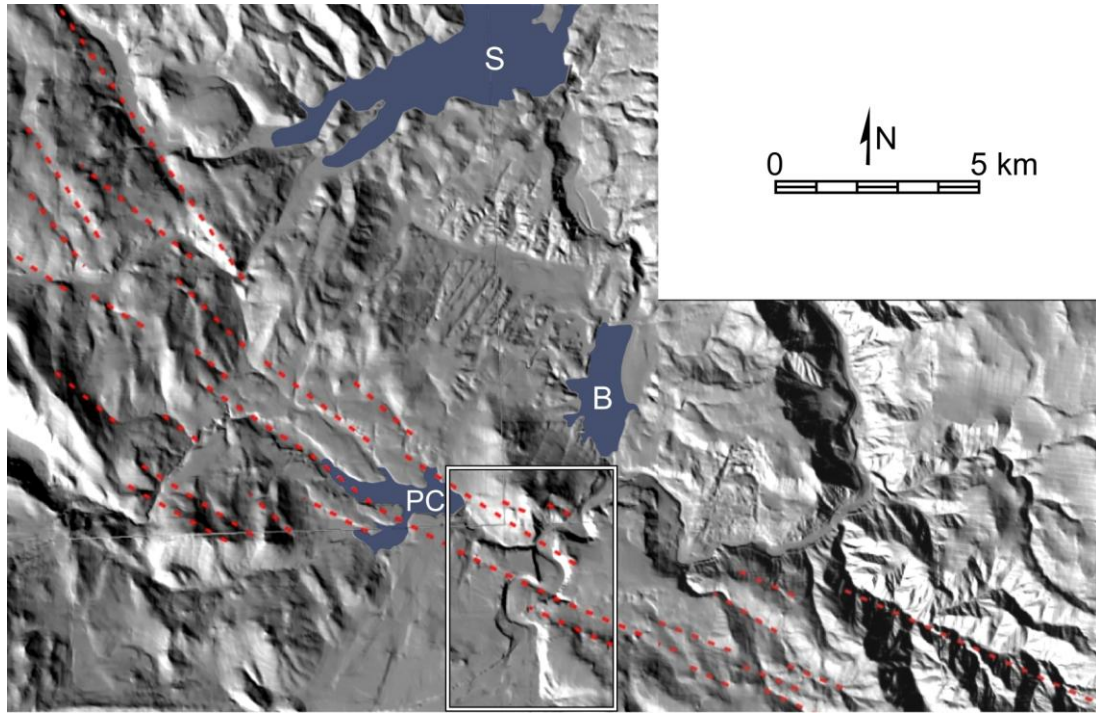


Figure 26. Prosser Creek trend. Red dashed curves are geomorphic lineaments that might indicate faulting and that are coincident with the seismo-lineament trend in Figure 25. Upper map is hillshade image of area near Stampede Reservoir (S), Boca Reservoir (B), and Prosser Creek reservoir (PC). White rectangle is location of aerial photo from Google Earth below, showing interpreted fault-controlled part of Truckee River channel. Road along Truckee River is Interstate Highway 80.

maps reviewed for this thesis. The nodal planes for earthquakes 8 and 14-16 that correspond to this trend are all steeply dipping dextral faults striking NW-SE (table 1). A particularly interesting geomorphic lineament includes part of the channel of the Truckee River (figure 26) and continues away from the river in both directions, marked by linear tonal boundaries, linear topographic features, and vegetation lineations. Several distinct geomorphic lineaments are observed within the boundaries of the composite seismo-lineament, such as right-lateral stream deflections, linear drainages, linear ridges, and linear troughs. These composite geomorphic lineaments continue for approximately thirty kilometers.

Earthquakes 14 (M 4.7-5.3), 15 (M 4.8) and 16 (M 3.05) occurred within 18 minutes of each other on 30 October 1998, with epicenters within ~5 km of each other and reported depths ranging from 2.41 km (#15) to 14.2 km (#14). All three of these earthquakes, as well as earthquake 8, have nodal planes whose seismo-lineaments might be associated with fault trends other than the Prosser Creek trend. Earthquakes 14 and 16 might be related to slip on the North Tahoe or West Tahoe-Dollar Point-Agate Bay fault systems. Earthquake 15 might be related to the Martis Creek trend, and earthquake 8 might be related to the Dog Valley fault zone.

Ichinose and others (1999) attribute the main earthquake to “a N33°E striking high-angle strike-slip fault” dipping 70°SE and locate it “well within the footwall of [the North Tahoe-Incline Village fault zone].” Ichinose and others (2003) published a modified focal mechanism solution for this event, used as earthquake 14b in this study (table 1), with a nodal plane that has the same strike but a steeper dip of 79°E. They map aftershocks along a trend to the northeast, similar to the fault-plane solution they derived

from a directivity analysis; however, the directivity analysis utilizes an aftershock assumed to be coplanar with the mainshock, so the directivity analysis is not an independent assessment of which nodal plane for the mainshock is the fault plane (Ichinose and others, 1999). “Aftershocks” can include induced seismicity on a fault surface that is conjugate to the fault that produced the mainshock, as in the Elmore Ranch-Superstition Hills sequence (Hanks and Allen, 1989).

In summary, there are strong geomorphic indicators of faulting along the Prosser Creek trend. A dextral fault along the Prosser Creek trend would be conjugate to the sinistral Dog Valley fault zone, to some sinistral segments of the North Tahoe or West Tahoe-Dollar Point-Agate Bay fault systems, and to the Martis Creek trend. The seismicity of the Prosser Creek trend is an admissible hypothesis, but is not demonstrated.

North Tahoe Fault

Seismo-lineaments associated with earthquakes 14a, 17-21, 23 and 28 correlate spatially with the northernmost section of the North Tahoe fault (figure 27). The northernmost section of the North Tahoe fault is described as having normal displacement (Schweickert and others, 2004). Potential fault-plane solutions with a north-northwest strike tend to be associated with normal to normal-sinistral slip. The solutions that strike more to the northeast are progressively more sinistral. Geomorphic lineaments potentially related to faulting within or paralleling the seismo-lineaments were not observed on the DEM surface.

Many of the earthquakes that might be correlated with the North Tahoe fault are also spatially correlative with another fault. Earthquake 14 correlates with the conjugate

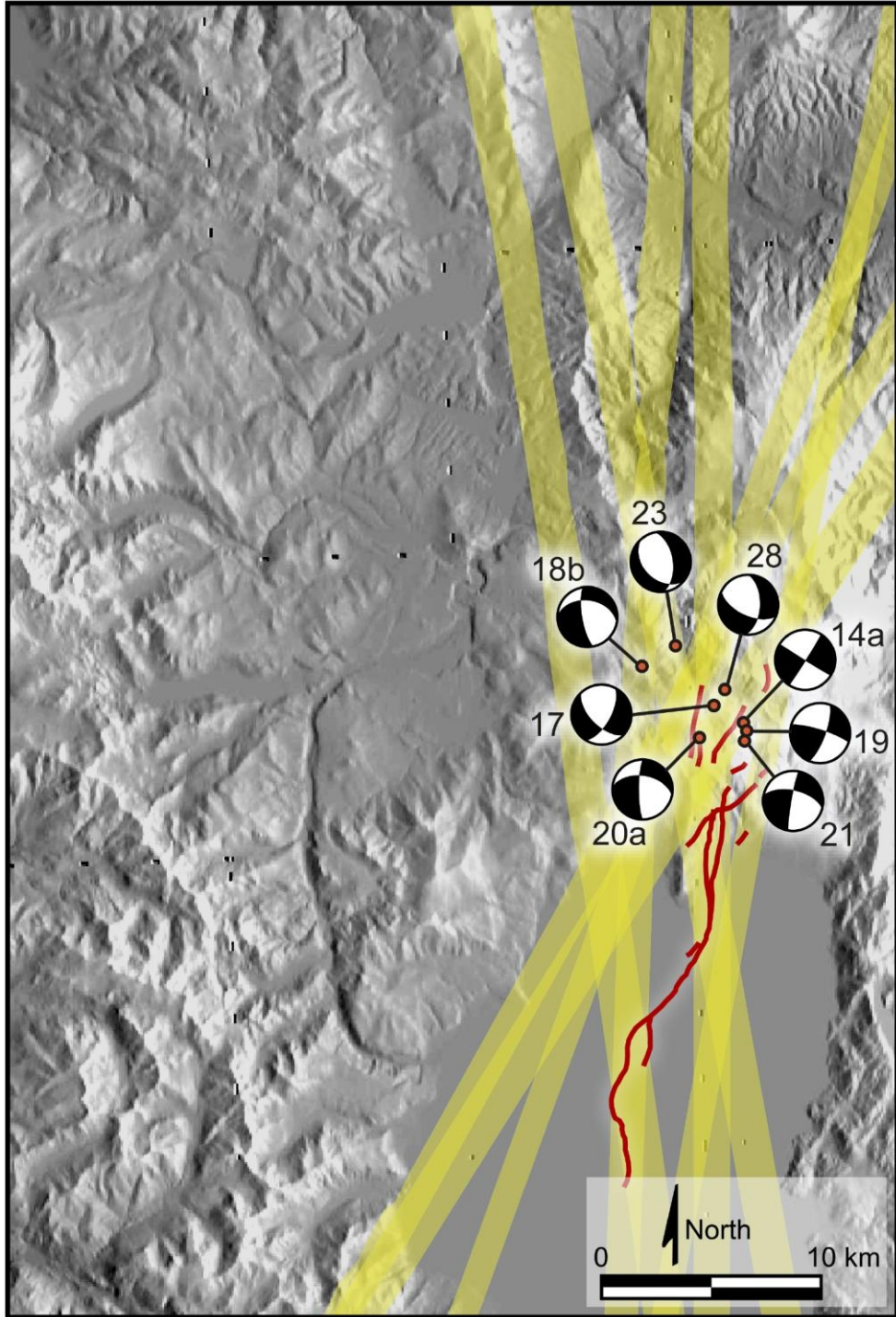


Figure 27. Overlapping seismo-lineaments (yellow) from focal mechanisms of earthquakes 14, 17-21, 23 and 28. Red curves are the surface trace of segments of the North Tahoe fault.

Prosser Creek trend, earthquake 19 with the West Tahoe-Dollar Point-Agate Bay fault system, earthquake 21 with the Incline Village fault zone, and earthquake 23 with the West Tahoe-Dollar Point-Agate Bay fault system. Several of these earthquakes are temporally associated with one another. Earthquakes 14 and 17 occurred within 35 days of each other in October-December, 1988. Both might have occurred on the North Tahoe fault, or earthquake 14 on the Prosser Creek trend might have helped induce earthquake 17 on the North Tahoe fault. Earthquakes 19-21 occurred within 39 days of each other in May-July, 2001, most likely on one or more north- to northeast-striking sinistral-oblique fault(s) in the north-central part of the Lake Tahoe Basin: West Tahoe/Agate Bay fault, North Tahoe fault, or Incline Village fault zone.

Martis Creek Trend

Seismo-lineaments associated with earthquakes 1, 7, 11 and 27 correlate spatially with distinctive northwest-trending geomorphic lineaments that traverse the highland area drained by branches of Martis Creek, just northwest of the Lake Tahoe basin (figures 28 and 29). Earthquake 27 might have originated on the dextral Polaris fault, which would be conjugate to a sinistral fault along the Martis Creek trend. There are no mapped faults that strike parallel to the corresponding nodal planes within the seismo-lineaments along the Martis Creek trend, and no fault surfaces were found in the field. Several of the geomorphic lineaments along the Martis Creek trend are strongly expressed and appear to be continuous for more than 10 km as perceived using the 10-meter DEM. These geomorphic lineaments might have developed along a set of sinistral-oblique cross faults within a part of the northern Walker Lane that is dominated by dextral shear on northwest-striking faults and normal displacement on north-striking

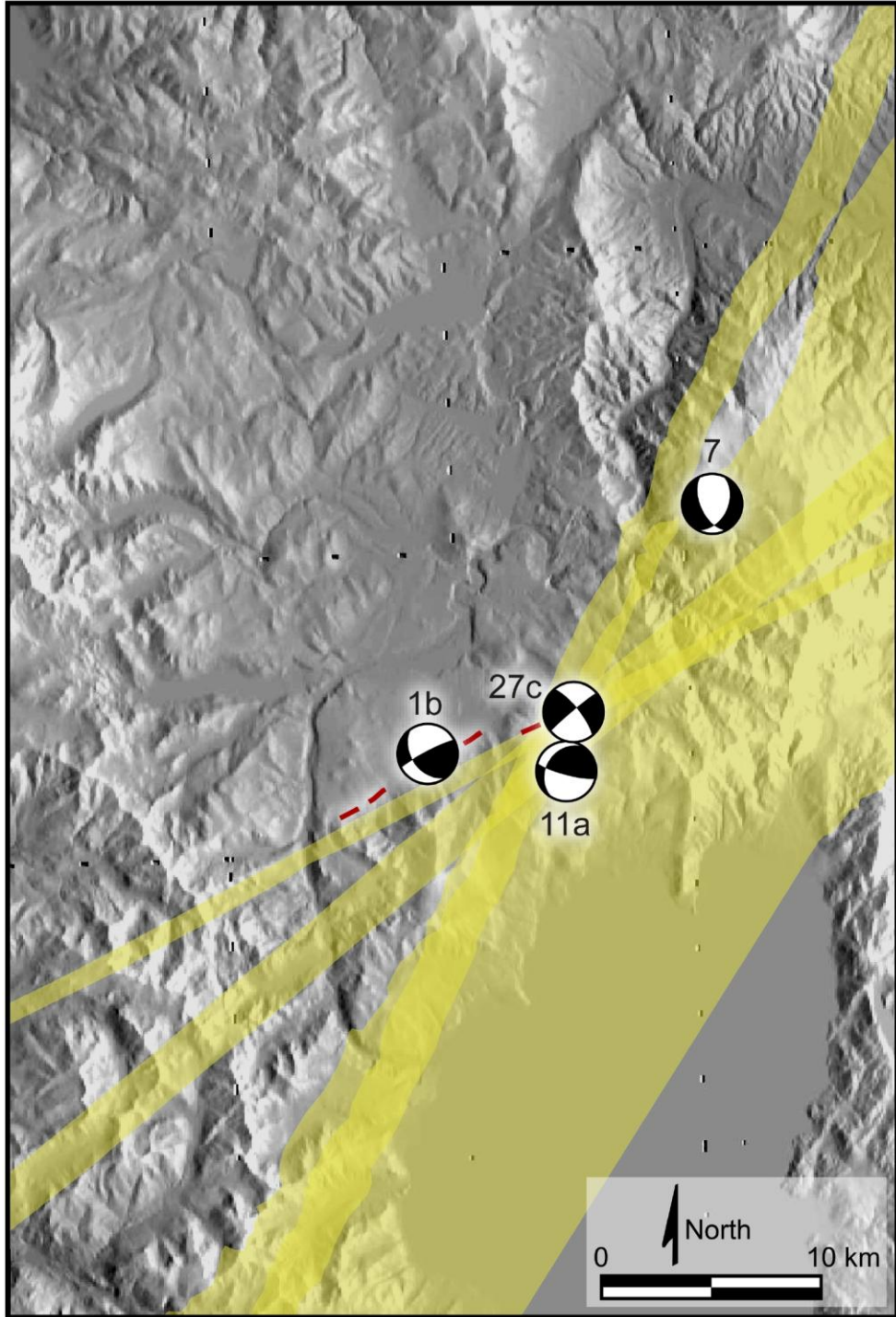


Figure 28. Martis Creek trend defined by overlapping seismo-lineaments (yellow) from focal mechanisms of earthquakes 1, 7, 11 and 27c.

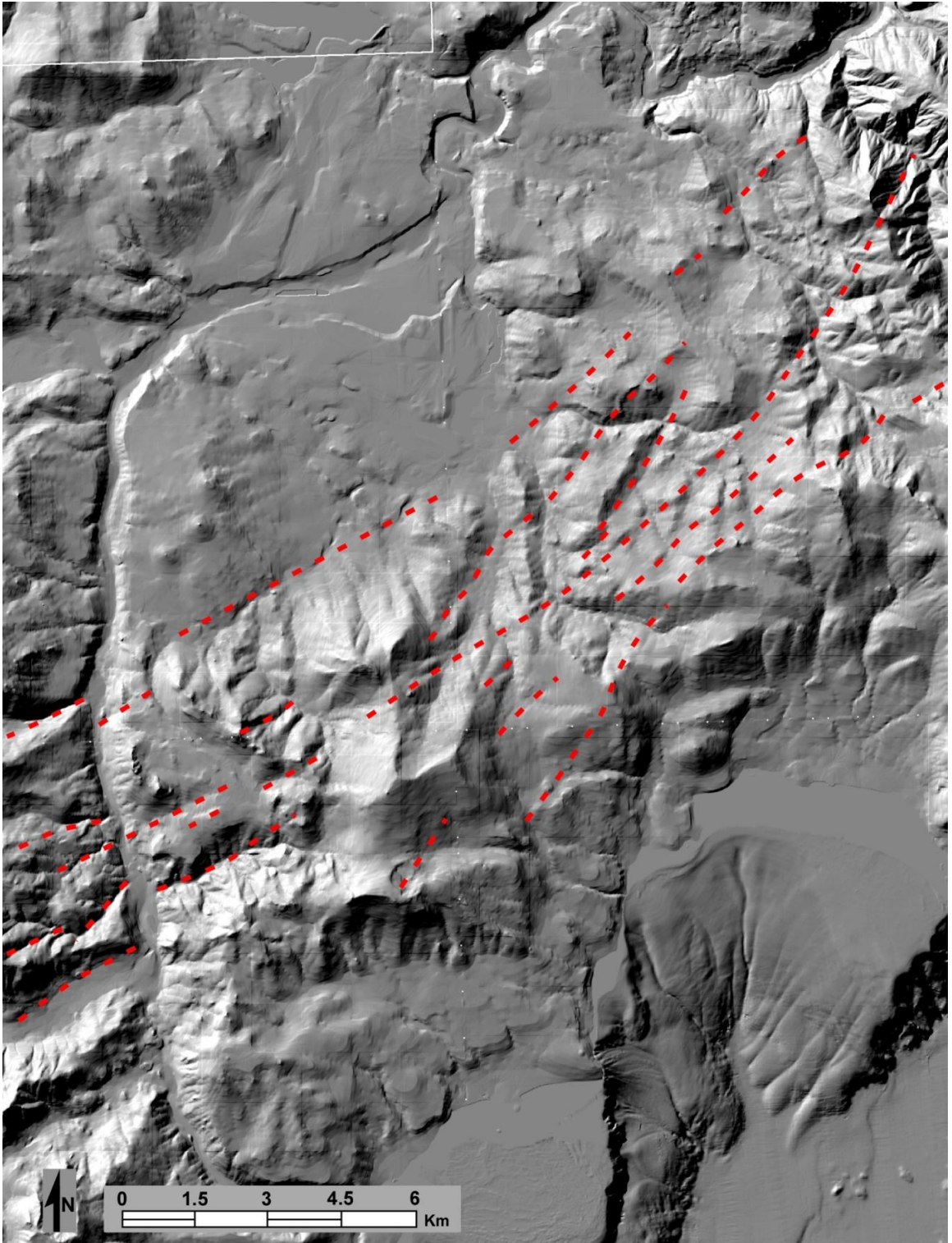


Figure 29. Martis Creek trend. Red dashed curves are prominent NE-SW trending geomorphic lineaments across the highland area drained by branches of Martis Creek, just north of Lake Tahoe.

faults. Further study using higher-resolution LiDAR data and aerial imagery preliminary to field investigation is warranted.

Synthesis

Schweickert and others (2004), describe transtensional deformation occurring between the northern Lake Tahoe region and the southern end of the Mohawk Valley fault zone, in a domain they called the Truckee Transition Zone (figure 30). Within this zone, they infer that conjugate strike-slip faults accommodate north-south crustal shortening, while extension is accommodated in the Tahoe Basin on north-striking east-dipping normal faults. Schweickert and others (2004) reference the dextral, northwest-striking Last Chance fault (Rogers and others, 1991) and two sinistral to sinistral-oblique trends that strike northeast: the Dog Valley fault zone and segments of the North Tahoe fault and Incline Village fault zone.

To this regional sketch map can now be added the northwest-striking dextral Polaris fault (Hunter and others, 2011). The inferred dextral faulting along the northwest-striking Prosser Creek trend and inferred sinistral faulting along the northeast-trending Martis Creek trend are consistent with the idea of conjugate strike-slip faulting in this domain. The variation in strike of these structures might be due to variations in horizontal stress axes across the area, or to a rotational component across the transition zone due to differential motion of the Sierra Nevada-Great Valley block relative to crust to the west of the Walker Lane.

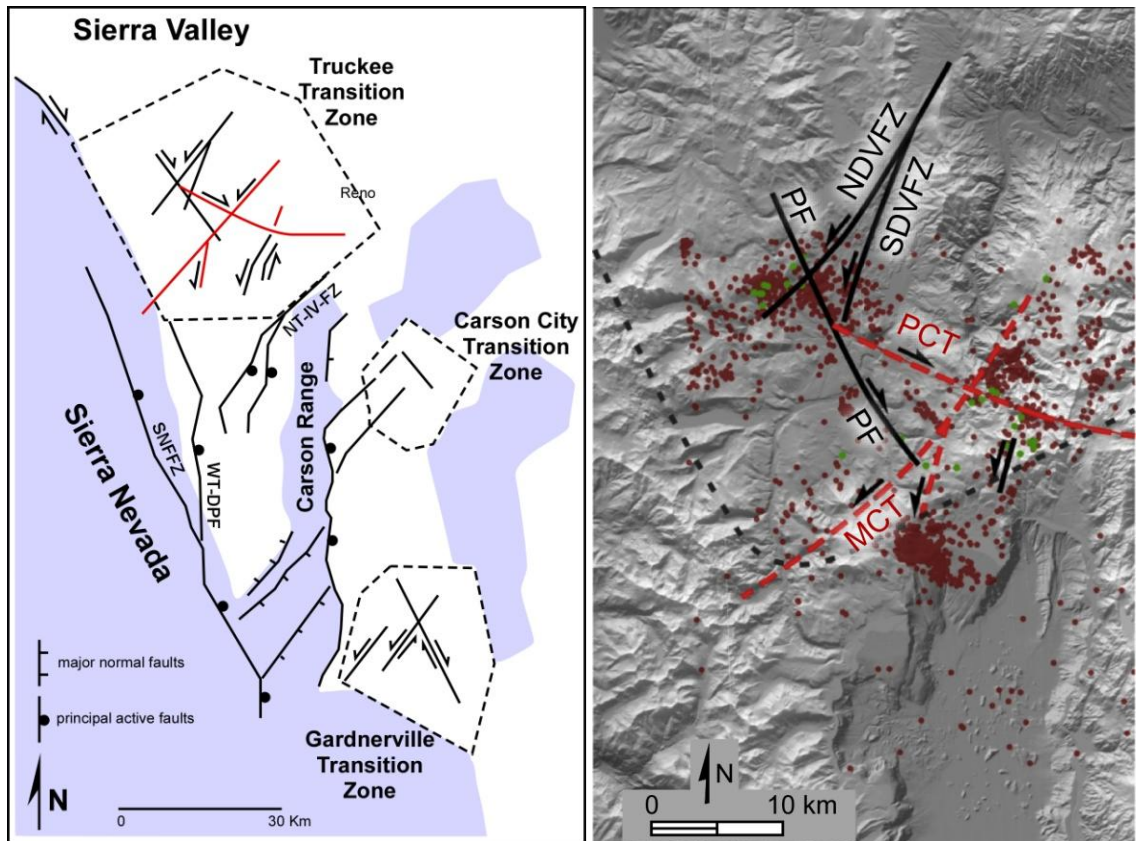


Figure 30. Interpretation of fault geometry in the study area. Sketch map at left is after Schweickert and others (2004). Black fault traces on both maps are previously mapped faults; red curves on both maps are seismicogenic trends identified in this thesis. Map at right includes epicenters from the NCEDC catalog ($M < 3.0$ = red dots, $M \geq 3.0$ = green dots). NDV-FZ = northern Dog Valley fault zone, SDV-FZ = southern Dog Valley fault Zone, PF = Polaris fault, PCT = Prosser Creek trend, MCT = Martis Creek trend.

An alternative explanation is that the northeast-trending sinistral faults (Dog Valley fault zone, hypothetical fault(s) along Martis Creek trend, segments of the North Tahoe fault and Incline Village fault zone) are cross faults between the more fundamental northwest-trending dextral faults (Mohawk Valley fault zone, Last Chance fault, Honey Lake fault zone, Polaris fault, hypothetical fault along the Prosser Creek trend, Dollar Point fault zone, \pm Tahoe-Sierra Nevada Frontal fault zone) that accommodate the motion of the Sierra Nevada-Great Valley block relative to the Basin and Range Province across

the Walker Lane (figures 6 and 7). This interpretation is analogous to the structural setting of faults in the transtensional Salton Trough, southern California, where a series of blocks exist between two major active northwest-striking dextral faults: the San Andreas fault and the San Jacinto fault (Hudnut and others, 1989). Between and subparallel to these major faults are a series of minor dextral faults, as well as a set of northeast-striking sinistral faults that are orthogonal or conjugate to the dominant faults.

CHAPTER SIX

Conclusions

Introduction

A primary goal of this research was to identify seismogenic faults in the north Tahoe area of California and Nevada. Prior studies described in chapter 2 identified faults that displace Quaternary strata in the north Tahoe area, including the Dog Valley fault zone, the Polaris fault, the Tahoe-Sierra Nevada Frontal fault zone, the West Tahoe-Dollar Point fault zone, the Incline Village fault zone and the North Tahoe fault (figure 4). Of these, only the Dog Valley fault zone had previously been associated with a recorded earthquake: the M 6 Truckee earthquake of 12 September 1966 (*e.g.*, Hawkins and others, 1986). The Incline Village earthquake of 30 October 1998 was broadly associated with the North Tahoe-Incline Village fault zone by Ichinose and others (1999); however, they recognized that the earthquake focus was located well within the footwall of that fault zone.

Published focal locations and source parameters from 29 earthquakes with reported magnitudes ≥ 3.0 were used in this study to map trends that might be related to seismogenic faulting. The results and interpretations are preliminary, given limitations in our understanding of the uncertainty associated with focal locations and nodal-plane orientations. Some individual seismo-lineaments correlated spatially with multiple known faults (*e.g.*, seismo-lineaments associated with earthquakes 13, 15, 16, 19, 21, 23, 24). Nodal planes from some earthquakes correlated spatially with two, conjugate/

orthogonal fault systems (*e.g.*, earthquakes 8, 9, 13, 14, 16, 25, 27), so differentiation of the fault plane from the auxiliary plane was ambiguous.

The Dog Valley fault zone, Polaris fault, West Tahoe fault, North Tahoe fault, Incline Village fault and the hypothetical Agate Bay fault all correlate spatially with one or more earthquakes, as noted in chapter 5 (table 4). None of the earthquakes included in this study correlated spatially with the hypothetical East Tahoe fault. Two trends defined by seismo-lineaments and geomorphic indicators of possible faulting, but along which no faults are currently mapped, were identified and named the Prosser Creek trend and the Martis Creek trend. The Prosser Creek trend might be along an unmapped northwest-striking dextral fault zone that passes through Prosser Creek Reservoir. The Martis Creek trend might be associated with an unmapped northeast-striking sinistral fault zone that traverses the highland area just northwest of the Lake Tahoe Basin. These possible seismogenic trends are a high priority for additional study because of their proximity to population centers and significant engineered structures.

Three fault exposures were observed during fieldwork related to this research. Faults at sites 7 and 19 appear to be newly recognized faults that are not included on the published maps reviewed for this thesis. The fault at site 20 is along the mapped trace of a segment of the Dog Valley fault zone. Geomorphic indicators of faulting are abundant in the north Tahoe area, but exposed fault traces are uncommon. Future work will necessarily include trench studies to find and characterize active faults.

Earthquakes in the north Tahoe area are interpreted to have occurred along northwest-striking dextral faults and northeast-striking sinistral faults that form conjugate/orthogonal systems, and along north-striking east-dipping normal faults. The

tectonic setting within the northern Walker Lane suggests that the northwest-striking dextral faults might predominate, with the northwest-trending sinistral faults acting as cross faults in a manner analogous to the transpressional Salton Trough in southern California.

Suggestions for Future Work

The digital elevation model used in this thesis had a reported horizontal resolution of 10 meters, and was appropriate for a large-area survey for possible seismogenic faults. Subsequent to the completion of the seismo-lineament analysis described in this thesis, LiDAR elevation point-cloud datasets for the north Tahoe area were made available through the Open Topography portal (<http://www.opentopography.org/>). These data were collected in August, 2010, and have an estimated vertical accuracy of 3.5 cm, and an average first-return pulse density of 11 per square meter – 2.26 per meter at ground level. The LiDAR-based data above lake level should then be merged with the lake-bottom data obtained by earlier multibeam seismic and shallow-water LiDAR surveys to build a seamless elevation map across the Tahoe Basin. Geomorphic analysis using these high-resolution elevation data along the seismo-lineament trends described in this thesis is a high priority.

All focal locations used in this thesis are based on single-event locations. Improved locations can often be obtained by joint relocation of sets of earthquakes, using one of several available relocation processes such as hypoDD (Waldhauser and Ellsworth, 2000; Waldhauser, 2001). With improved locations can come improved estimates of location uncertainty. It would also be very helpful to review or recompute each of the focal mechanism solutions, attempting to formally define the uncertainty in nodal plane

orientation (*e.g.*, Hardebeck and Shearer, 2002). Improved focal locations and focal-plane orientations, along with improved estimates for uncertainty, will allow revision of the seismo-lineaments in a manner that will improve our confidence in the results.

It would be very useful to compile all available, reliable fault-location data in an ArcGIS database, using published maps (*e.g.*, Saucedo, 2005; Sylvester and others, 2007), maps in published papers and reports (*e.g.*, Hawkins and others, 1986; Hunter and others, 2011; Schweickert and others, 2004) including agency files and open-file reports (*e.g.*, Olig and others, 2005a; Grose, 2000a-c; Carter, 1966; Burnett, 1982; Harwood and Fisher, 2002), maps from field-trip guidebooks (*e.g.*, Hunter and others, 2009; Seitz, 2009), maps from theses and dissertations (*e.g.*, Melody, 2009; Franks, 1980), and maps from engineering reports when they are available (*e.g.*, Kleinfelder-Geomatrix, 2009). Acquiring all relevant materials will be challenging, as will be the accurate transcription of map data into a digital map format. An additional challenge involves data quality assessment, so that speculative map-location information is differentiated from reliable observations of actual fault location obtained through field work and trenching.

Among the questions generated by this thesis research are the following: is there a seismogenic fault along the Prosser Creek trend, and is there a seismogenic fault along the Martis Creek trend? Use of the types of improved information resources just described will certainly help resolve these questions; however, a significant amount of field investigation will be necessary to test hypotheses generated by the analysis of these improved seismic and geomorphic data. Snow cover effectively limits the field season to the period from May through September. It would be advantageous to conduct field studies along the Prosser Creek trend in cooperation with the U.S. Army Corps of

Engineers and perhaps other public agencies that can arrange for trench studies to be conducted if tangible field evidence of youthful surface faulting is developed.

Finally, adding GPS stations within this actively deforming zone will provide data that will help resolve the network of active, seismogenic faults, building upon the work of Hammond and others (2011). Establishing and maintaining GPS stations and related infrastructure for data storage and analysis is a costly, long-term commitment; however, GPS geodesy is an essential tool for studying active tectonics. The data provided by GPS stations operated over decades will greatly enhance our understanding of seismic risk.

APPENDICES

APPENDIX A

SLAMCode *Mathematica* notebook used in this thesis.

```
startTime = AbsoluteTime[];
```

Projecting the nodal planes from a focal mechanism solution onto a digital elevation model surface

This code is copyright © 2004-2009 by Vincent S. Cronin. It may not be read, duplicated or used without his permission.

Written and revised by Vince Cronin for a research project of Vince Cronin, Brian Bayliss, Lauren Seidman, Mark Millard, Bruce Byars, and Lisa Zygo

Begun August 5, 2004; Revised July 23, 2009

Introduction

The purpose of this notebook is to describe how to define the intersection of a DEM surface and a plane of given orientation that passes through a particular point located below the DEM surface. The application of this is in estimating the surface trace of a fault plane defined by an earthquake focal mechanism solution. It is hoped that this technique, in conjunction with structural terrain analysis and field mapping, will assist in the identification of the surface traces of seismogenic faults. For more information about this code and its usage, refer to

Cronin, V.S., Millard, M.A., Seidman, L.E., and Bayliss, B.G., 2008, The Seismo-Lineament Analysis Method [SLAM] -- A reconnaissance tool to help find seismogenic faults: *Environmental and Engineering Geoscience*, v. 14, no. 3, p. 199-219.

Each fault surface is initially represented by an upward-directed unit vector that is normal to the fault plane and whose origin is at the earthquake focus. Each location vector to a point on the DEM surface grid is evaluated to determine whether it is within a user-defined region around 90° from the vector normal to the fault. If so, that grid location is identified as being along the surface trace of the fault plane, or within the uncertainty region around the fault plane. The result of evaluating every point on the DEM surface grid in this manner is a subset of points that collectively define the surface trace of the fault plane and the associated uncertainty region across the DEM surface.

The output from this application is a set of 3 files, whose names are defined by the user.

- One file is an encapsulated PostScript file (.eps) that contains the graphic showing the DEM shaded by elevation, the topographic contours at ~500 ft increments, curves marking the boundaries of the uncertainty region, and a curve showing the trace of the fault-plane solution intersection with the topography.
- Another file is a data file (.dat) with the same dimensions as the input DEM .dat file, but whose

values are either the null value (-9999) or, for points located along the trace of the fault-plane solution intersection with the topography, some other value (typically "1" or the DEM-derived elevation at that node point).

- The other file is a data file (.dat) with the same dimensions as the input DEM .dat file, but whose values are either the null value (-9999) or, for points located along the boundaries of the uncertainty region, some other value (typically "1" or the DEM-derived elevation at that node point).

Explanation of changes to this code that are necessary to evaluate another fault plane solution

(1) In the "Description of input data" section, the user must supply values for the following variables: focalLat, focalLong, reportedFocalDepthKm, faultDipTrend, faultDipPlunge, reportedVertError, horizError.

(2) In the "Import the DEM data from a DAT file" subsection of the "Digital elevation model (DEM)" section, the user may need to modify the path information so this notebook can find the input DEM/-DAT file.

(3) In the "Export data and image files" section at the end of this code, the user must supply different names for the output files to avoid over-writing the results of previous runs.

Description of input data

■ Data source for focal mechanism solution used in this run

<http://neic.usgs.gov/neis/sopar/20040603085446> <http://www.ncedc.org/ncedc/catalog-search.html> event

■ From focal mechanism solution

Epicenter location: latitude (focalLat) and longitude (focalLong) in decimal degrees.

```
focalLat = 39.3335;
```

```
focalLong = -120.0083;
```

Focal depth (focalDepthKm) in kilometers

```
reportedFocalDepthKm = 5.24;
```

Reported vertical (reportedVertError) and horizontal (horizError) uncertainties in the location of the earthquake focus, in kilometers.

```
reportedVertError = 2;
```

```
horizError = 1;
```

Trend (faultDipTrend) and plunge (faultDipPlunge) of dip vector of the fault plane, in decimal degrees

```
faultDipTrend1 = 84;
```

```
faultDipPlunge1 = 54;
```

```
faultDipTrend2 = 222;
```

```
faultDipPlunge2 = 44;
```

The central meridian of UTM Zone 10 (long -126 to -120) is -123, and for Zone 11 (long -120 to -114) is longitude -117°.

```
zoneMeridian = -123.
```

The maximum elevation in the input dataset is called maxElev, and is expressed in kilometers

```
maxElev = 3.32;
```

Some user-defined functions

```
makeVector[plunge_, trend_] := {Cos[plunge Degree] Sin[trend Degree],  
    Cos[plunge Degree] Cos[trend Degree], -Sin[plunge Degree]};
```

```
vectorNorm[x_] := Sqrt[x.x];
```

```
unitVector[x_] := {x[[1]] / vectorNorm[x],  
    x[[2]] / vectorNorm[x], x[[3]] / vectorNorm[x]};
```

```
vectorAngle[a_, b_] := ArcCos[a.b / (vectorNorm[a] vectorNorm[b])];
```

The lat/long to UTM conversion is after Snyder, 1982.

```

convertToUTM[inLat_, inLong_, centMerid_] :=
Module[{c1, c2, c3, c4, c5, v1, v2, v3, v4, v5, v6, utmX, utmY},
c1 = 6378206.4; c2 = 0.00676866; c3 = 0; c4 = centMerid; c5 = 0.9996;
v1 = c2 / (1 - c2); v2 = c1 / Sqrt[1 - (c2 * (Sin[inLat Degree]^2))];
v3 = Tan[inLat Degree]^2; v4 = v1 * (Cos[inLat Degree]^2);
v5 = (Cos[inLat Degree]) * ((inLong - c4) (π / 180));
v6 = (111132.0894 * inLat) - (16216.94 * Sin[2 * (inLat Degree)]) +
(17.21 * Sin[4 * (inLat Degree)]) - (0.02 * Sin[6 * (inLat Degree)]);
utmX = (c5 * v2 * (v5 + (((1 - v3 + v4) * v5^3) / 6) +
((5 - (18 * v3) + (v3^2) + (72 * v4) - (58 * v1)) * v5^5) / 120)) +
500000; utmY = c5 * (v6 - 0 + (v2 * Tan[inLat Degree] *
((v5^2 / 2) + (((5 - v3 + (9 * v4) + (4 * (v4^2))) * v5^4) / 24) +
(((61 - (58 * v3) + (v3^2) + (600 * v4) - (330 * v1)) * v5^6) /
720))))); {utmX, utmY}];

```

The following module differentiates between points that are within "width" meters from the fault plane and those that are further away. Given unit vector N that is normal to the fault plane that passes through the origin of the coordinate system, the distance from an arbitrary point (whose position vector is P) to that plane is given by |N·P|.

```

pointEvaluator[xCoord_, yCoord_, zCoord_, width_,
fltUNrml_, nulData_] := Module[{locVect, distToFlt, result},
locVect = {xCoord, yCoord, zCoord}; distToFlt =
If[{zCoord < (-1000)}, width, Abs[Dot[fltUNrml, locVect]]];
result = If[{distToFlt ≤ width}, zCoord, nulData]; result];

```

■ Defining the vertical extent of the uncertainty region around the earthquake focus

Defining the vertical extent of the uncertainty region around the earthquake focus is not always a simple matter of modifying the reported focal depth by the reported vertical error above and below the focus. In some cases, the combination of focal depth and stated vertical error yields locations that are above ground level, or below the reasonably expected depth of an earthquake focus in the area. The deepest reported earthquake in the west or central Santa Monica Mountains was a M2.9 event on February 1, 1994, located at longitude -119.17 and latitude 34.15, with a focal depth of 23 km (NEIC). The shallowest reported focal depths are less than 1 km. The highest elevation in the Santa Monica Mountains is Castro Peak, at 2,824 feet (861 meters).

The variable "upperBound" marks either the upper boundary of the crustal seismogenic zone (set at sea level) or the upper part of the uncertainty region for the earthquake focus, whichever is deeper.

```

upperBound = If[{(reportedFocalDepthKm - reportedVertError) < 0},
0, (reportedFocalDepthKm - reportedVertError)];

```

The variable "lowerBound" marks either the lower boundary of the crustal seismogenic zone (set at 23 km for the Malibu study) or the lower part of the uncertainty region for the earthquake

focus, whichever is shallower.

```
lowerBound = If[(reportedFocalDepthKm + reportedVertError) > 23,  
23., (reportedFocalDepthKm + reportedVertError)];
```

The variable "meanFocalDepthKm" is the depth half way between the upper bound and the lower bound.

```
meanFocalDepthKm = upperBound + ((lowerBound - upperBound) / 2);
```

In situations where the reported error bars cause us to consider the possibility of an earthquake focus that is in the atmosphere or below the regional norm for the base of the seismogenic zone, we use a "pseudofocus" located between the upper and lower boundaries of the seismogenic zone for the purpose of mapping the uncertainty swath across the DEM.

```
focalDepthKm = If[(meanFocalDepthKm == reportedFocalDepthKm),  
meanFocalDepthKm, reportedFocalDepthKm];
```

The "vertError" is half the vertical uncertainty in focus location, expressed in meters. In situations where a "pseudofocus" is used, the vertical error will differ from the reported vertical error, allowing us to map a more reasonable uncertainty swath across the DEM.

```
vertError = If[(focalDepthKm == reportedFocalDepthKm),  
(meanFocalDepthKm * 1000), (reportedVertError * 1000)];
```

Find the unit vector normal to the fault surface at the earthquake focus

Convert the fault dip vector from trend and plunge to a unit location vector (dipUnitVector)

```
faultDipUnitVector1 =  
unitVector[makeVector[faultDipPlunge1, faultDipTrend1]];
```

```
faultDipUnitVector2 =  
unitVector[makeVector[faultDipPlunge2, faultDipTrend2]];
```

Find the dip azimuth vector (dipAzimuthVector)

```
dipAzimuthVector1 =  
{Sin[faultDipTrend1 Degree], Cos[faultDipTrend1 Degree], 0};
```

```
dipAzimuthVector2 =  
{Sin[faultDipTrend2 Degree], Cos[faultDipTrend2 Degree], 0};
```

Find the strike vector (strikeVector) defined using the right-hand rule

```
faultStrikeTrend1 = faultDipTrend1 - 90;
```

```
strikeVector1 =  
{Sin[faultStrikeTrend1 Degree], Cos[faultStrikeTrend1 Degree], 0};
```

```

faultStrikeTrend2 = faultDipTrend2 - 90;

strikeVector2 =
    {Sin[faultStrikeTrend2 Degree], Cos[faultStrikeTrend2 Degree], 0};

```

Find the unit vector that is normal to the fault plane and is directed upwards (faultUnitNormal)

```

faultUnitNormal1 = unitVector [faultDipUnitVector1 × strikeVector1];

faultUnitNormal2 = unitVector [faultDipUnitVector2 × strikeVector2];

```

Digital elevation model (DEM)

The digital elevation model is presented as a set of z data in meters, with x and y coordinates explicit from the position of the z datum in the data file. The data file is derived from the U.S. Geological Survey's DEM data for the Pt. Dume, Malibu Beach and Topanga 7.5 minute quadrangles (30 m resolution).

DEM files can be acquired from the National Elevation Dataset, produced by the U.S. Geological Survey (USGS) and obtained from USGS web servers(<http://seamless.usgs.gov>), the Geocommunity web server (<http://data.geocomm.com>) or from www.gisdatadepot.com. The file can be in ASCII (DEM) format or Spatial Data Transfer Standard (SDTS) format.

■ Import the DEM data from a DAT file

The file pathway to the DEM file must be specified.

```

mydata = Import [
    "C:\SharedItems\TahoeResearch\MathematicaFiles\100mTahoeDEM.
dat";

```

■ Read and interpret the DEM header information

Read the header information.

```

headerData = Table[mydata[[i, j]], {i, 6}, {j, 2}]

```

"ncols" is the number of columns; label in position [[1,1]] and value in [[1,2]]

```

ncols = headerData[[1, 2]]

```

"nrows" is the number of rows; label in position [[2,1]] and value in [[2,2]]

```

nrows = headerData[[2, 2]]

```

"xllcorner" is the UTM zone 11 "x" coordinate, in meters, of the lower left corner of the DEM; label in position [[3,1]] and value in [[3,2]].

```
xllcorner = headerData [ 3, 2 ]
```

"yllcorner" is the UTM zone 11 "y" coordinate, in meters, of the lower left corner of the DEM; label in position [[4,1]] and value in [[4,2]]

```
yllcorner = headerData [ 4, 2 ]
```

"gridSpacing" a.k.a. "cellsize" is the distance between grid nodes in the DEM file, in meters; label in position [[5,1]] and value in [[5,2]]

Note that the code below uses the variable name "gridSpacing" rather than "cellsize."

```
cellsize = headerData [ 5, 2 ]
```

"nodata_value" is the value used in the data file to indicate that there is no data in a specific location in the data file; label in position [[6,1]] and value in [[6,2]]

```
nodataValue = headerData [ 6, 2 ]
```

The seventh row of the data set is the first data row.

The true UTM coordinates of the datum in position [[i,j]] of the data set (from row 7 to the end) are as follows:

x coordinate = $xllcorner + (cellsize * (j - 1))$ y coordinate = $yllcorner + (cellsize * (nrows - i))$

z coordinate = the datum in position [[i,j]]

The "gridspacing" is the distance between grid nodes in the DEM file, as we are going to work with the file.

```
gridSpacing = cellsize
```

Convert the input coordinates of the earthquake focus to the same coordinate system as the DEM data

```
utmCoordinates = convertToUTM[focalLat, focalLong, zoneMeridian];
```

The "focus" is the (x, y, z) coordinates in meters of the "pseudofocus" located at a depth half way between the upper and lower boundaries of the vertical uncertainty region, in a coordinate system in which the origin is the lower-left (southwest) corner of the DEM at sea level.

```
focus = { (utmCoordinates [ 1 ] - xllcorner),  
           (utmCoordinates [ 2 ] - yllcorner), (focalDepthKm * (-1000)) };
```

The "reptFocus" is the (x, y, z) coordinates in meters of the reported earthquake focus, in a coordinate system in which the origin is the lower-left (southwest) corner of the DEM at sea level.

```

reptFocus =
  {(utmCoordinates[[1]] - xllcorner), (utmCoordinates[[2]] - yllcorner),
   (reportedFocalDepthKm * (-1000))};

```

Define the threshold for resolving whether a point in the DEM is within the fault swath

The "zoneHalfWidth" is half the distance between the parallel planes that bound the uncertainty region for this fault-plane solution. The units are meters.

```

zoneHalfWidth1 = (vertError * Cos[faultDipPlunge1 Degree]) +
  (horizError * 1000 * Sin[faultDipPlunge1 Degree]);

zoneHalfWidth2 = (vertError * Cos[faultDipPlunge2 Degree]) +
  (horizError * 1000 * Sin[faultDipPlunge2 Degree]);

```

The "innerZone" is the minimal width of the surface trace of the fault-plane solution, needed to define the trace given the input grid spacing. The units are meters.

```

innerZone1 = ((1 * gridSpacing) * Sin[faultDipPlunge1 Degree]);

innerZone2 = ((1 * gridSpacing) * Sin[faultDipPlunge2 Degree]);

```

Define the location of the seismo-lineament associated with the first nodal plane

- Determine which points on the DEM lie along the modeled fault-plane trace, \pm the width of the "innerZone," and map the corresponding boundaries

The UTM coordinates of each point from the DEM are transformed to a coordinate system whose origin is at the earthquake focus

(focus = {(utmCoordinates[[1]]-xllcorner),(utmCoordinates[[2]]- yllcorner),(focalDepthKm*(-1000))}).

```

x coordinate=(gridSpacing*(j-1))-focus[[1]]      y coordinate=(gridSpacing*(nrows-i))-
focus[[2]]
z coordinate=(the datum in position [[i,j]])-focus[[3]]

```

```

inFaultTrace1 =
  Table[pointEvaluator[ ((gridSpacing * (j - 1)) - reptFocus[[1]]),
    ((gridSpacing * (nrows - i)) - reptFocus[[2]]),
    (mydata[[i + 6, j]] - reptFocus[[3]]), innerZone1,
    faultUnitNormal1, nodataValue], {i, nrows}, {j, ncols}];

```

```
elev11 = Table[inFaultTrace1[[i, j]], {i, nrows, 1, -1}, {j, ncols}];

traceImageFile11 = ListContourPlot[elev11,
  ContourShading → False, AspectRatio → Automatic, Contours → {0}]
```

- Determine which points on the DEM lie within the uncertainty swath for the fault location, \pm the width of the "zoneHalfWidth," and map the corresponding boundaries

```
uncertSwath1 =
  Table[pointEvaluator[((gridSpacing * (j - 1)) - focus[[1]]),
    ((gridSpacing * (nrows - i)) - focus[[2]]),
    (mydata[[i + 6, j]] - focus[[3]]), zoneHalfWidth1,
    faultUnitNormal1, nodataValue], {i, nrows}, {j, ncols}];

elev21 = Table[uncertSwath1[[i, j]], {i, nrows, 1, -1}, {j, ncols}];

traceImageFile21 = ListContourPlot[elev21,
  ContourShading → False, AspectRatio → Automatic, Contours → {0}]
```

- Combine the fault-trace map with the fault-swath map into a single graphic

```
traceImageFile1 = Show[%, traceImageFile11]
```

Define the location of the seismo-lineament associated with the second nodal plane

- Determine which points on the DEM lie along the modeled fault-plane trace, \pm the width of the "innerZone," and map the corresponding boundaries

The UTM coordinates of each point from the DEM are transformed to a coordinate system whose origin is at the earthquake focus

```
(focus = {(utmCoordinates[[1]]-xllcorner),(utmCoordinates[[2]]- yllcorner),(focalDepthKm*(-1000))}).
```

```
x coordinate=(gridSpacing*(j-1))-focus[[1]]      y coordinate=(gridSpacing*(nrows-i))-
focus[[2]]
```

```
z coordinate=(the datum in position [[i,j]])-focus[[3]]
```

```

inFaultTrace2 =
  Table[pointEvaluator[((gridSpacing * (j - 1)) - reptFocus[[1]]),
    ((gridSpacing * (nrows - i)) - reptFocus[[2]]),
    (mydata[[i + 6, j]] - reptFocus[[3]]), innerZone2,
    faultUnitNormal2, nodataValue], {i, nrows}, {j, ncols}];

elev12 = Table[inFaultTrace2[[i, j]], {i, nrows, 1, -1}, {j, ncols}];

traceImageFile12 = ListContourPlot[elev12,
  ContourShading -> False, AspectRatio -> Automatic, Contours -> {0}]

```

- Determine which points on the DEM lie within the uncertainty swath for the fault location, \pm the width of the "zoneHalfWidth," and map the corresponding boundaries

```

uncertSwath2 =
  Table[pointEvaluator[((gridSpacing * (j - 1)) - focus[[1]]),
    ((gridSpacing * (nrows - i)) - focus[[2]]),
    (mydata[[i + 6, j]] - focus[[3]]), zoneHalfWidth2,
    faultUnitNormal2, nodataValue], {i, nrows}, {j, ncols}];

elev22 = Table[uncertSwath2[[i, j]], {i, nrows, 1, -1}, {j, ncols}];

traceImageFile22 = ListContourPlot[elev22,
  ContourShading -> False, AspectRatio -> Automatic, Contours -> {0}]

```

- Combine the fault-trace map with the fault-swath map into a single graphic

```

traceImageFile2 = Show[%, traceImageFile12]

```

Plot a topographic contour map of the DEM, at a contour interval of 500 feet (152.4 meters)

```

demImageFile =
  Table[mydata[[i + 6, j]] - focus[[3]], {i, nrows}, {j, ncols}];

aratio = nrows / ncols
minval = 0;
maxval = Max[demImageFile]
relief = (maxval - minval)

elev3 = Table[demImageFile[[i, j]] + focus[[3]],
  {i, nrows, 1, -1}, {j, ncols}];

topoMap = ListContourPlot[elev3, ContourShading -> False,
  Frame -> False, AspectRatio -> aratio,
  Contours -> Table[c, {c, -152.3, 4400, 152.4}]]

```

```

ListDensityPlot[elev3, AspectRatio → aratio, Frame → False,
  Mesh → False, ColorFunction → Function[z, GrayLevel[0.3 + 0.7 z]]]

shadedTopoMap = Show[%, topoMap]

semifinalImage = Show[%, traceImageFile1]

finalImage = Show[%, traceImageFile2]

```

■ Add the original header data to the output files

```

mergedData = Join[headerData, inFaultTrace];

mergedSwathData = Join[headerData, uncertSwath];

```

■ Export data and image files

The file created in the next line is a data file (.dat) with the same dimensions as the input DEM .dat file, but whose values are either the null value (-9999) or, for points located along the trace of the fault-plane solution intersection with the topography, some other value (typically "1" or the DEM-derived elevation at that node point).

```

Export["/Users/vince/Desktop/20031031010718aseisLina.dat", mergedData];

```

The file created in the next line is a data file (.dat) with the same dimensions as the input DEM .dat file, but whose values are either the null value (-9999) or, for points located along the boundaries of the uncertainty region, some other value (typically "1" or the DEM-derived elevation at that node point).

```

Export["/Users/vince/Desktop/20031031010718bseisLina.dat", mergedSwathData];

```

The file created in the next line is an encapsulated PostScript file (.eps) that contains the graphic showing the DEM shaded by elevation, the topographic contours at ~500 ft increments, curves marking the boundaries of the uncertainty region, and a curve showing the trace of the fault-plane solution intersection with the topography.

```

Export["/Users/vince/Desktop/Tahoe20040603085445a.eps", finalImage, "EPS"];

```

```

ClearAll[mergedData, mergedSwathData, traceImageFile,
  traceImageFile1, traceImageFile2, finalImage, shadedTopoMap,
  mydata, inFaultTrace, uncertSwath, elev1, elev2, elev3];

```

■ How long did this program take to run, in minutes?

```

minutesForProcessing = (AbsoluteTime[] - startTime) / 60

```

References

Colley, S.J., 2002, Vector calculus [2nd edition]: Upper Saddle River, New Jersey, Prentice-Hall, 558 p., (pp. 43-50), ISBN 0-13-041531-6.

Cronin, V.S., and Sverdrup, K.A., 1998, Preliminary assessment of the seismicity of the Malibu Coast Fault Zone, southern California, and related issues of philosophy and practice, *in* Welby, C.W., and Gowan, M.E. [editors], A Paradox of Power--Voices of Warning and Reason in the Geosciences: Geological Society of America, Reviews in Engineering Geology, p. 123-155.

Cronin, V.S., Byars, B.W., and Gammill, T., 2003, Developing techniques for regional structural interpretation using GIS and DEM-based terrain analysis: Geological Society of America, Abstracts with Programs, v. 34, no. 7, p. 261. http://gsa.confex.com/gsa/2003AM/finalprogram/abstract_61851.htm

Cronin, V.S., Millard, M.A., Seidman, L.E., and Bayliss, B.G., 2008, The Seismo-Lineament Analysis Method [SLAM] -- A reconnaissance tool to help find seismogenic faults: Environmental and Engineering Geoscience, v. 14, no. 3, p. 199-219.

Davis, H.F., and Snider, A.D., 1987, Introduction to vector analysis [5th edition]: Boston, Allyn and Bacon, 365 p. (pp. 34-37), ISBN 0-205-10263-8.

Gammill, T., Cronin, V.S., and Byars, B.W., 2004, Combining earthquake focal data and digital map analysis in reconnaissance for active faults, central Santa Monica Mountains and northern Santa Monica Bay, California: Geological Society of America, Abstracts with Programs, v. 36, no. 5, http://gsa.confex.com/gsa/2004AM/finalprogram/abstract_80352.htm

Haneberg, W.C., 2004, Computational geosciences with *Mathematica*: Berlin, Springer-Verlag, 381 p., CD, ISBN 3-540-40245-4.

Snyder, J.P., 1982, Map projections used by the U.S. Geological Survey: U.S. Geological Survey Bulletin 1532, pp. 63-69 and 233-235.

APPENDIX B

FisherStatsSD.nb *Mathematica* notebook used in this thesis.

Fisher Statistics, Strike & Dip Version

FisherStatsSD.nb available at http://bearspace.baylor.edu/Vince_Cronin/www/MathematicaCode/FisherStatsSD.nb

© 2011 by Vincent S. Cronin. This code may be used for non - profit educational and scientific purposes with appropriate attribution to the original author (Vincent S. Cronin).

Version 1.0. Begun January 21, 2011; revised January 27, 2011

Introduction

Mathematica code to use Fisher statistics (Fisher, 1953) to find the mean and 95% confidence interval of a set of data that characterize several spot orientations of a surface. The input data are in an Excel spreadsheet, and consist of strikes and dip angles.

Data

■ Description of input data

Fisher statistics are used to find the mean and characterize the dispersion around the mean of a set of vectors. They can also be used to find the mean orientation of planes by using dip vectors or the vectors normal to the planes as input data. The input data include the right-hand-rule strike azimuth, in degrees (range of azimuth is 0 to 360°), and the plunge of the dip vector in degrees (range of dip angle is 0 to 90°).

This notebook assumes that the input values will be integers, because the uncertainty inherent in a Brunton compass or other pocket transit is on the order of 1°. Hence, the output data are in integers.

■ Making a data file in Excel

The input data is an Excel spreadsheet (.xls file) in which each record/row has 2 values/columns. The first column contains the right-hand-rule strike azimuth, in degrees, and the second column has the plunge of the dip vector (*i.e.*, the dip angle), in degrees. The right-hand-rule strike azimuth is 90° anticlockwise from the trend of the dip vector.

■ Finding the Excel data file on your computer

Each user will need to ensure that the path to the input data file is correctly specified in the first input line of this notebook (*i.e.*, in the blue box below). For example, a correct specification for the file "rawData.xls" located on the desktop of Vince Cronin's office Mac Pro computer would look like this:

```
mydata = Import["/Users/vince/Desktop/rawData.xls"];
```

and the specification for the file "OB7_Fisher.xls" located in the TahoeRuns directory on the C drive of Cronin's Dell computer would look like this:

```
mydata=Import["C:\TahoeRuns\OB23_Fisher.xls"];
```

In the code immediately following this text, be certain that the path to the input data file is correctly specified.

```
mydata = Import ["/Users/vince/Desktop/ryanSite7.xls"];
```

```
inData0 = Flatten[mydata, 1] ;
```

Computation

■ Functions defined in this notebook

The function **findVector** converts orientation data for a vector, expressed as the trend and plunge of the vector, to the corresponding 3 D Cartesian unit vector coordinates.

```
findVector[vectTrend_, vectPlunge_] :=  
  {Sin[vectTrend Degree] Cos[vectPlunge Degree],  
   Cos[vectTrend Degree] Cos[vectPlunge Degree],  
   -Sin[vectPlunge Degree]};
```

The function **cart2TrendPlunge** converts from a 3 D Cartesian unit vector to trend and plunge. A downward plunge has a positive sign.

```
cart2TrendPlunge[inVector_] := Module[{a, unitA, trend, plunge},  
  plunge = -ArcSin[inVector[[3]]] (180 /  $\pi$ );  
  a = {inVector[[1]], inVector[[2]]};  
  unitA = {a[[1]] / Norm[a], a[[2]] / Norm[a]};  
  trend = If[(unitA[[1]] < 0), (360 - (ArcCos[unitA[[2]]] (180 /  $\pi$ ))),  
    (ArcCos[unitA[[2]]] (180 /  $\pi$ ))]; {trend, plunge};
```

The module **equalAreaPlot** computes the {x,y} coordinates for an equal-area stereonet of a vector whose orientation is given in terms of trend and plunge expressed in degrees. This module is based on the assumption that the stereonet has a unit radius (*i.e.*, radius = 1). The first element of **inTrendPlunge** is the trend (azimuth measured clockwise from north), and the second is the plunge angle (measured from horizontal, positive down, negative up).

```

equalAreaPlot[inTrendPlunge_] :=
Module[{radius, xCoord, yCoord}, radius = 1;

xCoord = radius  $\sqrt{2}$  Sin[ $\left(\frac{\pi}{4}\right) - \left(\frac{\text{inTrendPlunge}[[2]] \left(\frac{\pi}{180}\right)}{2}\right)$ ];

Sin[inTrendPlunge[[1]]  $\left(\frac{\pi}{180}\right)$ ];

yCoord = radius  $\sqrt{2}$  Sin[ $\left(\frac{\pi}{4}\right) - \left(\frac{\text{inTrendPlunge}[[2]] \left(\frac{\pi}{180}\right)}{2}\right)$ ];

Cos[inTrendPlunge[[1]]  $\left(\frac{\pi}{180}\right)$ ]; {xCoord, yCoord}];

```

The function **round2Int** rounds an arbitrary number to the nearest integer value.

```

round2Int[x_] := Round[IntegerPart[x * 10] / 10];

```

■ Input the nodal plane data

These are data for nodal plane 9 B

```

npDipAzimuth = 245;

```

```

npDipAngle = 50;

```

```

npDipVector = {npDipAzimuth, npDipAngle};

```

```

xMatrixNP =

```

$$\begin{pmatrix} 1 & 0 & 0 \\ 0 & \text{Cos}[(90 - \text{npDipAngle}) \text{Degree}] & -\text{Sin}[(90 - \text{npDipAngle}) \text{Degree}] \\ 0 & \text{Sin}[(90 - \text{npDipAngle}) \text{Degree}] & \text{Cos}[(90 - \text{npDipAngle}) \text{Degree}] \end{pmatrix};$$

```

zMatrixNP =

```

$$\begin{pmatrix} \text{Cos}[-\text{npDipAzimuth Degree}] & -\text{Sin}[-\text{npDipAzimuth Degree}] & 0 \\ \text{Sin}[-\text{npDipAzimuth Degree}] & \text{Cos}[-\text{npDipAzimuth Degree}] & 0 \\ 0 & 0 & 1 \end{pmatrix};$$

Define sets of points in circles oriented with a radius of 10, 20 and 30 degrees around a vector pointing straight down.

```

vectorPlunge10 = 80;

```

```

vectorPlunge20 = 70;

```

```

vectorPlunge30 = 60;

```

```

initSmCircle10 = Table[{i, vectorPlunge10}, {i, 0, 360, 10}];

```

```

initSmCircle20 = Table[{i, vectorPlunge20}, {i, 0, 360, 10}];

```

```

initSmCircle30 = Table[{i, vectorPlunge30}, {i, 0, 360, 10}];

```

```
matrixSizeNP = Dimensions[initSmCircle10];
```

Variable `ptsAroundCircle` is the number of points used to define the small circle.

```
ptsAroundCircleNP = matrixSizeNP[[1]];

initSmCircCart10 =
  Table[findVector[initSmCircle10[[i, 1]], initSmCircle10[[i, 2]]],
    {i, ptsAroundCircleNP}];

initSmCircCart20 =
  Table[findVector[initSmCircle20[[i, 1]], initSmCircle20[[i, 2]]],
    {i, ptsAroundCircleNP}];

initSmCircCart30 =
  Table[findVector[initSmCircle30[[i, 1]], initSmCircle30[[i, 2]]],
    {i, ptsAroundCircleNP}];

rotSmCircCart100 =
  Table[{zMatrixNP.xMatrixNP.initSmCircCart10[[i]]},
    {i, ptsAroundCircleNP}];

rotSmCircCart200 =
  Table[{zMatrixNP.xMatrixNP.initSmCircCart20[[i]]},
    {i, ptsAroundCircleNP}];

rotSmCircCart300 =
  Table[{zMatrixNP.xMatrixNP.initSmCircCart30[[i]]},
    {i, ptsAroundCircleNP}];

rotSmCircCart10 = Flatten[rotSmCircCart100, 1];
rotSmCircCart20 = Flatten[rotSmCircCart200, 1];
rotSmCircCart30 = Flatten[rotSmCircCart300, 1];

rotSmCircTP10 = Table[
  cart2TrendPlunge[rotSmCircCart10[[i]]], {i, ptsAroundCircleNP}];
rotSmCircTP20 = Table[
  cart2TrendPlunge[rotSmCircCart20[[i]]], {i, ptsAroundCircleNP}];
rotSmCircTP30 = Table[
  cart2TrendPlunge[rotSmCircCart30[[i]]], {i, ptsAroundCircleNP}];

plotSmCircDataFile10 =
  Table[equalAreaPlot[rotSmCircTP10[[i]]], {i, ptsAroundCircleNP}];
plotSmCircDataFile20 =
  Table[equalAreaPlot[rotSmCircTP20[[i]]], {i, ptsAroundCircleNP}];
plotSmCircDataFile30 =
  Table[equalAreaPlot[rotSmCircTP30[[i]]], {i, ptsAroundCircleNP}];

part9 = Graphics[
  {PointSize[Small], Green, Point[equalAreaPlot[npDipVector]]}];
part10 = Graphics[Line[plotSmCircDataFile10];
```

```
part11 = Graphics [Line [plotSmCircDataFile20]];
part12 = Graphics [Line [plotSmCircDataFile30]];
```

■ Define the sample size

```
matrixSize1 = Dimensions [inData0];
```

Variable **noInputVectors** is the number of vectors in the set. It is equivalent to the variable "N" in Cronin (2008).

```
noInputVectors = matrixSize1 [[1]];
```

■ Convert strike & dip data to dip vector data

The following step converts the input strike-and-dip data to trend-and-plunge vector data for the corresponding dip vectors. The input strike data must be expressed using the right - hand - rule convention.

```
inData = Table [{If [(inData0 [[i, 1]] < 270),
    (inData0 [[i, 1]] + 90), (inData0 [[i, 1]] - 270)],
    inData0 [[i, 2]]}, {i, noInputVectors}];
```

■ Proceed with vector analysis

Variable **dirCosines** is a table of the direction cosines $\{l, m, n\}$ for each of the input vectors (equation 1 from Cronin, 2008).

```
dirCosines =
    Table [{Cos [inData [[i, 2]] Degree] Cos [inData [[i, 1]] Degree],
    Cos [inData [[i, 2]] Degree] Sin [inData [[i, 1]] Degree],
    Sin [inData [[i, 2]] Degree]}, {i, noInputVectors}];
```

Variable **meanDirCos** includes the set of three direction cosines for the mean dip vector (equation 2 from Cronin, 2008).

```
meanDirCos = Total [dirCosines, 1];
```

Variable **capR** is the length of the mean dip vector (equation 3 from Cronin, 2008). It is equivalent to the variable "R" in Cronin (2008).

$$\text{capR} = \sqrt{\text{meanDirCos} [[1]]^2 + \text{meanDirCos} [[2]]^2 + \text{meanDirCos} [[3]]^2};$$

Variable **meanUnitVector** is the set of coordinates for the mean unit dip vector (equation 4 from Cronin, 2008).

```
meanUnitVector =
    {  $\frac{\text{meanDirCos} [[1]]}{\text{capR}}$ ,  $\frac{\text{meanDirCos} [[2]]}{\text{capR}}$ ,  $\frac{\text{meanDirCos} [[3]]}{\text{capR}}$  };
```

Variable **delta** is the plunge angle of the mean dip vector in radians (equation 5 from Cronin, 2008). It is equivalent to the variable "δ" in Cronin (2008).

```
delta = ArcSin [meanUnitVector [[3]]];
```

Variable **meanDipTrend** is the trend of the mean dip vector in degrees (equation 6 from Cronin, 2008).

$$\text{meanDipTrend} = \text{If} \left[(\text{meanUnitVector}[[2]] < 0), \right. \\ \left. \left((2\pi) - \text{ArcCos} \left[\frac{\text{meanUnitVector}[[1]]}{\text{Cos}[\text{ArcSin}[\text{meanUnitVector}[[3]]]]} \right] \right) (180/\pi), \right. \\ \left. \left(\text{ArcCos} \left[\frac{\text{meanUnitVector}[[1]]}{\text{Cos}[\text{ArcSin}[\text{meanUnitVector}[[3]]]]} \right] \right) (180/\pi) \right];$$

Variable **meanStrike** is the trend of the mean strike azimuth measured clockwise from north in degrees (equation 6 from Cronin, 2008), determined using the right-hand-rule convention -- the RHR strike is 90° anticlockwise from the trend of the dip vector.

$$\text{meanStrike} = \\ \text{If}[(\text{meanDipTrend} < 90), (\text{meanDipTrend} + 270), (\text{meanDipTrend} - 90)];$$

Variable **k** is the precision parameter, which ranges from 0 for a vector set that is strongly noncolinear to infinity for vectors that are perfectly colinear, as when $N = R$ (equation 7 from Cronin, 2008).

$$k = \frac{\text{noInputVectors} - 1}{\text{noInputVectors} - \text{capR}};$$

Variable **alpha95** is the angular radius of the 95% confidence cone around the mean vector, in radians (equation 8 from Cronin, 2008). It is equivalent to the variable " α_{95} " in Cronin (2008).

$$\text{alpha95} = \text{ArcCos} \left[1 - \left(\frac{\text{noInputVectors} - \text{capR}}{\text{capR}} \right) \left(\left(\frac{1}{0.05} \right)^{\frac{1}{\text{noInputVectors} - 1}} - 1 \right) \right];$$

Variable **theta** is an intermediate value in the computation of the uncertainty in the azimuth of the vector (equation 10 from Cronin, 2008). It is equivalent to the variable " θ " in Cronin (2008).

$$\text{theta} = \text{ArcSin} \left[\frac{\text{Sin}[\text{alpha95}] \text{Sin}[\text{delta}]}{\text{Cos}[\text{alpha95}] \text{Cos}[\text{delta}]} \right];$$

Variable **beta** is the uncertainty in the azimuth of the vector (equation 12 from Cronin, 2008). It is equivalent to the variable " β " in Cronin (2008).

$$\text{beta} = \text{ArcTan} \left[\frac{\text{Sin}[\text{alpha95}] \text{Cos}[\text{theta}]}{(\text{Cos}[\text{alpha95}] \text{Cos}[\text{delta}]) - (\text{Sin}[\text{alpha95}] \text{Sin}[\text{theta}] \text{Sin}[\text{delta}])} \right];$$

Round numerical output to integers

$$\text{meanDipAzimuth} = \text{round2Int}[\text{meanDipTrend}]; \\ \text{meanStrike} = \text{round2Int}[\text{meanStrike}]; \\ \text{strikeUncertainty} = \text{round2Int}[\text{beta} (180/\pi)]; \\ \text{meanDipAngle} = \text{round2Int}[\text{delta} (180/\pi)];$$

```
alphaNinetyFive = round2Int[alpha95 (180 / π)];
precisionParameterK = round2Int[k];
```

Graphics

■ Computation

```
meanLine = {meanDipAzimuth, meanDipAngle};
xMatrix1 =
  ⎡ 1           0           0 ⎤
  ⎢ 0 Cos[(90 - meanDipAngle) Degree] -Sin[(90 - meanDipAngle) Degree] ⎥;
  ⎢ 0 Sin[(90 - meanDipAngle) Degree]  Cos[(90 - meanDipAngle) Degree] ⎥
zMatrix1 = ⎡ Cos[-meanDipAzimuth Degree] -Sin[-meanDipAzimuth Degree] 0 ⎤
  ⎢ Sin[-meanDipAzimuth Degree]  Cos[-meanDipAzimuth Degree] 0 ⎥;
  ⎢ 0           0           1 ⎥
```

Define a set of points in a circle oriented with a radius of alpha 95 degrees around a vector pointing straight down.

```
vectorPlunge = 90 - (round2Int[alpha95 (180 / π)]);
initSmCircle = Table[{i, vectorPlunge}, {i, 0, 360, 10}];
matrixSize2 = Dimensions[initSmCircle];
```

Variable `ptsAroundCircle` is the number of points used to define the small circle.

```
ptsAroundCircle = matrixSize2[[1]];
initSmCircCart = Table[findVector[initSmCircle[[i, 1]],
  initSmCircle[[i, 2]]], {i, ptsAroundCircle}];
rotSmCircCart0 = Table[{zMatrix1.xMatrix1.initSmCircCart[[i]]},
  {i, ptsAroundCircle}];
rotSmCircCart = Flatten[rotSmCircCart0, 1];
rotSmCircTP = Table[
  cart2TrendPlunge[rotSmCircCart[[i]]], {i, ptsAroundCircle}];
plotSmCircDataFile =
  Table[equalAreaPlot[rotSmCircTP[[i]]], {i, ptsAroundCircle}];
part1 = Graphics[Circle[{0, 0}, 1]];
part2 =
  Graphics[Line[{{{0, 0.01}, {0, -0.01}}, {{0.01, 0}, {-0.01, 0}},
  {{0, 1}, {0, 0.95}}, {{0, -1}, {0, -0.98}},
  {{1, 0}, {0.98, 0}}, {{-1, 0}, {-0.98, 0}}}}];
```

See also `PlotMarkers` under `ListPlot`

```
part3 = Graphics[Line[plotSmCircDataFile]];
```

```

part4 = Graphics[
  {PointSize[Small], Red, Point[equalAreaPlot[meanLine]]};
rawPoints = Table[equalAreaPlot[inData[[i]], {i, noInputVectors}];
part5 = Graphics[{PointSize[Small], Point[rawPoints]};

```

■ Plot the plane and the pole to the plane

Define a set of points that will trace a great - circle arc on the final stereo plot

```

rawGreatCircle =
  {{270, 0}, {270, 10}, {270, 20}, {270, 30}, {270, 40}, {270, 50},
   {270, 60}, {270, 70}, {270, 80}, {270, 90}, {90, 80}, {90, 70},
   {90, 60}, {90, 50}, {90, 40}, {90, 30}, {90, 20}, {90, 10}, {90, 0}};
ptsAlongGrCirc = 19;
initGrCircCart = Table[findVector[rawGreatCircle[[i, 1]],
  rawGreatCircle[[i, 2]]], {i, ptsAlongGrCirc}];
rotGrCircCart0 = Table[
  {zMatrix1.xMatrix1.initGrCircCart[[i]]}, {i, ptsAlongGrCirc}];
rotGrCircCart = Flatten[rotGrCircCart0, 1];
rotGrCircTP =
  Table[cart2TrendPlunge[rotGrCircCart[[i]]], {i, ptsAlongGrCirc}];
plotGrCircDataFile =
  Table[equalAreaPlot[rotGrCircTP[[i]]], {i, ptsAlongGrCirc}];
part6 = Graphics[Line[plotGrCircDataFile]];
xMatrix2 =
  
$$\begin{pmatrix} 1 & 0 & 0 \\ 0 & \cos[-(\text{meanDipAngle}) \text{Degree}] & -\sin[-(\text{meanDipAngle}) \text{Degree}] \\ 0 & \sin[-(\text{meanDipAngle}) \text{Degree}] & \cos[-(\text{meanDipAngle}) \text{Degree}] \end{pmatrix};$$

zMatrix2 =
  
$$\begin{pmatrix} \cos[-\text{meanDipAzimuth Degree}] & -\sin[-\text{meanDipAzimuth Degree}] & 0 \\ \sin[-\text{meanDipAzimuth Degree}] & \cos[-\text{meanDipAzimuth Degree}] & 0 \\ 0 & 0 & 1 \end{pmatrix};$$

rotSmCircCartB = Table[{zMatrix2.xMatrix2.initSmCircCart[[i]]},
  {i, ptsAroundCircle}];
rotSmCircCart2 = Flatten[rotSmCircCartB, 1];
rotSmCircTP2 = Table[
  cart2TrendPlunge[rotSmCircCart2[[i]]], {i, ptsAroundCircle}];
plotSmCircDataFile2 =
  Table[equalAreaPlot[rotSmCircTP2[[i]]], {i, ptsAroundCircle}];
temp3 = Line[plotSmCircDataFile2];

```

```

part7 = Graphics[{Dashed, Blue, temp3}];
meanPole = {If[(meanDipAzimuth < 180), meanDipAzimuth + 180,
meanDipAzimuth - 180], (90 - meanDipAngle)};
part8 = Graphics[
{PointSize[Small], Blue, Point[equalAreaPlot[meanPole]}]};

```

Output

The numerical output below is rounded to the nearest integer value. All angles and azimuths are expressed in degrees.

```

meanDipAzimuth
meanStrike
strikeUncertainty
meanDipAngle
alphaNinetyFive
precisionParameterK

```

The graphics below are lower - hemisphere equal - area projections, with the longer tick mark at the top of the circle directed north and the cross in the middle of the circle (*i.e.*, at the bottom of the projection hemisphere).

The stereo plot below includes a small circle with a radius of alpha95 (α_{95}) degrees showing the projection of the cone - shaped uncertainty region around the mean dip vector (the red dot).

```

Show[part1, part2, part3, part4]

```

The stereo plot below includes a small circle with a radius of alpha95 (α_{95}) degrees showing the projection of the cone - shaped uncertainty region around the mean dip vector (the red dot). It also shows the dip vector of the nodal plane (the green dot) and three concentric small circles with angular radii of 10, 20 and 30 degrees.

```

Show[part1, part2, part3, part4, part9, part10, part11, part12]

```

The stereo plot below includes the dip vectors of the input planar data (black dots) in addition to the features of the previous plot.

```

Show[part1, part2, part3, part4, part5]

```

The stereo plot below includes the trace (*i.e.*, a great - circle arc) of the mean/average plane in addition to the features of the previous plot.

```

Show[part1, part2, part3, part4, part5, part6]

```

The stereo plot below includes the pole (blue dot) of the mean/average plane and the associated 95% CI uncertainty region (blue dashed circle/ellipse), in addition to the features of the previous plot.

```

Show[part1, part2, part3, part4, part5, part6, part7, part8]

```

References Cited and Other Relevant Texts

- Batschelet, E., 1981, **Circular Statistics in Biology**: London, Academic Press, 371 p.
- Borradaile, G., 2003, **Statistics of Earth Science Data, Their Distribution in Time, Space, and Orientation**: Berlin, Springer-Verlag, 351 p.
- Brunton Company, 2000, Pocket Transit Instruction Manual, The Brunton Company Riverton, WY. 25 p.
- Compton, R.R., 1962, **Manual of Field Geology**: New York, John Wiley & Sons, 378 p.
- Cronin, V.S., 2008, Finding the mean and 95 % confidence interval of a set of strike - and - dip or lineation data: *Environmental and Engineering Geoscience*, v.14, no.2, p.113 - 119.
- Fisher, N.I., Lewis, T., and Embleton, B.J.J., 1987, **Statistical Analysis of Spherical Data**: Cambridge, UK, Cambridge University Press, 329 p.
- Fisher, R.A., 1953, Dispersion on a sphere: *Proceedings Royal Society, London*, v. A217, no. 1130. p. 295-305.
- Irving, E., 1964, **Paleomagnetism and its Application to Geological and Geophysical Problems**: New York, John Wiley & Sons, 399 p.
- Mardia, K.V., 1972, **Statistics of Directional Data**: London, Academic Press, 357 p.
- Opdyke, N.D., and Channell, J.E.T., 1996, **Magnetic Stratigraphy**: San Diego, California, Academic Press, 346 p.
- Tarling, D.H., 1971, **Principles and Applications of Palaeomagnetism**: London, Chapman and Hall, 164 p.
- Tauxe, L., 1998, **Paleomagnetic Principles and Practices**: Dordrecht, Kluwer Academic Publishers, 299 p.

APPENDIX C

Location of field sites

Name	Latitude	Longitude
Site 1	39.2501	-119.9789
Site 2	39.2482	-119.9718
Site 3	39.2354	-119.9341
Site 4	39.2507	-119.9884
Site 5	39.2370	-120.0156
Site 6	39.2736	-120.0399
Site 7	39.2717	-120.0963
Site 8	39.3130	-120.1457
Site 9	39.3159	-120.2508
Site 10	39.3417	-120.3233
Site 11	39.3390	-120.1338
Site 12	39.3649	-120.1165
Site 13	39.4512	-120.0067
Site 14	39.3799	-120.1367
Site 15	39.3978	-120.1085
Site 16	39.3803	-120.0595
Site 17	39.3944	-120.0903
Site 18	39.4148	-120.0918
Site 19	39.4390	-120.0971
Site 20	39.4770	-120.1031
Site 21	39.4155	-120.0986
Site 22	39.4143	-120.1819
Site 23	39.5265	-120.2900
Site 24	39.5141	-120.0812
Site 25	39.5081	-120.1319
Site 26	39.3187	-120.1266
Site 27	39.3223	-120.1173
Site 28	39.3222	-120.1172
Site 29	39.3268	-120.1153
Site 30	39.3277	-120.1123

APPENDIX D

Fisher statistics, sites 7 and 19

Site 7

User-supplied input values

Number of measurements (N)	7
Instrument (compass) error	$\pm 1^\circ$
Probability	0.05

	Strike	Dip angle
First measurement	348°	56°
Second measurement	345°	51°
Third measurement	336°	55°
Fourth measurement	339°	58°
Fifth measurement	350°	54°
Sixth measurement	354°	54°
Seventh measurement	351°	49°

Output values

Mean strike	346°
95% CI uncertainty in strike	6°
Mean dip angle	54°
95% CI uncertainty in dip angle	4°
k (class I if $k \geq 10$)	276

Site 19

User-supplied input values

Number of measurements (N)	7
Instrument (compass) error	$\pm 1^\circ$
Probability	0.05

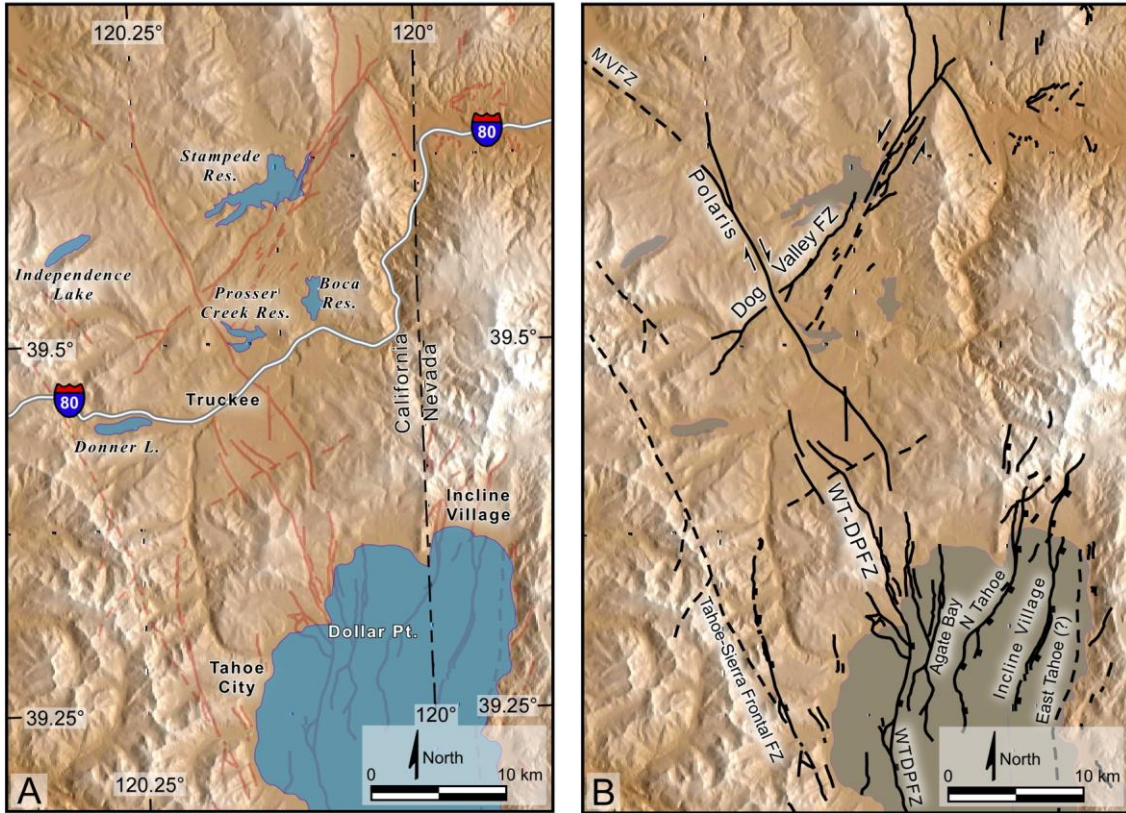
	Strike	Dip angle
First measurement	15°	78°
Second measurement	18°	81°
Third measurement	20°	85°
Fourth measurement	22°	83°
Fifth measurement	13°	82°
Sixth measurement	18°	81°
Seventh measurement	20°	84°

Output values

Mean strike	18°
95% CI uncertainty in strike	13°
Mean dip angle	82°
95% CI uncertainty in dip angle	2°
k (class I if $k \geq 10$)	1191

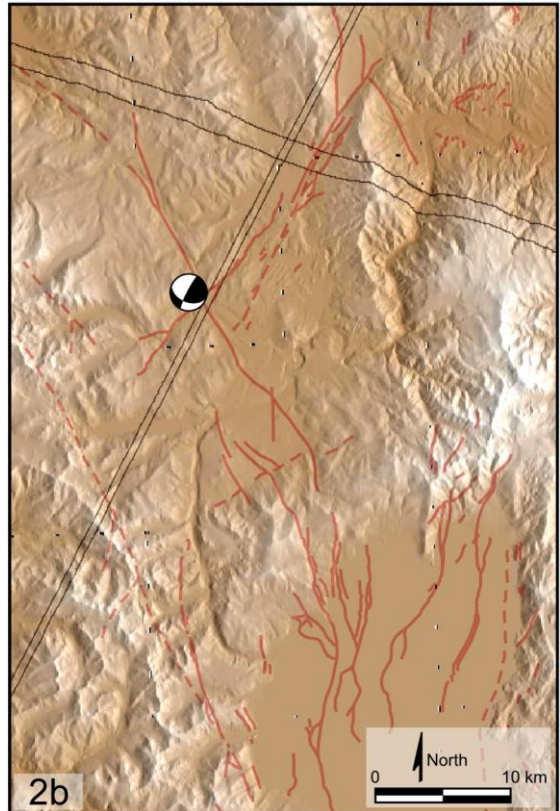
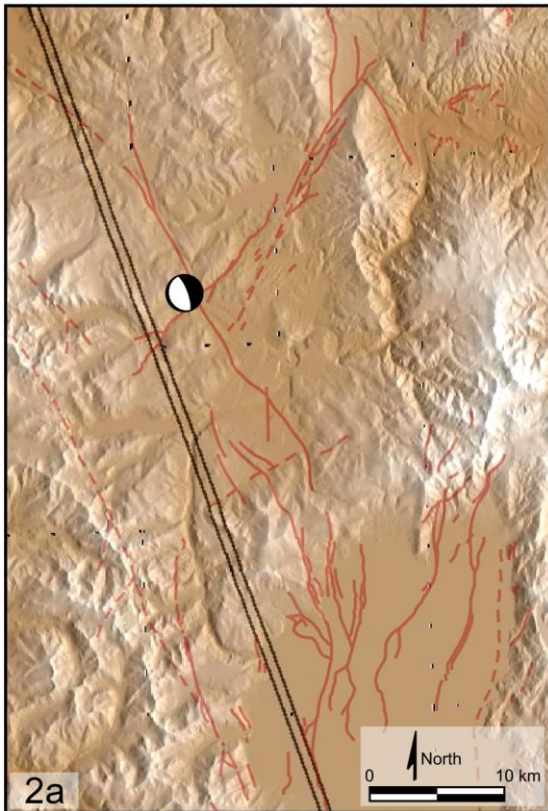
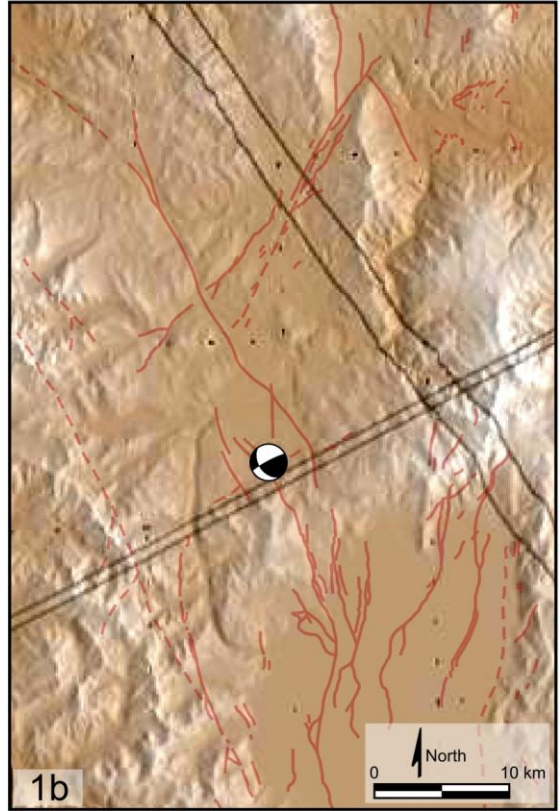
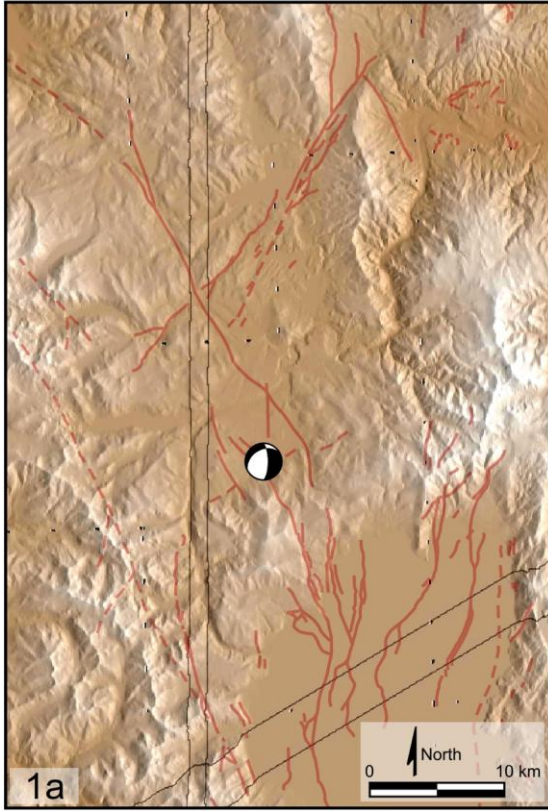
APPENDIX E

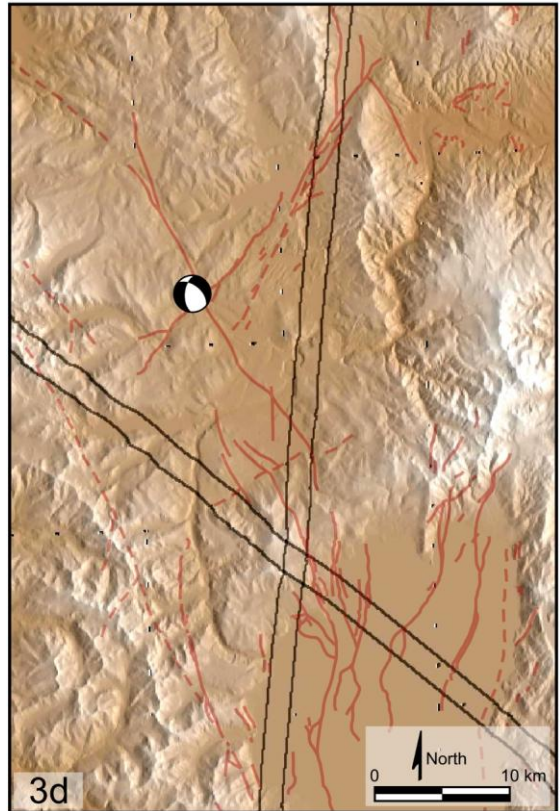
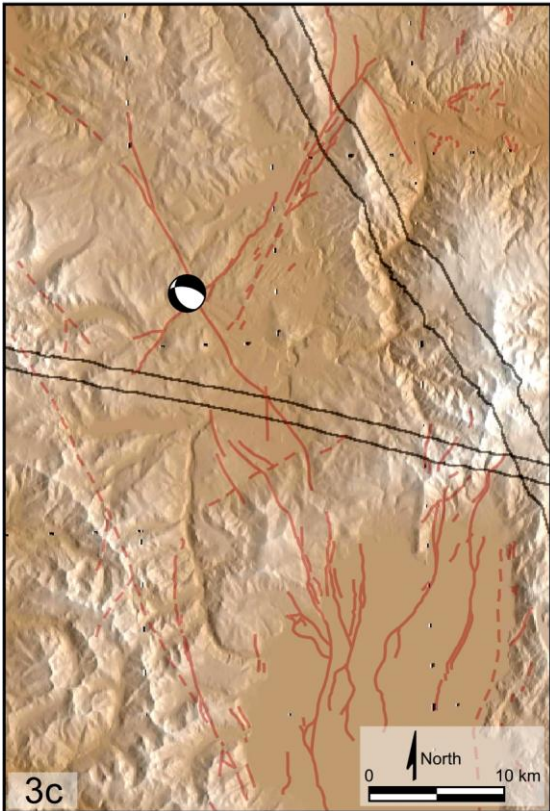
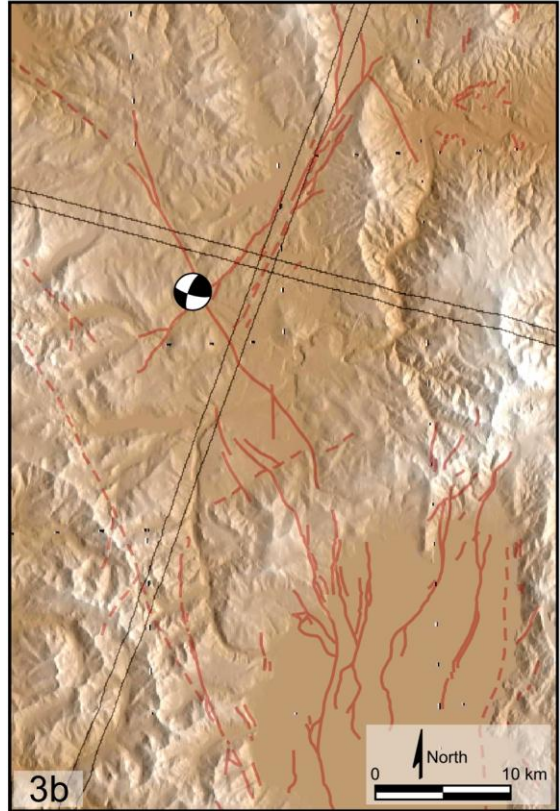
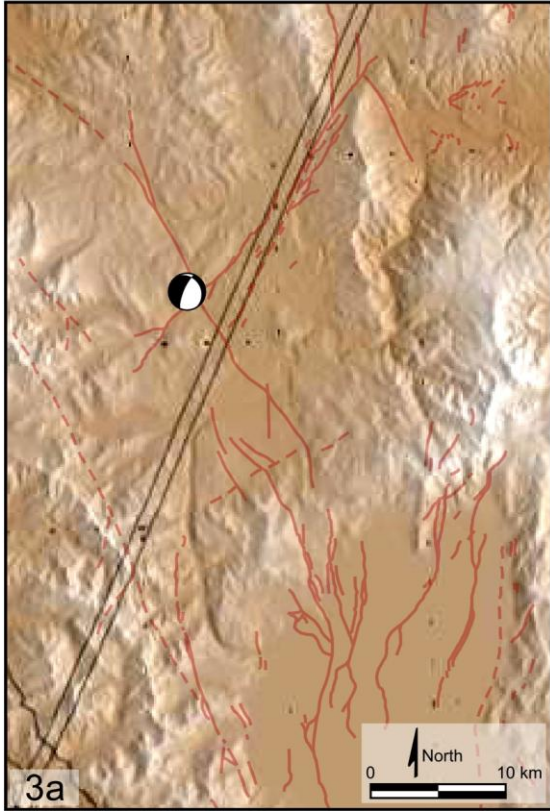
Output seismo-lineament maps from SLAMCode.nb.

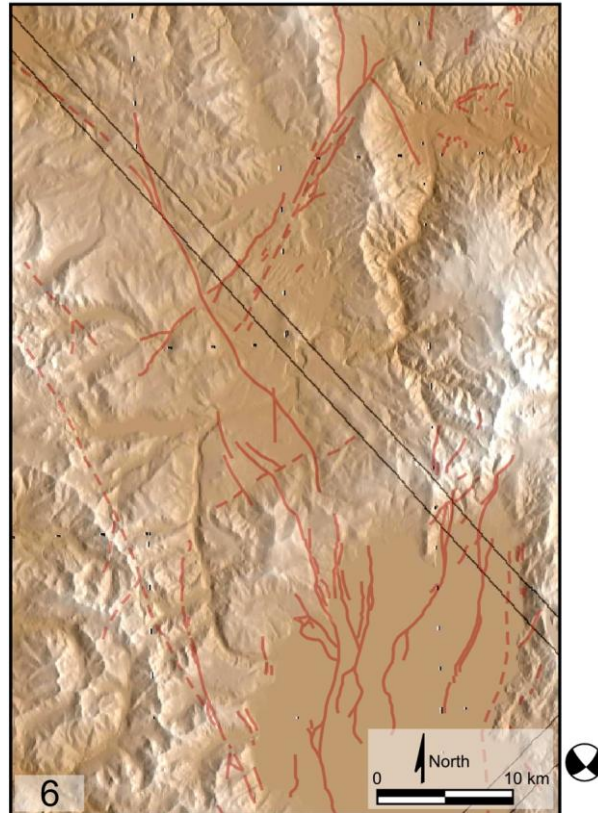
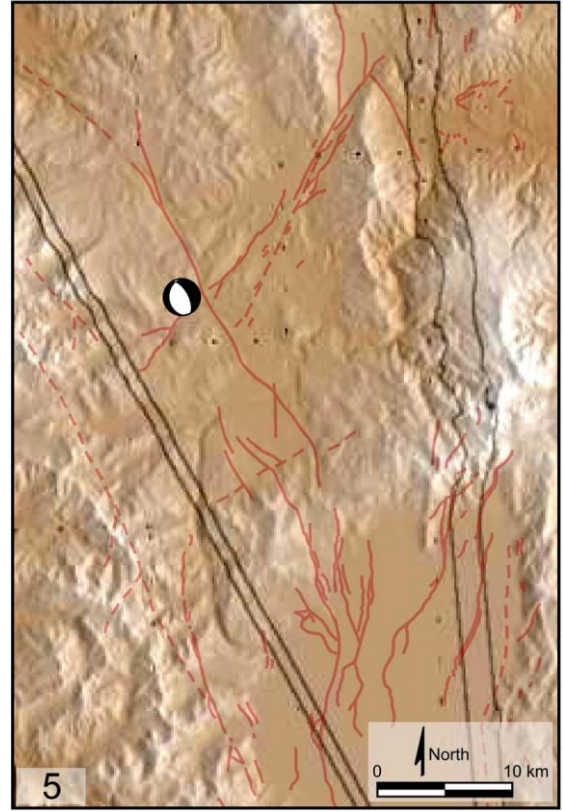
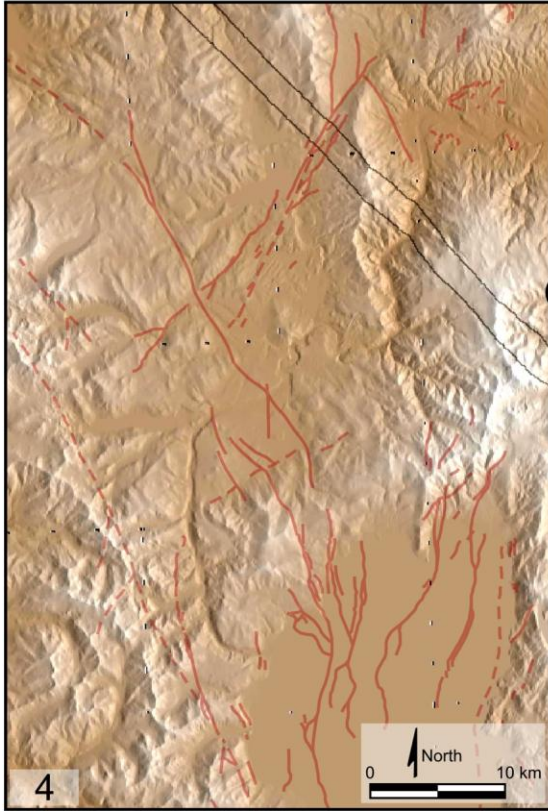


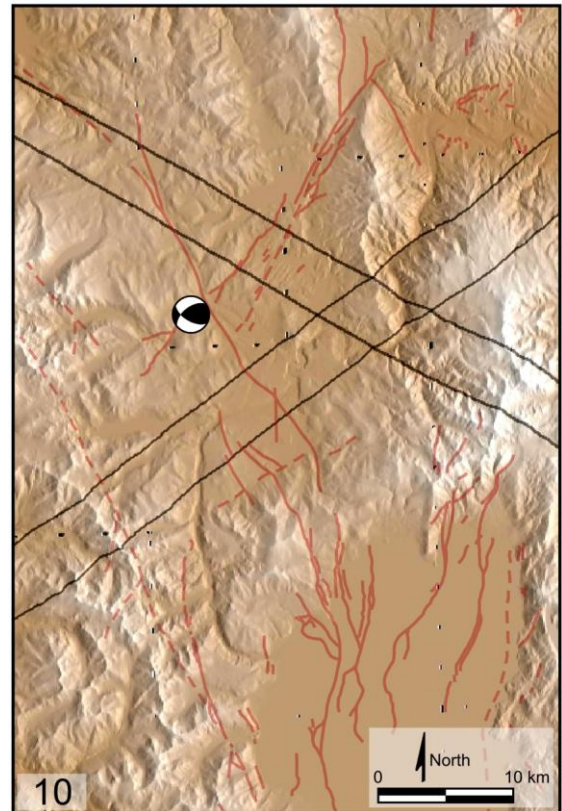
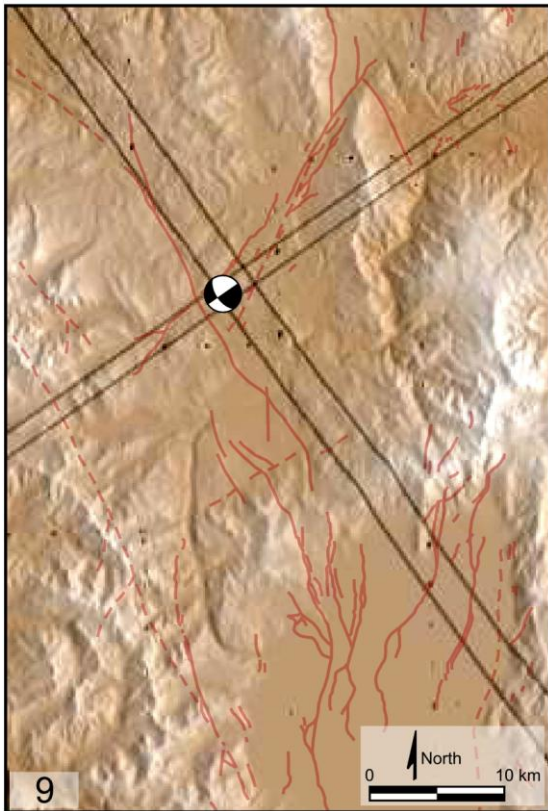
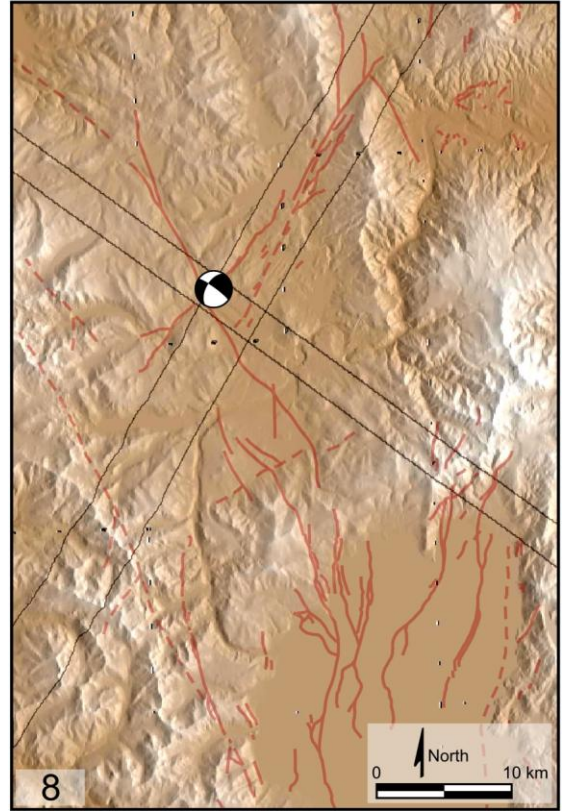
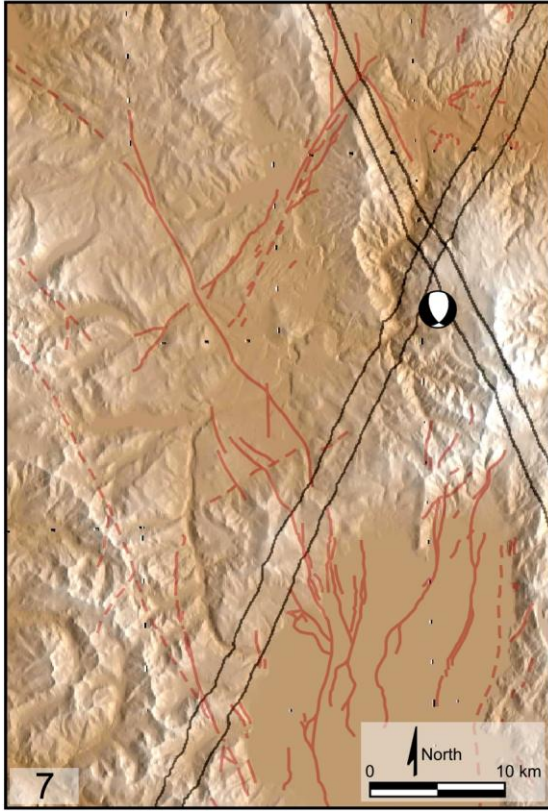
[A] Location map that coincides with the seismo-lineament maps in this appendix. [B] Primary mapped or inferred faults in the study area. These faults are indicated with red curves on the seismo-lineament maps that follow. MVFZ = Mohawk Valley fault zone; WTDPFZ = West Tahoe-Dollar Point fault zone.

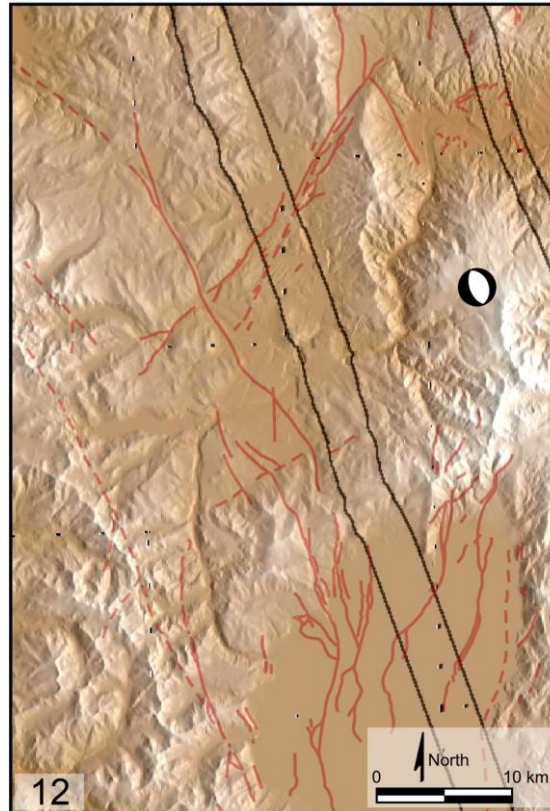
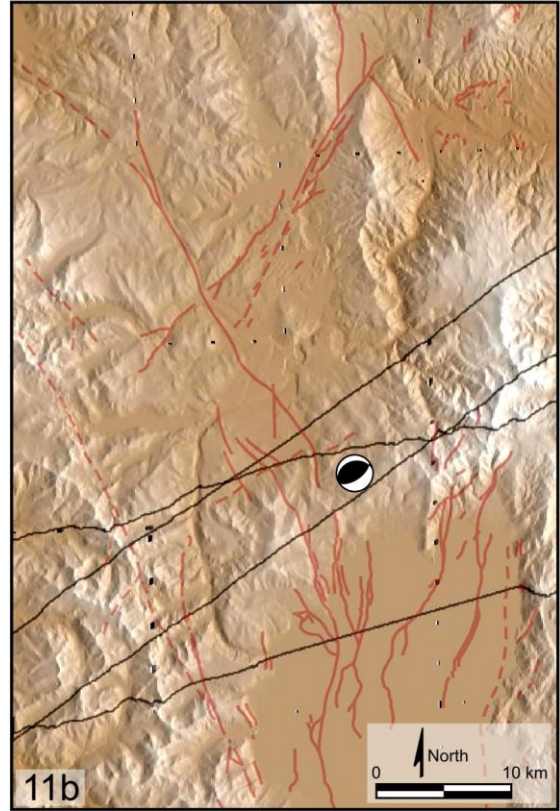
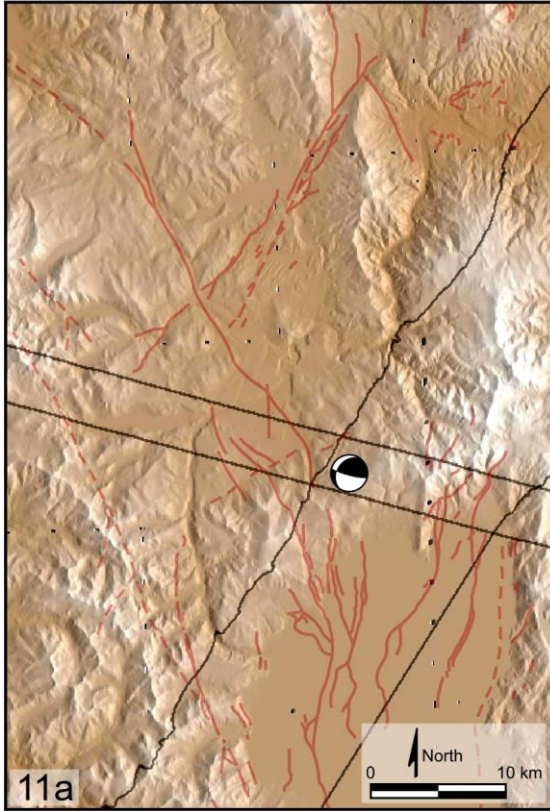
The maps presented in this appendix are created using the graphics output of the SLAMCode *Mathematica* notebook. The earthquakes are numbered as in Table 1, and each map has the corresponding earthquake number in the lower-left corner. All focal mechanism diagrams are equal-area lower-hemisphere stereographic projections plotted using an application by Scherbaum and others (accessed 2011). Hillshade image is illuminated from the east at an elevation of 15° from horizontal.

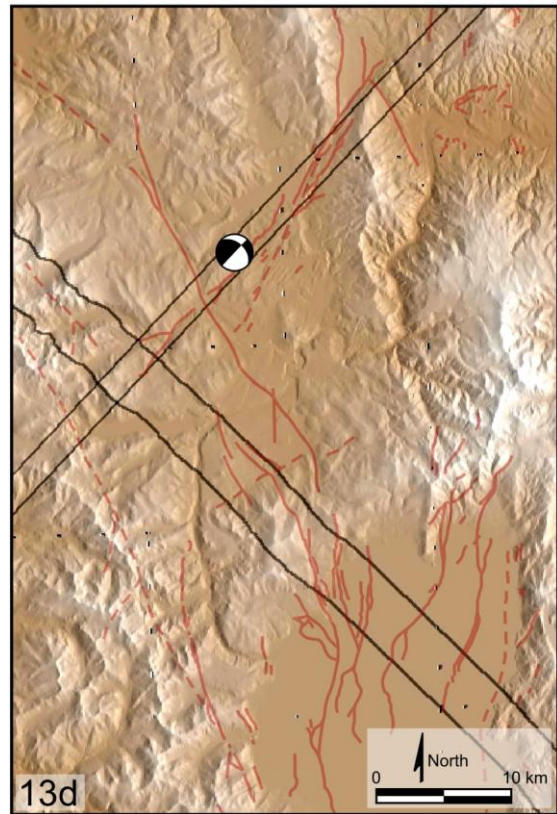
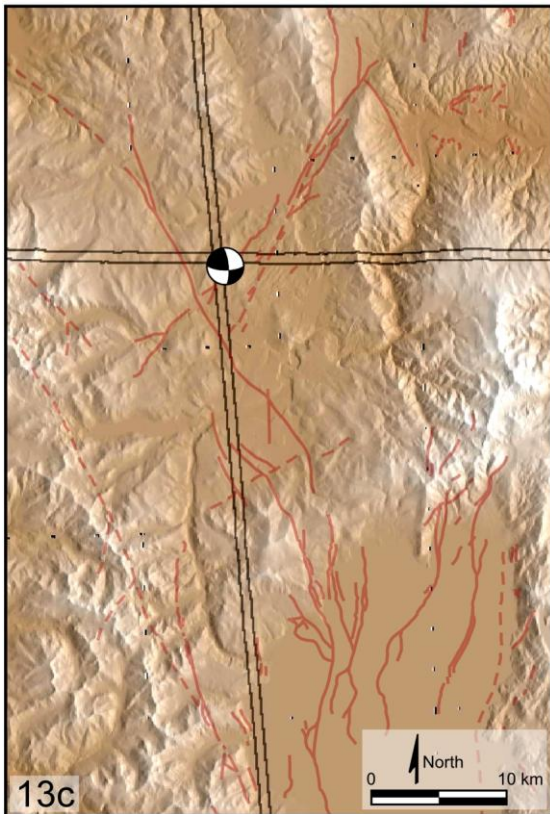
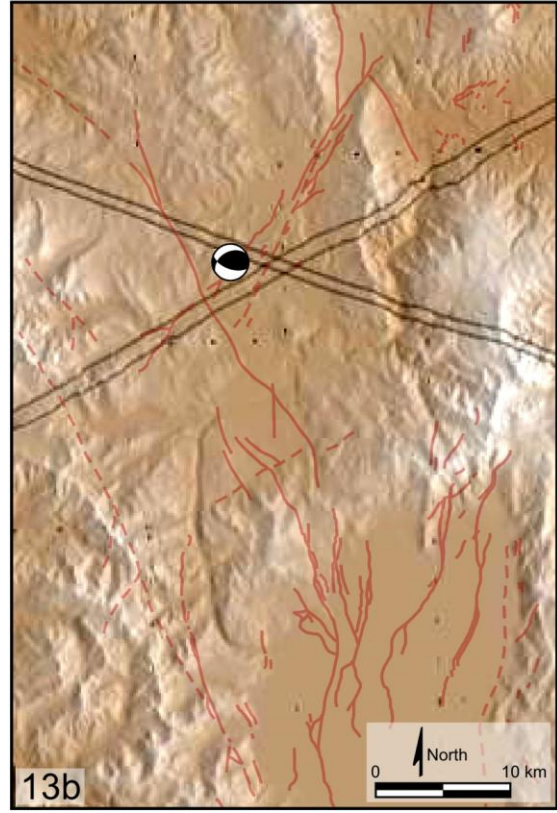
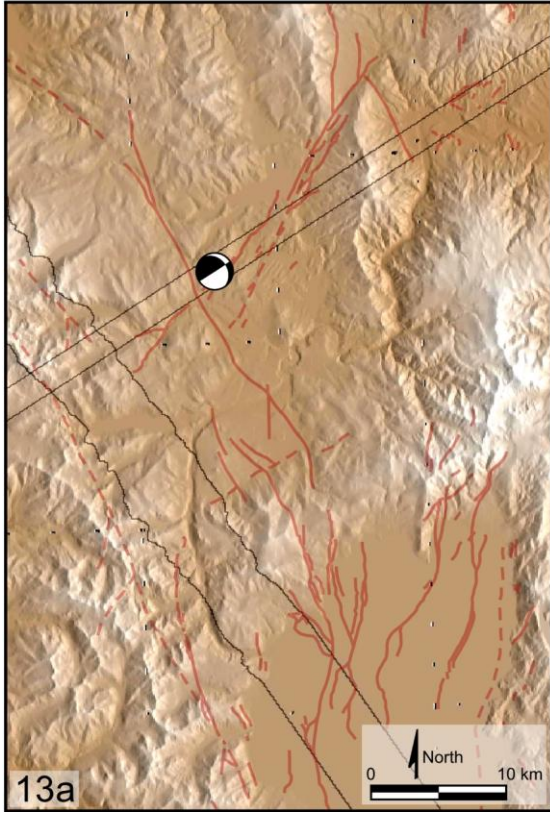


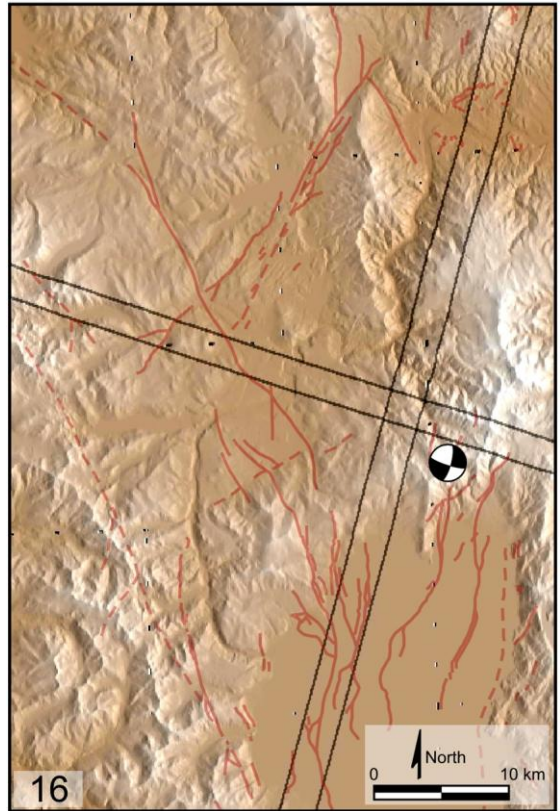
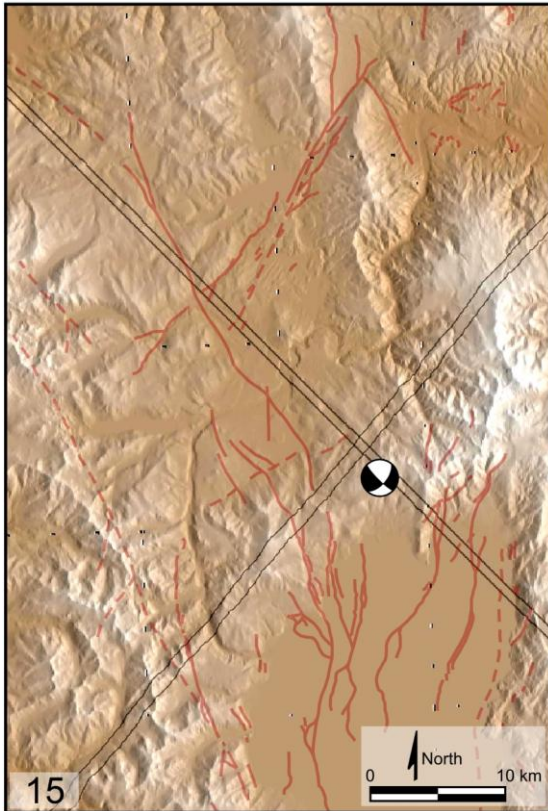
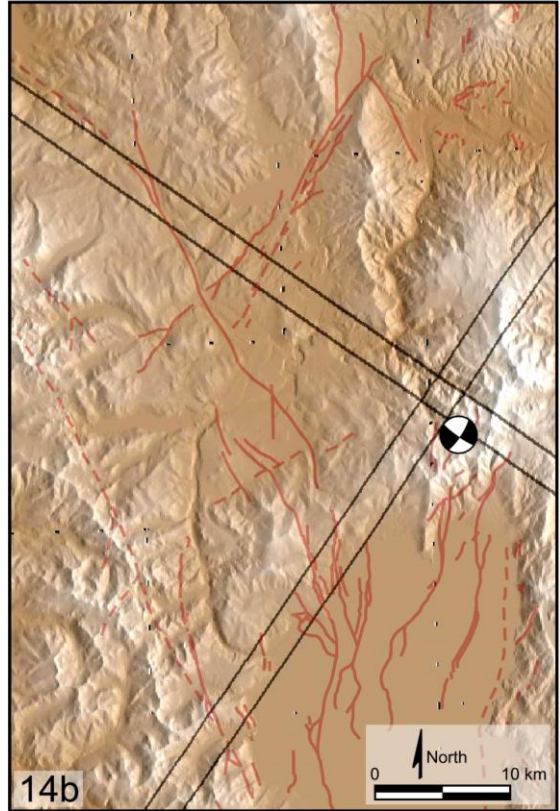
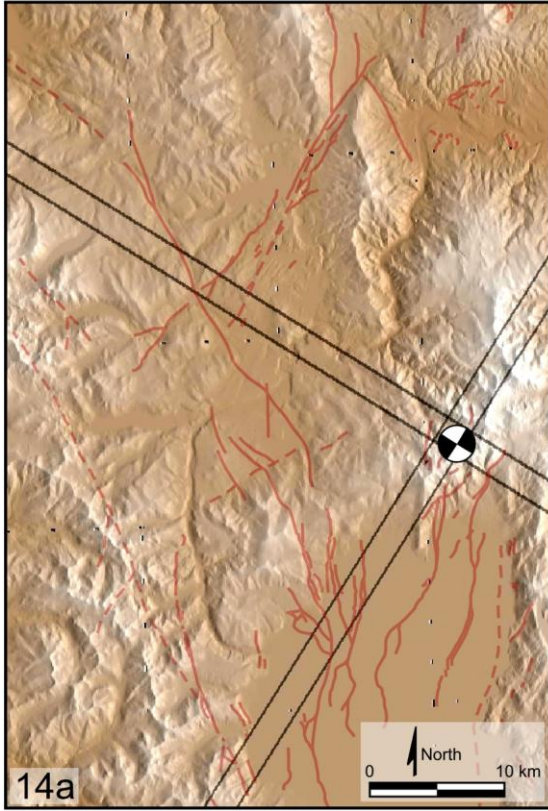


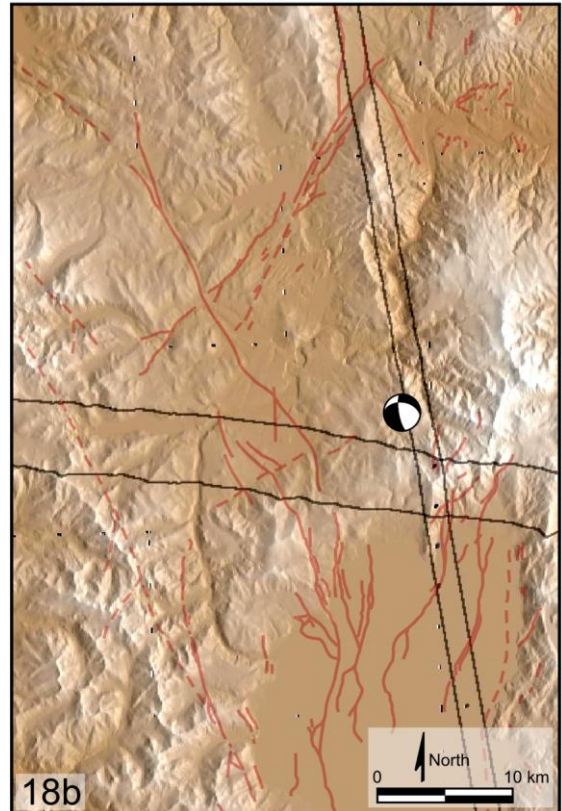
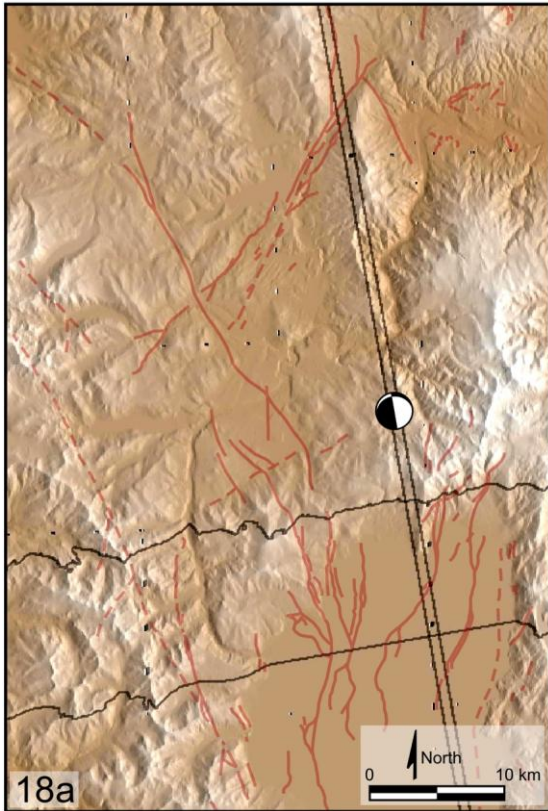
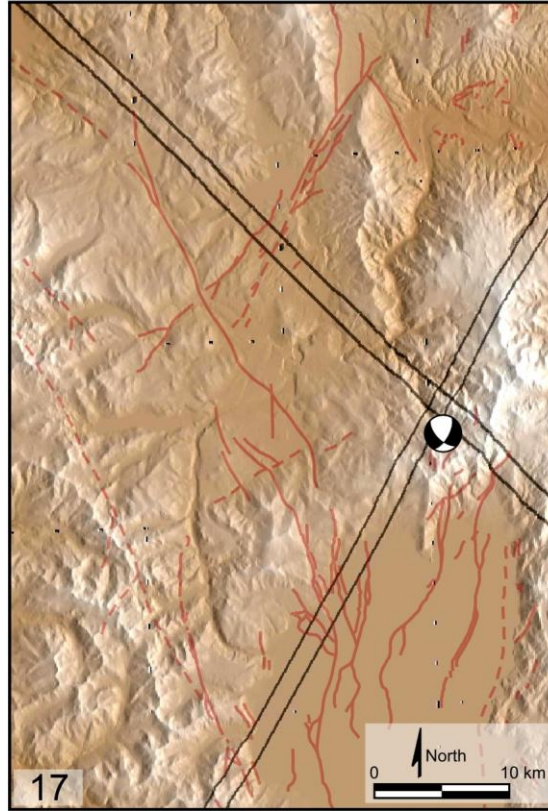


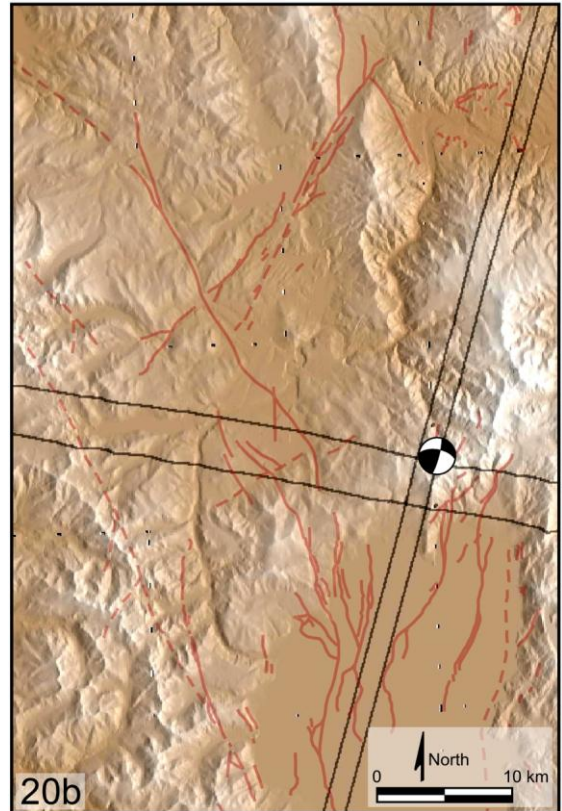
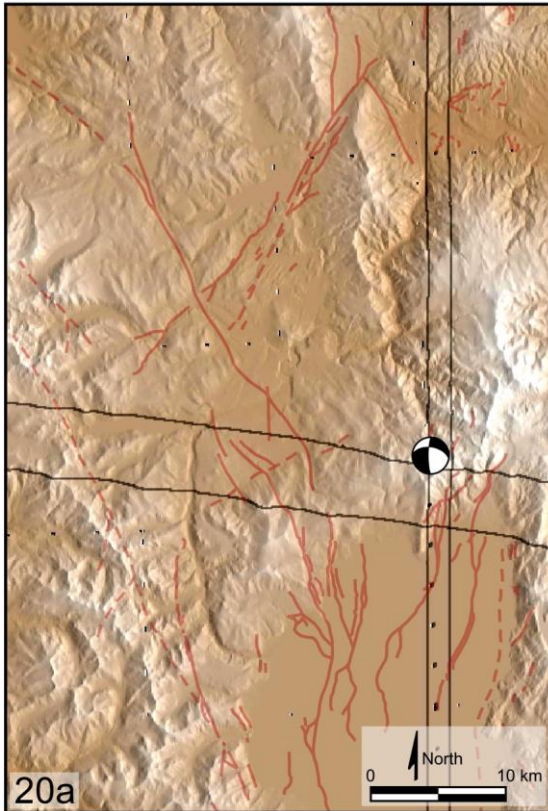
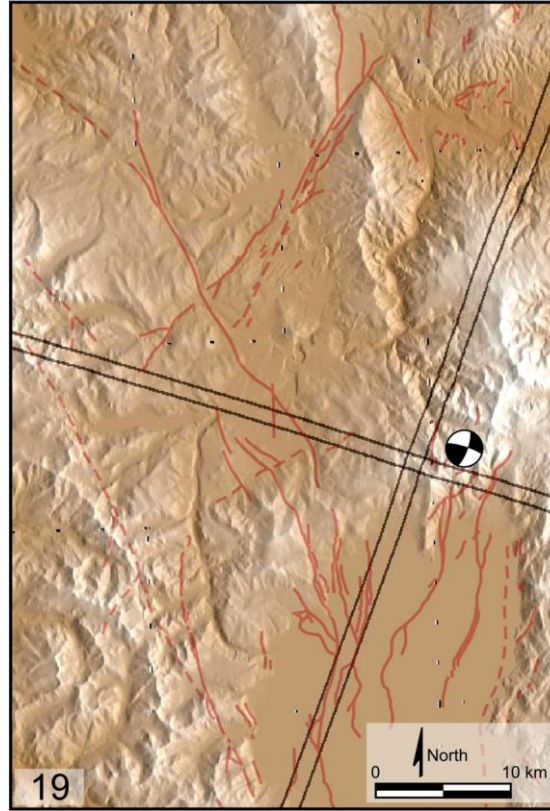


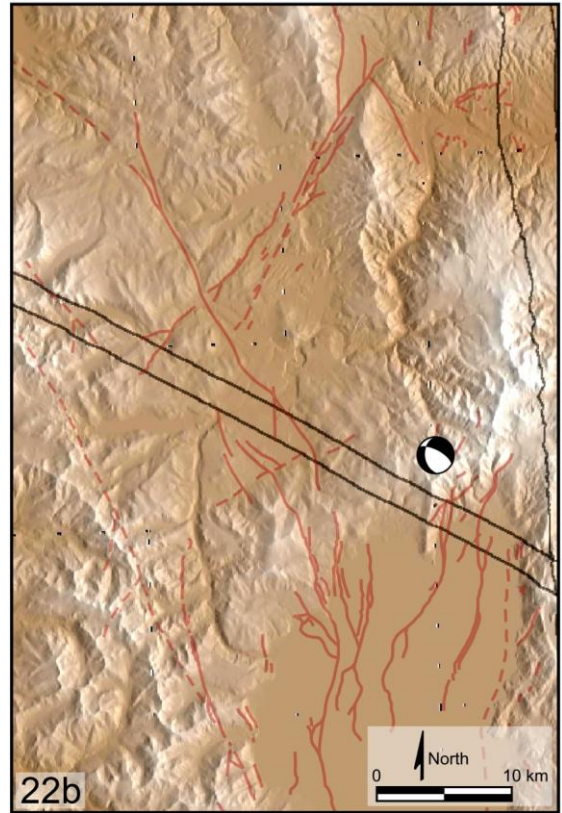
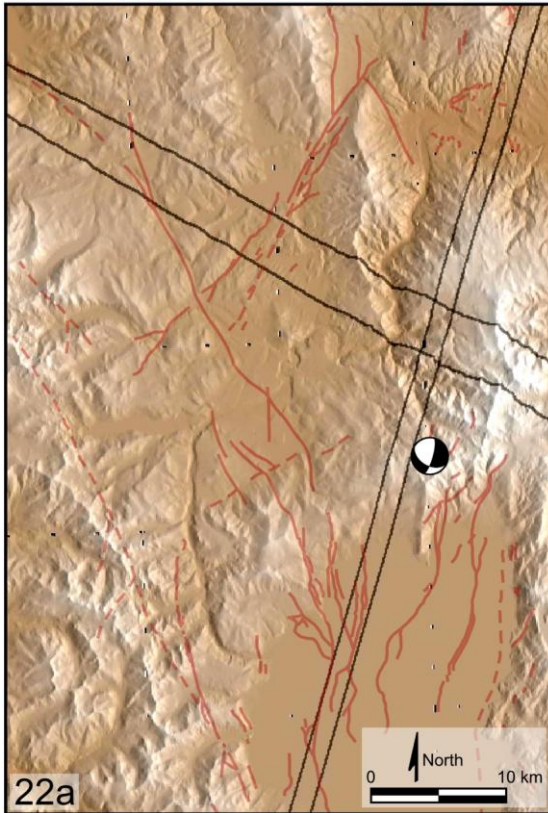
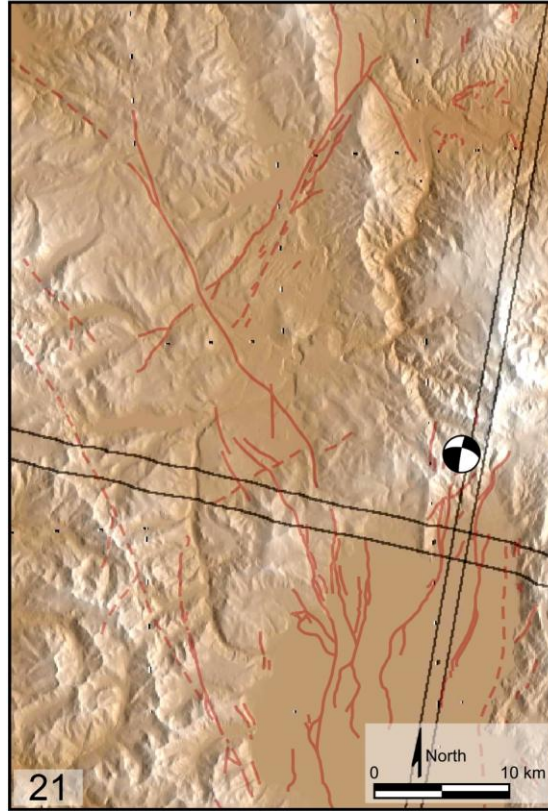


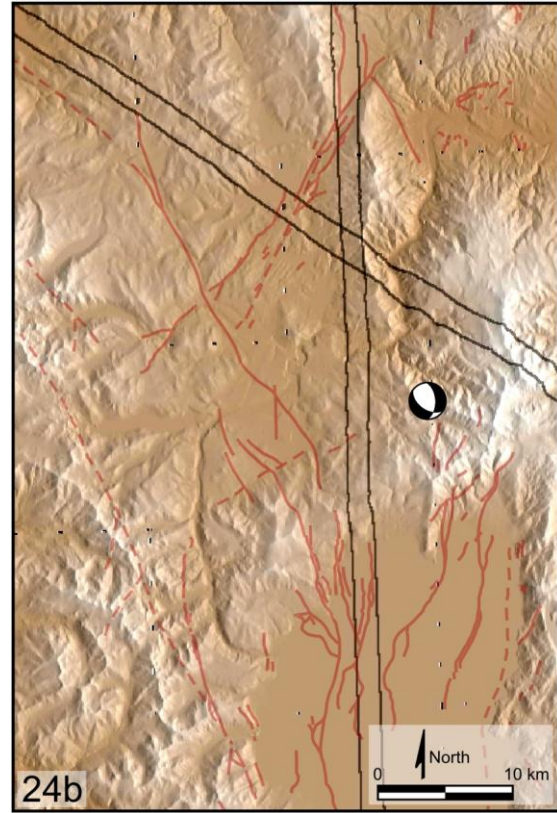
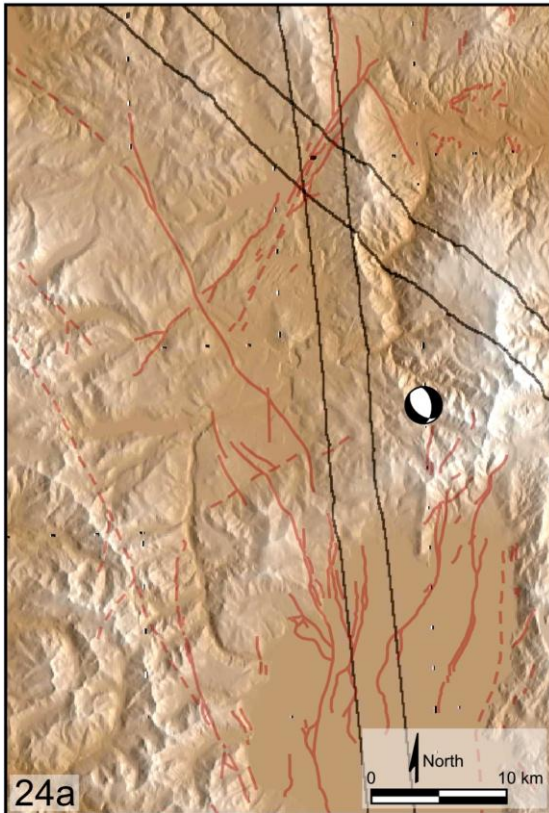
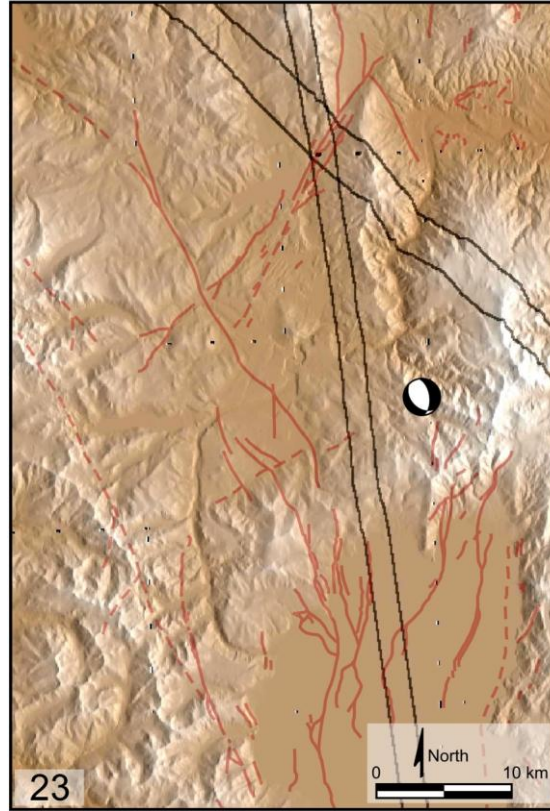


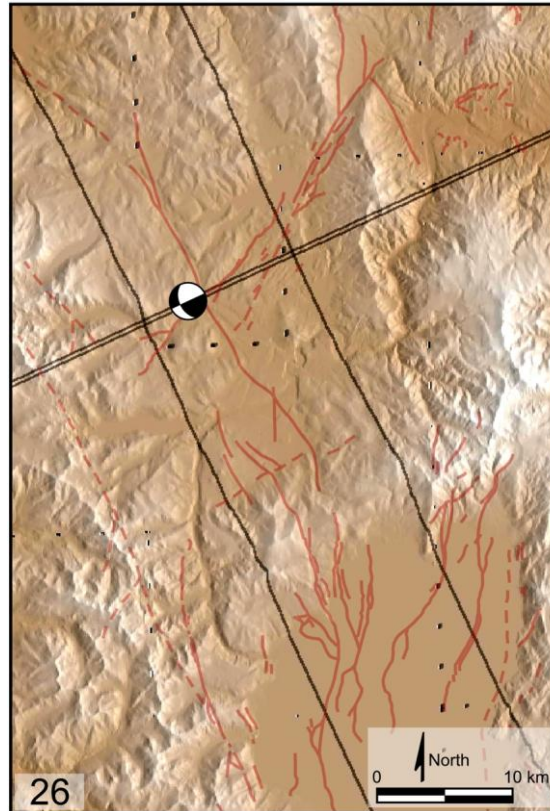
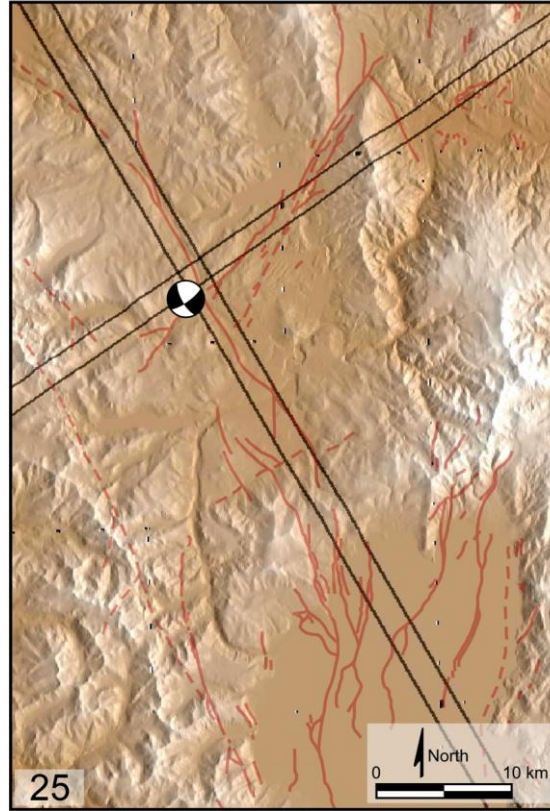


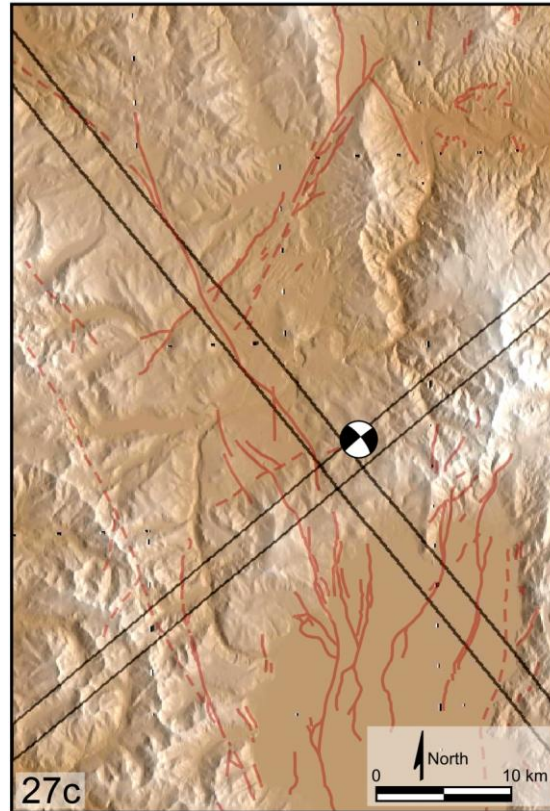
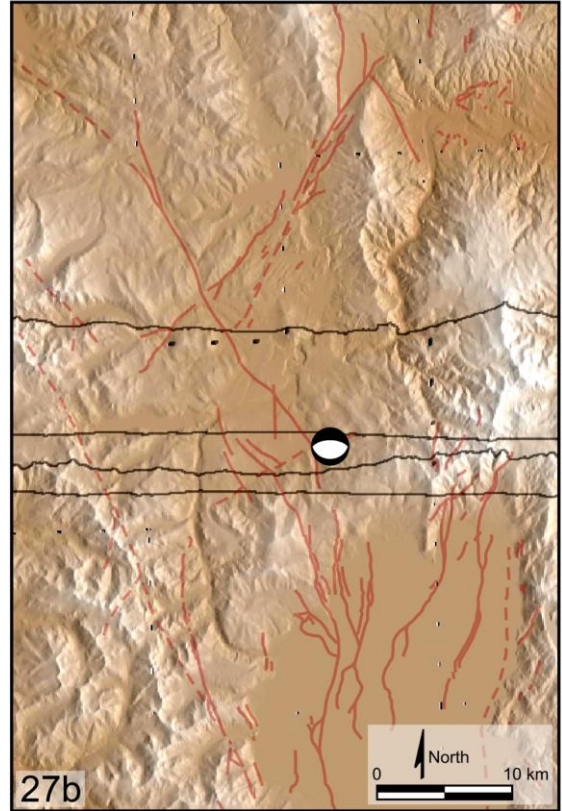
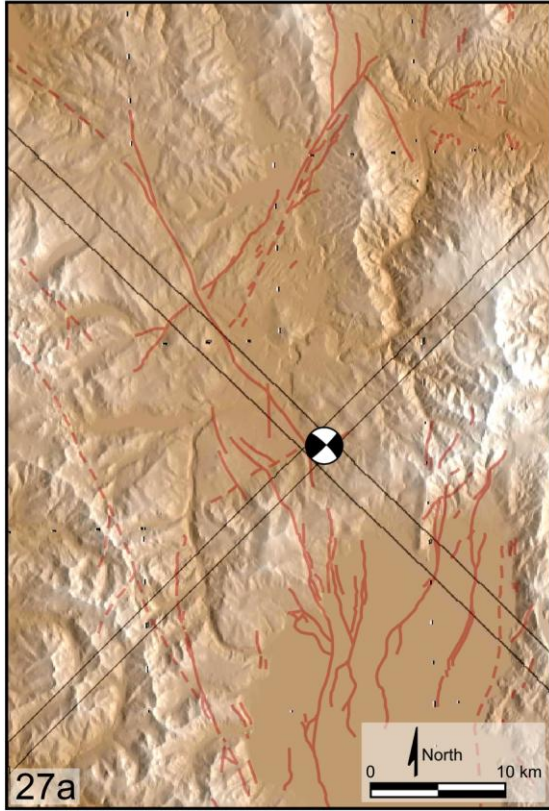


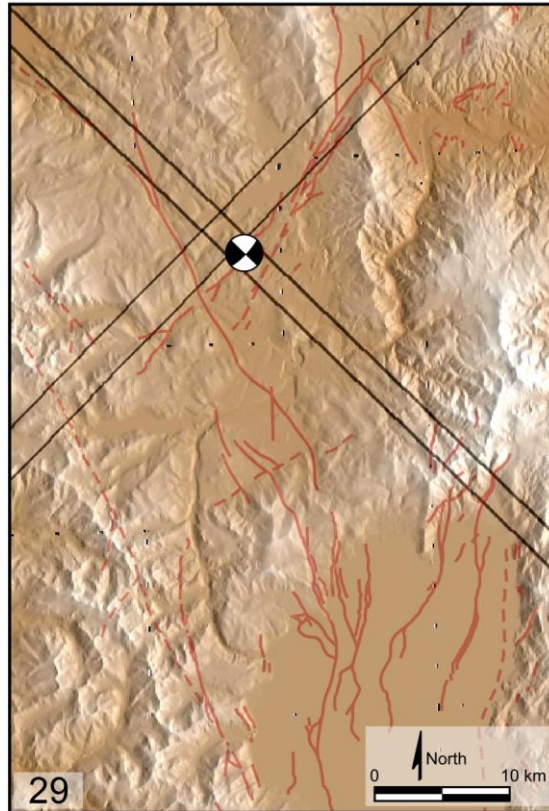
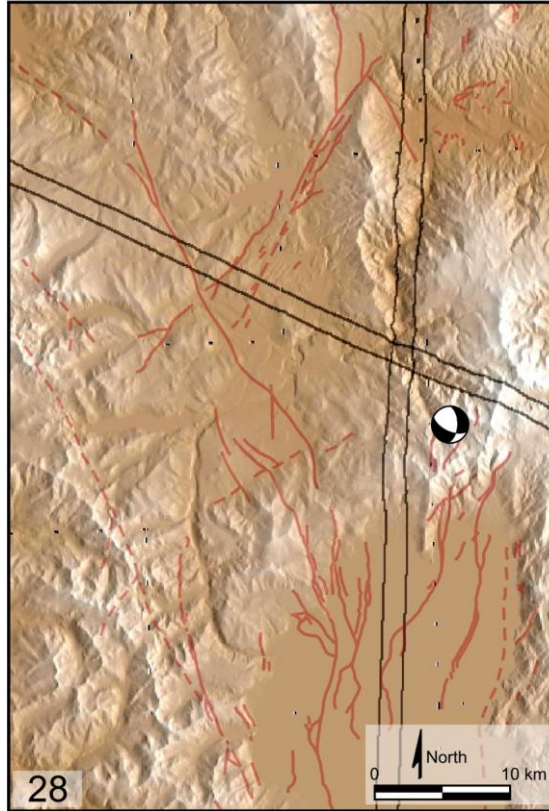












REFERENCES CITED

- Argus, D.F., and Gordon, R.G., 1991, Current Sierra Nevada-North America motion from very long baseline interferometry – Implications for the kinematics of the western United States: *Geology*, v. 19, p. 1085-1088.
- Atwater, T., 1970, Implications of plate tectonics for the Cenozoic tectonic evolution of western North America: *Geological Society of America Bulletin*, v. 81, p. 3513-3536.
- Atwater, T., and Stock, J., 1998, Pacific-North America plate tectonics of the Neogene southwestern United States – An update, *in* Ernst, W.G., and Nelson, C.A., [editors], *Integrated Earth and environmental evolution of the southwestern United States – The Clarence A. Hall, Jr., Volume*: Boulder, Colorado, Geological Society of America, p. 393-420.
- Bartow, J.A., 1979, Age control for the latest movements on the Melones fault zone in the Sierra foothills belt from K-Ar dates for late Tertiary intrusions: U.S. Geological Survey, Open File Report 79-582, p. 12.
- Bateman, P.C., and Eaton, J.P., 1967, Sierra Nevada Batholith: *Science*, v. 158, p. 1407-1417.
- Bateman, P.C., and Wahrhaftig, C., 1966, Geology of the Sierra Nevada, *in* Bailey, E.H., [editor], *Geology of Northern California*: California Division of Mines and Geology Bulletin 190, p. 107-172.
- Bayliss, B., 2007, Test of a method to recognize seismogenic faults: Waco, Texas, Baylor University Geology Department, M.S. thesis, 71 p., available online via <http://hdl.handle.net/2104/5035>.
- Bennett, R.A., Wernicke, B.P., Niemi, N.A., Friedrich, A.M., Davis, J.L., 2003, Contemporary strain rates in the northern Basin and Range province from GPS data: *Tectonics*, v. 22, no. 2.
- Birkeland, P.W., 1961, Pleistocene history of the Truckee area, north of Lake Tahoe, California: Stanford University, Ph.D. dissertation, 126 p., plate 1, scale 1:62,500.
- Birkeland, P.W., 1963, Pleistocene volcanism and deformation of the Truckee area, north of Lake Tahoe, California: *Geological Society of America Bulletin*, vol. 74, p. 1453-1474.

- Blewitt, G., Hammond, W.C., and Kreemer, C., 2009, Geodetic constraints on contemporary deformation in the northern Walker Lane – 1 Semi-permanent GPS strategy, *in* Oldow, J.S., and Cashman, P., [editors], Late Cenozoic structure and evolution of the Great Basin-Sierra Nevada transition: Geological Society of America, Special Paper 447, p. 1-15.
- Bonilla, M.G., 1982, Evaluation of potential surface faulting and other tectonic deformation: U.S. Geological Survey Open-File Report 82-732, p. 58.
- Briggs, R.W., and Wesnousky, S.G., 2004, Late Pleistocene fault slip rate, earthquake recurrence, and reactivity of slip along the Pyramid Lake fault zone, northern Walker Lane, United States: *Journal of Geophysical Research*, v. 109, B08402, doi:10.1029/2003JB002717.
- Brothers, D.S., Kent, G.M., Driscoll, N.W., Smith, S.B., Karlin, R., Dingler, J.A., Harding, A.J., Seitz, G.G., and Babcock, J.M., 2009, New constraints on deformation, slip rate, and timing of the most recent earthquake on the West Tahoe – Dollar Point Fault, Lake Tahoe Basin, California: *Bulletin of the Seismological Society of America*, v. 99, no. 2A, p. 499-519.
- Bryant, W.A., and Hart, E.W., 2007, Fault-rupture hazard zones in California: California Department of Conservation, California Geological Survey, Special Publication 42, 42 p.
- Burbank, D.W., and Anderson, R.S., 2001, *Tectonic geomorphology*: Oxford, Blackwell Science, 274 p.
- Burnett, J.L., 1982, Geologic map of Lake Tahoe: California Division of Mines and Geology, unpublished mapping, scale 1:62,500.
- Carter, B.H., 1966, Mapping and geological investigations of Prosser Creek Dam, Boca Dam, Stampede damsite, and limited regional observations after the September 12, 1966 earthquake – Washoe Project, California-Nevada: U.S. Bureau of Reclamation Memorandum, central files, Sacramento, 10 p., Map 320-208-70 (unpublished).
- Cashman, P.H., and Fontaine, S.A., 2000, Strain partitioning in the northern Walker Lane, western Nevada and northeastern California: *Tectonophysics*, v. 326, p. 111-130.
- Chester, F.M., Evans, J.P., and Biegel, R.L. 1993, Internal structure and weakening mechanisms of the San Andreas fault: *Journal Geophysical Research*, vol. 98, p. 771-786.

- Chester, F.M., Chester, J.S., Kirschner, D.L., Schulz, S.E., and Evans, J.P., 2004, Structure and large-displacement, strike-slip fault zones in the brittle continental crust, *in* Karner, G.D., Taylor, B., Driscoll, N.W., and Kohlstedt, D.L., [editors], *Rheology and deformation of the lithosphere at continental margins*: New York, Columbia University Press, p. 223-260.
- Cronin, V.S., 2004, A draft primer on focal mechanism solutions for geologists: Teaching Quantitative Skills in the Geosciences, http://serc.carleton.edu/files/NAGTWorkshops/structure04/Focal_mechanism_primer.pdf
- Cronin, V.S., 2008, Finding the mean and 95% confidence interval of a set of strike-and-dip or lineation data: *Environmental and Engineering Geoscience*, v. 14, no. 2, p. 113-119.
- Cronin, V.S., 2011a, SLAMCode.nb -- Projecting the nodal planes from a focal mechanism solution onto a digital elevation model surface: *Mathematica* notebook file available online at http://bearspace.baylor.edu/Vince_Cronin/www/MathematicaCode/SLAM_code.nb.
- Cronin, V.S., 2011b, Using earthquake focal mechanism solutions to find the surface trace of seismogenic faults: Medellin, Colombia, Sociedad Colombiana de Geologia, XIV Congreso Latinoamericano de Geologia, Memorias, p. 169; presentation text in English and images available online via http://bearspace.baylor.edu/Vince_Cronin/www/SLAM/Cronin31Aug2011.pdf.
- Cronin, V.S., 2011c, SeismoLinGeomorph.nb – Seismo-lineament geomorphology: *Mathematica* notebook file available online at http://bearspace.baylor.edu/Vince_Cronin/www/MathematicaCode/SeismoLinGeomorph.nb.
- Cronin, V.S., Lindsay, R., and Dunbar, J., 2009, Finding probable seismogenic faults using EarthScope (and other) data an the Seismo-Lineament Analysis Method [abstract]: Association of Environmental and Engineering Geologists National Meeting, South Lake Tahoe, September 2009, available via http://bearspace.baylor.edu/Vince_Cronin/www/CroninAEG09.doc
- Cronin, V.S., Millard, M.A., Seidman, L.E., and Bayliss, B.G., 2008, The Seismo-Lineament Analysis Method [SLAM] -- A reconnaissance tool to help find seismogenic faults: *Environmental and Engineering Geoscience*, v. 14, no. 3, p. 199-219.
- Cronin, V.S., Schurter, G., and Sverdrup, K.A., 1993, Preliminary Landsat lineament analysis of the northern Nanga Parbat-Haramosh Massif, northwest Himalaya: *Geological Society of London Special Publication*, No. 74, p. 193-206.

- DeMets, C., Gordon, R.G., and Argus, D.F., 2010, Geologically current plate motions: *Geophysical Journal International*, v. 181, no. 1, p. 1-80, doi:10.1111/j.1365-246X.2009.04491.x
- Dingler, J., Kent, G., Driscoll, N., Babcock, J., Harding, A., Seitz, G., Karlin, B., and Goldman, C., 2009, A high-resolution seismic CHIRP investigation of active normal faulting across Lake Tahoe Basin, California-Nevada: *Geological Society of America Bulletin*, v. 121, no. 7/8, p. 1089-1107.
- Dixon, T.H., Miller, M., Farina, F., Wang, H.Z., and Johnson, D., 2000, Present-day motion of the Sierra Nevada block and some tectonic implications for the Basin and Range province, North American Cordillera: *Tectonics*, v. 19, p. 1-24.
- Dixon, T.H., Norabuena, E., and Hotaling, L., 2003, Paleoseismology and Global Positioning System – Earthquake-cycle effects and geodetic versus geologic fault slip rates in the Eastern California Shear Zone: *Geology*, v. 31, no. 1, p. 55-58.
- Dokka, R.K., and Travis, C.J., 1990a, Role of the Eastern California shear zone in accommodating Pacific-North American plate motion: *Geophysical Research Letters*, v. 17, p. 1323-1326.
- Dokka, R.K. and C.J. Travis, 1990b, Late Cenozoic strike-slip faulting in the Mojave Desert, California: *Tectonics*, v. 9, p. 311-340.
- Dulcea, M. and Saleeby, J.B., 1998, A case for delamination of the deep batholithic crust beneath the Sierra Nevada, California: *International Geology Review*, v. 40, no. 1, p. 78-93.
- Farmer, G.L., Glazner, A.F., and Manley, C.R., 2002, Did lithospheric delamination trigger late Cenozoic potassic volcanism in the southern Sierra Nevada, California? *Geological Society of America Bulletin*, v. 114, no. 6, p. 754-768.
- Faulds, J.E., Henry, C.D., and Hinz, N.H., 2005, Kinematics of the northern Walker Lane – An incipient transform fault along the Pacific-North American plate boundary: *Geology*, v. 33, p. 505-508, doi:10.1130/G21274.1.
- Figuroa, A.M., and Knott, J.R., 2010, Tectonic geomorphology of the southern Sierra Nevada Mountains (California) – Evidence for uplift and basin formation: *Geomorphology*, v. 123, p. 34-45.
- Fisher, R.A., 1953, Dispersion on a sphere: *Proceedings Royal Society, London*, v. A217, no. 1130, p. 295-305.
- Franks, A.L., 1980, Environmental geology-land use planning, erosion and sedimentation west Martis Creek drainage basin, California: University of California, Davis, Ph.D. dissertation, 371 p., plate 1, scale 1:12,000.

- Gardner, J.V., Dartnell, P., Mayer, L.A., and Hughes-Clark, J., 1999, Bathymetry and selected perspective views of Lake Tahoe, California and Nevada: U.S. Geological Survey Water Resources Investigation Report 99-4043.
- Gardner, J.V., Mayer, L.A., and Hughes-Clark, J., 1998, Cruise report, RV Inland Surveyor cruise IS-98 – the bathymetry of Lake Tahoe, California-Nevada, August 2 through August 17, 1998, Lake Tahoe, California and Nevada: U.S. Geological Survey, Open-File Report 98-509, 28 p..
- Gardner, J.V., Mayer, L.A. and Hughes-Clarke, J.E., 2000, Morphology and processes in Lake Tahoe (California-Nevada): Geological Society of America Bulletin, v. 112, n. 5, p. 736- 746.
- Greensfelder, R., 1968, Aftershocks of the Truckee, California, earthquake of September 12, 1966: Bulletin of the Seismological Society of America, v. 58, no. 5, p. 1607-1620.
- Grose, T.L.T., 2000a, Geologic map of the Loyalton 15' quadrangle, Lassen, Plumas, and Sierra counties, California: California Division of Mines and Geology Open-File Report OFR 00-25, map scale 1:62,500.
- Grose, T.L.T., 2000b, Geologic map of the Blairsden 15' quadrangle, Plumas County, California: California Division of Mines and Geology Open-File Report OFR 00-21, map scale 1:62,500.
- Grose, T.L.T., 2000c, Geologic map of the Sierraville 15' quadrangle, Sierra and Plumas counties, California: California Division of Mines and Geology Open-File Report OFR 00-24, map scale 1:62,500.
- Hammond, W.C., and Thatcher, W., 2004, Contemporary tectonic deformation of the Basin and Range province, western United States – 10 years of observation with the Global Positioning System: Journal of Geophysical Research, v. 109, B08403, doi:10.1029/2003JB002746.
- Hammond, W.C., and Thatcher, W., 2005, Northwest Basin and Range tectonic deformation observed with the Global Positioning System, 1999-2003: Journal of Geophysical Research, v. 110, B10405, doi:10.1029/2005JB003678.
- Hammond, W.C., and Thatcher, W., 2007, Crustal deformation across the Sierra Nevada, northern Walker Lane, Basin and Range transition, western United States measured with GPS, 2000-2004: Journal of Geophysical Research, v. 112, B05411, doi:10.1029/2006JB004625.

- Hammond, W.C., Kreemer, C., and Blewitt, G., 2009, Geodetic constraints on contemporary deformation in the northern Walker Lane – 3 Central Nevada seismic belt postseismic relaxation, *in* Oldow, J.S., and Cashman, P., [editors], Late Cenozoic structure and evolution of the Great Basin-Sierra Nevada transition: Geological Society of America, Special Paper 447, p. 33-54.
- Hammond, W.C., Blewitt, G., and Kreemer, C., 2011, Block modeling of crustal deformation of the northern Walker Lane and Basin and Range from GPS velocities: *Journal of Geophysical Research*, v. 116, B04402, doi:10.1029/2010JB007817.
- Hanks, G.C., and Allen, C.R., editors, 1989, The Elmore Ranch and Superstition Hills earthquakes of 24 November 1987: Special Issue, *Bulletin of the Seismological Society of America*, v. 79, no. 2, p. 231-541.
- Harwood, D.S. and Fisher, G.R., 2002, Geologic map of part of eastern Placer County, California: U.S. Geological Survey (in preparation), scale 1:48,000.
- Hawkins, F.F., LaForge, Roland and Hansen, R.A., 1986, Seismotectonic study of the Truckee/Lake Tahoe area northeastern Sierra Nevada, California for Stampede, Prosser Creek, Boca and Lake Tahoe dams: U.S. Bureau of Reclamation Seismotectonic Report No. 85-4, 210 p., plate 1, scale 1:250,000.
- Hearn, E.H. and Humphreys, E.D., 1998, Kinematics of the southern Walker Lane belt and motion of the Sierra Nevada block, California: *Journal of Geophysical Research*, v. 103, p. 27033-27049.
- Henry, C.D., and Perkins, M.E., 2001, Sierra Nevada-Basin and Range transition near Reno, Nevada – Two-state development at 12 and 3 Ma: *Geology*, v. 29, no. 8, p. 719-722.
- Henry, T.L., and Palmer, D.F., 1974, Magnetic studies on Lake Tahoe, California-Nevada: *Geological Society of America Bulletin*, v. 85, p. 1907-1912.
- Hinz, N.H., Faulds, J.E., and Henry, C.D., 2009, Tertiary volcanic stratigraphy and paleotopography of the Diamond and Fort Sage mountains – Constraining slip along the Honey Lake fault zone in the northern Walker Lane, northeastern California and western Nevada, *in* Oldow, J.S., and Cashman, P., [editors], Late Cenozoic structure and evolution of the Great Basin—Sierra Nevada Transition: Geological Society of America, Special Paper 447, p. 101-131.
- Hudnut, K., Seeber, L., Rockwell, T., Goodmacher, J., Klinger, R., Lindvall, S., and McElwain, R., 1989, Surface ruptures on cross-faults in the 24 November 1987 superstition hills, California, earthquake sequence: *Bulletin of the Seismological Society of America*, v. 79, no. 2, p. 282-296.

- Hunter, L.E., Howle, J.F., Rose, R.S., and Bawden, G.W., 2011, LiDAR-Assisted Identification of an active fault near Truckee, California: *Bulletin of the Seismological Society of America*, v. 101, no. 3, p. 1162-1181, doi: 10.1785/0120090261.
- Hunter, L.E., Rose, R.S., Hilton, B.R., McCormick, W., and Crampton, T., 2010, Use of hi-resolution LiDAR in discovering the Polaris fault, Martis Creek dam, Truckee, California, in *Collaborative management of integrated watersheds: Proceedings, 30th Annual United States Society on Dams Conference*, Sacramento, California, p. 281-294, available online via <http://ussdams.com/proceedings/USSDproceedings2010.pdf>.
- Hunter, L.E., Rose, R.S., Howle, J.F., Brown, V.W., Powers, M.H., Hilton, B., and Hubbard, E., 2009, Geotechnical and paleoseismic investigations of the Martis Creek dam, Truckee, California: 2009 Association of Engineering Geology Field Trip Guidebook, 43 p.
- Hyne, N.J., Chelminski, P., Court, J.E., Gorsline, D.S., and Goldman, C., 1972, Quaternary history of Lake Tahoe, California-Nevada: *Geological Society of America Bulletin*, v. 83, p. 1435-1448.
- Ichinose, G.A., Anderson, J.G., Satake, Kenji, Schweickert, R.A. and Lahren, M.M., 2000, The potential hazard from tsunami and seiche waves generated by large earthquakes within Lake Tahoe, California-Nevada: *Geophysical Research Letters*, v. 27, no. 8, p. 1203- 1206.
- Ichinose, G., Anderson, J., Smith, K., dePolo, D., Anooshehpour, R., Schweickert, R., and Lahren, M., 1999, The seismotectonics of the 30 October 1998 Incline Village, Nevada earthquake and its effects: *Seismological Research Letters*, v. 70, no. 3, p. 297-305.
- Ichinose, G.A., Anderson, J.G., Smith, K.D., and Zeng, Y., 2003, Source parameters of eastern California and western Nevada earthquakes from regional moment tensor inversion: *Bulletin of the Seismological Society of America*, v. 93, no. 1, p. 61-84.
- Jennings, C.W., and Bryant, W.A., 2010, An explanatory text to accompany the fault activity map of California, scale 1:750,000: California Geological Survey, 94 p., accessible online via [http:// www.consrv.ca.gov/cgs/cgs_history/Documents/FAM_phamplet.pdf](http://www.consrv.ca.gov/cgs/cgs_history/Documents/FAM_phamplet.pdf)
- Kachadoorian, R., Yerkes, R.F., and Waananen, A.O., 1967, Effects of the Truckee, California, earthquake of September 12, 1966: U.S., Geological Survey, Circular 573, p. 14.

- Kent, G.M., Babcock, J.M., Driscoll, N.W., Harding, A.J., Dingler, J.A., Seitz, G.G., Gardner, J.V., Mayer, L.A., Goldman, C.R., Heyvaert, A.C., Richards, R.C., Karlin, R., Morgan, C.W., Gayes, P.T., and Owen, L.A., 2005, 60 k.y. record of extension across the western boundary of the Basin and Range Province – Estimate of slip rates from offset shoreline terraces and a catastrophic slide beneath Lake Tahoe: *Geology*, v. 33, no. 5, p. 365-368.
- Kleinfelder-Geomatrix, 2009, Martis Creek DSAP Fault Trenching Interim Report, Nevada County, California. Sacramento, California: Kleinfelder-Geomatrix Joint-Venture, Report Prepared for Sacramento District, U.S. Army Corps of Engineers under Contract No. W91238-08-D-0015, Task Order 0009. July 2009.
- Kreemer, C., and Hammond, W.C., 2007, Geodetic constraints on areal changes in the Pacific-North America plate boundary zone – What controls Basin and Range extension? *Geology*, v. 35, no. 10, p. 943-947.
- Kreemer, C., Blewitt, G., and Hammond, W.C., 2009, Geodetic constraints on contemporary deformation in the northern Walker Lane -- 2 Velocity and strain rate tensor analysis, *in* Oldow, J.S., and P.H. Cashman, [editors], *Late Cenozoic Structure and Evolution of the Great Basin – Sierra Nevada Transition: Geological Society of America, Special Paper 447*, p. 17-31.
- Kreemer, C., Holt, W.E., and Haines, A.J., 2003, An integrated global model of present-day plate motions and plate boundary deformation: *Geophysical Journal International*, v. 154, p. 8-34.
- Kumamoto, T., Wesnousky, S.G., Okamura, M., Tsutsumi, H., Chida, N., Shimazaki, K., Nakata, T., and Rose, M.R., 1995, Active faults in Lake Tahoe, western part of the United States: *Active Fault Research*, v. 13, p. 47-53.
- Lancaster, D., 2011, Correlation of earthquakes with seismogenic faults along the Northern Arizona Seismic Belt, southwestern margin of the Colorado Plateau: Waco, Texas, Baylor University Geology Department, M.S. thesis, 98 p., available online via <http://hdl.handle.net/2104/8228>.
- Le, K., Lee, J., Owen, L.A., and Finkel, R., 2007, Late Quaternary slip rates along the Sierra Nevada frontal fault zone, California – Slip partitioning across the western margin of the Eastern California Shear Zone-Basin and Range Province: *Geological Society of America Bulletin*, v. 119, no. 1/2, p. 240-256.
- Locke, A., Billingsley, P., and Mayo, E.B., 1940, Sierra Nevada tectonic patterns: *Geological Society of America Bulletin*, v. 51, p. 513-540.
- Louie, J.N., Thelen, W., Smith, S.B., Scott, J.B., Clark, M., and Pullammanappallil, S., 2004, The northern Walker Lane refraction experiment – Pn arrivals and the northern Sierra Nevada root: *Tectonophysics*, v. 388, p. 253-269.

- Manley, C.R., Glazner, A.F., and Farmer, G.L., 2000, Timing of volcanism in the Sierra Nevada of California – Evidence for Pliocene delamination of the batholithic root? *Geology*, v. 28, no. 9, p. 811-814.
- Maune, D.F., [editor], 2001, Digital elevation model technologies and applications – the DEM user’s manual: Bethesda, Maryland, The American Society for Photogrammetry and Remote Sensing, 539 p.
- McCaffrey, R., 2005, Block kinematics of the Pacific-North America plate boundary in the southwestern United States from inversion of GPS, seismological, and geologic data: *Journal of Geophysical Research*, v. 110, B07401, doi:10.1029/2004JB003307.
- McCaplin, J., ed., 2009, Paleoseismology [2nd edition]: Amsterdam, Academic Press, 613 p.
- McCaughey, J.W., 2003, Pleistocene glaciation of the southwest Tahoe Basin, Sierra Nevada, California: University of Nevada, Reno, M.S. thesis, 179 p., plate 1, scale 1:15,400.
- Melody, A.D., 2009, Active faulting and Quaternary paleohydrology of the Truckee fault zone north of Truckee, California: unpublished M.S. thesis, Humboldt State University, 71 p.; available online via <http://humboldt-dspace.calstate.edu/xmlui/handle/2148/520>.
- Millard, M., 2007, Linking onshore and offshore data to find seismogenic faults along the eastern Malibu coastline: Waco, Texas, Baylor University Geology Department, M.S. thesis, 136 p., available online via <http://hdl.handle.net/2104/5109>.
- Miller, V.C., 1961, *Photogeology*: McGraw-Hill, New York, p. 248.
- Moore, J.G., Schweikert, R.A., Robinson, J.E., Lahren, M.M., and Kitts, C.A., 2006, Tsunami generated boulder ridges in Lake Tahoe, California-Nevada: *Geology*, vol. 34, no. 11, p. 965-968.
- Northern California Earthquake Data Center, accessed 2008-2011, available online via <http://www.ncedc.org>.
- Oldow, J.S., 2003, Active transtensional boundary zone between the western Great Basin and Sierra Nevada block, western U.S. Cordillera: *Geology*, v. 31, no. 12, p. 1033-1036.
- Oldow, J.S., and Cashman, P.H., 2009, Introduction, *in* Oldow, J.S., and Cashman, P.H., [editors], Late Cenozoic structure and evolution of the Great Basin-Sierra Nevada transition: Geological Society of America, Special Paper 447, p. v-viii.

- Oldow, J.S., Aiken, C.L.V., Hare, J.L., Ferguson, J.F., and Hardyman, R.F., 2001, Active displacement transfer and differential block motion within the central Walker Lane, western Great Basin: *Geology*, v. 29, no. 1, p. 19-22.
- Olig, S., Sawyer, T., Wright, D., Terra, F., and Anderson, L., 2005a, Preliminary seismic source characterization of faults near Stampede and Prose Creek dams - Washoe project and Boca Dam - Truckee storage project, U.S. Department of the Interior, Bureau of Reclamation, Denver, 65 p.
- Olig, S., Sawyer, T., Anderson, L., Wright, D., Wong, I., and Terra, F., 2005b, Insights into Quaternary strain patterns in the northern Walker Lane from mapping and source characterization of faults near Truckee, California [abstract]: *Seismological Research Letters*, v. 76, no. 2, p. 251.
- Pacha, A., Anderson, J.G., and Kreemer, C., 2006, Comparison of seismic and geodetic scalar moment rates across the Basin and Range Province: *Bulletin of the Seismological Society of America*, v. 96, no. 1, p. 11-32.
- Page, W.D., and Sawyer, T.L., 1992, Tectonic deformation of the Lovejoy Basalt, a late Cenozoic strain gage across the northern Sierra Nevada, California: *Eos, Transactions of the American Geophysical Union*, v. 73, no. 43, p. 590.
- Quaternary Fault and Fold Database of the United States, accessed 2008-2011, available online via <http://earthquake.usgs.gov/hazards/qfaults/>.
- Ray, R.G., 1960, Aerial photographs in geologic interpretation and mapping: U.S. Geological Survey Professional Paper 373, p. 230.
- Reasenberg, P.A., and Oppenheimer, D., 1985, FPFIT, FPLOT, and FPPAGE -- Fortran computer programs for calculating and displaying earthquake fault-plane solutions: U.S. Geological Survey, Open-File Report, no. 85-739.
- Rogers, A.M., Harmsen, S.C., Corbett, E.J., Priestley, K., and dePolo, D., 1991, The seismicity of Nevada and some adjacent parts of the Great Basin, *in* Slemmons, D.B., Engdahl, E.R., Zoback, M.D., and Blackwell, D.D., [editors], *Neotectonics of North America*: Boulder, Colorado, Geological Society of America, Decade Map Volume 1, p. 153-184
- Ryall, A.S., and VanWormer, J.D., 1980, Estimation of maximum magnitude and recommended seismic zone changes in the western Great Basin: *Seismological Society of America Bulletin*, v. 70, p. 1573-1581.
- Ryall, A., Van Wormer, J.D., and Jones, A.J., 1968, Triggering of micro-earthquakes by earth tides, and other features of the Truckee, California, earthquake sequence of September, 1966: *Bulletin of the Seismological Society of America*, v. 58, no. 1, p. 215-248.

- Saleeby, J., and Foster, Z., 2004, Topographic response to mantle lithosphere removal in the southern Sierra Nevada region, California: *Geology*, v. 32, no. 3, p. 245-248.
- Sauber, J., Thatcher, W., Solomon, S., and Lisowski, M., 1994, Geodetic slip rate for the eastern California shear zone and the recurrence time of Mojave Desert earthquakes: *Nature*, v. 367, p. 264-266.
- Saucedo, G.J., 1992, Map showing recency of faulting, Chico quadrangle, California: California Division of Mines and Geology, Regional Geologic Map Series, Map 7A, Sheet 5, scale 1:250,000.
- Saucedo, G.J., compiler, 2005, Geologic map of the Lake Tahoe Basin, California and Nevada, scale 1:100,000: California Geological Survey, Regional Geological Map Series, Map No. 4, accessible online via <http://www.quake.ca.gov/gmaps/RGM/tahoe/tahoe.html>
- Saucedo, G.J., and Wagner, D.L., 1992, Geologic map of the Chico quadrangle: California Division of Mines and Geology, Map 7A, accessible online via <http://www.quake.ca.gov/gmaps/RGM/chico/chico.html>
- Savage, J.C., Gan, W., and Svarc, J.L., 2001, Strain accumulation and rotation in the Eastern California Shear Zone: *Journal of Geophysical Research*, v. 106, no. B10, p. 21,995-22,007.
- Savage, J.C., Lisowski, M., and Prescott, W.H., 1990, An apparent shear zone trending north-northwest across the Mojave Desert into Owens Valley: *Geophysical Research Letters*, v. 17, p. 2113-2116.
- Sawyer, T.L., compiler, 1995a, Fault number 25a, Mohawk Valley fault zone, Mohawk Valley section, *in* Quaternary fault and fold database of the United States: U.S. Geological Survey website, <http://earthquakes.usgs.gov/regional/qfaults>.
- Sawyer, T.L., compiler, 1995b, Fault number 25b, Mohawk Valley fault zone, Sierra Valley section, *in* Quaternary fault and fold database of the United States: U.S. Geological Survey website, <http://earthquakes.usgs.gov/regional/qfaults>.
- Sawyer, T.L., compiler, 1999a, Fault number 1650, Incline Village fault, *in* Quaternary fault and fold database of the United States: U.S. Geological Survey website, <http://earthquakes.usgs.gov/regional/qfaults>.
- Sawyer, T.L., compiler, 1999b, Fault number 1651, East Tahoe fault, *in* Quaternary fault and fold database of the United States: U.S. Geological Survey website, <http://earthquakes.usgs.gov/regional/qfaults>.

- Sawyer, T.L., and Haller, K.M., compilers, 2000, Fault number 1649, North Tahoe fault, *in* Quaternary fault and fold database of the United States: U.S. Geological Survey website, <http://earthquakes.usgs.gov/regional/qfaults>.
- Sawyer, T.L., and Page, W.D., 1993, Recurrent late Quaternary surface faulting along the Mohawk Valley fault zone, NE California: Geological Society of America, Abstracts with Programs, v. 25, no. 5, p. 142.
- Sawyer, T.L., Briggs, R.W., and Ramelli, A.R., 2005, Late Quaternary activity of the southern Mohawk Valley fault zone, northeastern California: Seismological Research Letters, v. 76, p. 248.
- Sawyer, T.L., Page, W.D., and Hemphill-Haley, M.A., 1993, Recurrent late Quaternary surface faulting along the southern Mohawk Valley fault zone, NE California: Geological Society of America, Abstracts with Programs, v. 25, no. 5, p. 142.
- Scherbaum, F., Kuehn, N., and Zimmermann, B., accessed 2011, Earthquake focal mechanism: Computable Demonstration File, Wolfram Demonstrations Project, accessible online via <http://demonstrations.wolfram.com/EarthquakeFocalMechanism/>.
- Scholz, C.H., 2002, The mechanics of earthquakes and faulting, 2nd ed.: Cambridge, U.K., Cambridge University Press, 471 p.
- Schweickert, R.A., Lahren, M.M., Smith, K., and Karlin, R., 1999, Preliminary fault map of the Lake Tahoe Basin, California and Nevada: Seismological Research Letters, v. 70, no. 3, p. 306-312.
- Schweickert, R.A., Lahren, M.M., Karlin, R., Howle, J. and Smith, K., 2000a, Lake Tahoe active faults, landslides, and tsunamis, in Lageson, D.R., Peters, S.G. and Lahren, M.M., editors, Great Basin and Sierra Nevada: Geological Society of America Field Guide 2, p. 1-22.
- Schweickert, R.A., Lahren, M.M., Karlin, R.E., Smith, K.D. and Howle, J.F., 2000b, Preliminary map of Pleistocene to Holocene faults in the Lake Tahoe Basin, California and Nevada: Nevada Bureau of Mines and Geology Open-File Report 2000-4, scale 1:100,000.
- Schweickert, R.A., Lahren, M.M., Smith, K.D., Howle, J.F., and Ichinose, G., 2004, Transtensional deformation in the Lake Tahoe region, California and Nevada, USA: Tectonophysics, vol. 392, p. 303-323.
- Schweickert, R.A., Lahren, M.M., Smith, K.D., and Karlin, R., 1999, Preliminary fault map of the Lake Tahoe basin, California and Nevada: Seismological Research Letters, v. 70, no. 3, p. 306-313.

- Seidman, L., 2007, Seismo-lineament analysis of the Malibu Beach quadrangle, southern California: Waco, Texas, Baylor University Geology Department, M.S. thesis, 95 p., available online via <http://hdl.handle.net/2104/5108>
- Seitz, G., 2009, Large magnitude Holocene earthquakes recorded on the Incline Village fault, Lake Tahoe, California-Nevada, in Bell, J.W., and Ramelli, A.R., Geohazards of the Lake Tahoe basin and the eastern front of the Sierra Nevada: Association of Engineering Geologists, Field Trip Guidebook, p. 29-35.
- Sharp, R.V., Budding, K.E., Boatwright, J. Ader, M.J., Bonilla, M.G., Clark, M.M., Fumal, T.E., Harms, K.K., Lienkaemper, J.J., Morton, D.M., O'Neill, B.J., Ostergren, C.L., Ponti D.J., Rymer, M.J., Saxton, J.L., and Sims, J.D., 1989, Surface faulting along the Superstition Hills fault zone and nearby faults associated with the earthquakes of 24 November 1987: Bulletin of the Seismological Society of American, v. 79, no. 2, p. 254-281.
- Sibson, R.H., 2003, Thickness of the seismic slip zone: Bulletin of the Seismological Society America, v. 93, p. 1169-1178.
- Slemmons, D.B., and dePolo, C.M., 1986, Evaluation of active faulting and associated hazards, *in* Studies in Geophysics – Active Tectonics: Washington, D.C., National Research Council, National Academy Press, p. 45-62.
- Smith, K.D., von Seggern, D., Blewitt, G., Preston, L., Anderson, J.G., Wernicke, B.P., and Davis, J.L., 2004, Evidence for deep magma injection beneath Lake Tahoe, Nevada-California: Science, v. 305, p. 1277-1280.
- Snoke, A.W., Tullis, J., and Todd, V.R., [editors], 1998, Fault-related rocks – a photographic atlas: Princeton, New Jersey, Princeton University Press, 617 p.
- Stewart, J.H., 1988, Tectonics of the Walker Lane belt western Great Basin – Mesozoic and Cenozoic deformation in a shear zone. In: Ernst, W.G. (Ed.), Metamorphism and Crustal Evolution of the Western United States. Englewood Cliffs, Prentice Hall, New Jersey, pp. 683-713.
- Surpless, B.E., Stockli, D.F., Dumitru, T.A., and Miller, E.L., 2002, Two-phase westward encroachment of Basin and Range extension into the northern Sierra Nevada: Tectonics, vol. 21, no. 1, p. 1-13.
- Svarc, J.L., Savage, J.C., Prescott, W.H., and Ramelli, A.R., 2002, Strain accumulation and rotation in western Nevada, 1993-2000, Journal of Geophysical Research, v. 107, no. B5.

- Sylvester, A.G., Wise, W.S., Hastings, J.T., and Moyer, L.A., 2007, Digital geologic map of the Tahoe – Donner Pass region, northern Sierra Nevada, California: University of California, Santa Barbara, Department of Earth Science, scale 1:40,000, accessible online via <http://www.geol.ucsb.edu/projects/tahoe/FinalTahoeMap2.jpg>
- Thompson, G.A. and Parsons, T., 2009, Can footwall unloading explain late Cenozoic uplift of the Sierra Nevada crest?: *International Geology Review*, v. 51, nos. 9-11, p. 986-993.
- Tsai, Y-B., and Aki, K., 1970, Source mechanism of the Truckee, California, Earthquake of September 12, 1966: *Bulletin of the Seismological Society of America*, v. 60, no. 4, p. 1199-1208.
- Turner, H.W., 1897, Downieville folio, California: U.S. Geological Survey, Folio 37, scale 1:125,000.
- Turner, R., Koehler, R., Briggs, R.W., and Wesnousky, S.G., 2008, Reevaluation of the fault slip rate and paleoseismic history of the Henry Lake fault zone, northeastern California: *Bulletin of the Seismological Society of America*, v. 98, p. 1730-1736, doi:10.1785/0120070090.
- Uhrh, J., Humphrey, J., and Barton, A., 2003, Transtensional model for the Sierra Nevada frontal fault system, eastern California: *Geology*, v. 31, no. 4, p. 327-330.
- VanWormer, J.D., and Priestly, K.F., 1978, Earthquake activity in the Reno-Truckee area, north-central Sierra Nevada mountains [abstract]: *Earthquake Notes*, Seismological Society of America, v. 49, p. 28.
- VanWormer, J.D., and Ryall, A.S., 1980, Sierra Nevada-Great Basin boundary zone – earthquake hazard related to structure, active tectonic processes, and anomalous patterns of earthquake occurrence: *Bulletin of the Seismological Society of America*, v. 70, no. 5, p. 1557-1572.
- Wagner, D.L., Jennings, C.W., Bedrossian, T.L., and Bortugno, E.J., 1981, Geologic map of the Sacramento Quadrangle: California Division of Mines and Geology, Map 1A, scale 1:250,000, accessible online via <http://www.quake.ca.gov/gmaps/RGM/sacramento/sacramento.html>
- Wakabayashi, J., and Sawyer, T.L., 2001, Stream incision, tectonics, uplift, and evolution of topography of the Sierra Nevada, California: *Journal of Geology*, v. 109, p. 539-562.
- Wdowinski, S., and Eriksson, S., 2009, Geodesy in the 21st century: *Eos, Transactions, American Geophysical Union*, v. 90, no. 18, p. 153-155.

- Wernicke, B., and Snow, J.K., 1998, Cenozoic extension in the central Basin and Range – Motion of the Sierran-Great Valley block: *International Geological Review*, v. 40, p. 403-410.
- Wernicke, B.P., Clayton, R., Ducea, M., Jones, C.H., Park, S., Rupper, S., Saleeby, J., Snow, J.K., Squires, L., Fliedner, M, Jiracek, G., Keller, R., Klemperer, S., Luetgert, J., Malin, P., Miller, K., Mooney, W., Oliver, H., Phinney, R. 1996, Origin of high mountains in the continents – the southern Sierra Nevada: *Science*, v. 271, p. 190-193.
- Wesnousky, S.G., 2005a, Active faulting in the Walker Lane: *Tectonics*, v. 24, p. TC3009, doi:10.1029/2004TC001645.
- Wesnousky, S.G., 2005b, The San Andreas and Walker Lane fault systems, western North America – transpression, transtension, cumulative slip and the structural evolution of a major transform plate boundary: *Journal of Structural Geology*, v. 27, p. 1505-1512.
- Wesson, R.L., Helley, E.J., Lajoie, K.R. and Wentworth, C.M., 1975, Faults and future earthquakes, *in* Borchardt, R.D., [editor], *Studies for seismic zonation of the San Francisco Bay region*: U.S. Geological Survey Professional Paper 941-A, p. 5-30.
- Wills, C.J., and Borchardt, G., 1993, Holocene slip rate and earthquake recurrence on the Honey Lake fault zone, northeastern California: *Geology*, v. 21, p. 853-856.
- Yeats, R.S., Sieh, K., and Allen, C.R., 1997, *The geology of earthquakes*: New York, Oxford University Press, 568 p.
- Zoback, M.L., and Zoback, M.D., 1980, Faulting patterns in north-central Nevada and strength of the crust: *Journal of Geophysical Research*, v. 85, no. B1, p. 275-284.